Design and characterisation of high-power superluminescent diodes

Burrow, Liam

Award date:
2005

Awarding institution:
University of Bath

Design and Characterisation of High-Power Superluminescent Diodes

Submitted by

Liam Burrow

For the degree of Doctor of Philosophy

University of Bath

Department of Electronic and Electrical Engineering

June 2005

Liam Burrow

ProQuest LLC
789 East Eisenhower Parkway
P.O. Box 1346
Ann Arbor, MI 48106-1346

Summary

This PhD thesis presents the design and characterisation of high-power superluminescent diodes (SLDs) designed with the aim of improving device efficiency. SLD-to-fibre coupling are also discussed in detail. In addition, two new SLD designs are introduced and the experimental characterisation of in-house fabricated prototypes is discussed in the context of the theoretical results obtained from models developed in-house.

Two models based on the ray analysis have been developed especially to interpret the experimental characterisation of SLDs with unconventional geometry. The models can be used to compute the operational characteristics of SLDs with various geometries, including tapered geometries. Whenever possible theoretical results are used to validate representative experimental results obtained from over two hundred SLDs fabricated in-house from high-power, triple quantum well InGaAs/GaAs/AlGaAs material. Superluminescent operation is achieved by etching a v-groove deflector at the rear of the device to effectively suppress lasing. Record-breaking output powers in excess of 1.3W have been achieved under pulsed operation with AR coated tapered SLDs, with 16% peak wall-plug efficiency and low spectral modulation (< 0.1dB).

The effect of optical gain saturation on the operating characteristics of stripe and tapered geometry SLDs is investigated. Efforts to improve device efficiency by reducing optical saturation and introducing (effective) index-guiding regions along the length of the device are discussed and substantiated with several experimental results.

Two methods of coupling SLDs to multi-mode and single-mode fibres are presented. Butt-coupling efficiencies of 84% into multi-mode fibre and 5.3% into single-mode fibres have been achieved, corresponding to 750mW and 7.5mW optical power in the fibre, respectively. A three-lens system was then used to correct the inherent astigmatism of the SLD output beam, increasing the coupling efficiency into single-mode fibres to 23%, corresponding to 45mW into the fibre.

Tapered geometry SLD arrays to further increase the output power, and segmented-contacts SLDs, referred to as a *'Hammer-Head'* SLD, to achieve linear power-current characteristics are presented for the first time in this thesis. The extensive theoretical and experimental characterisation of such devices is presented in detail. Output powers in excess of 2.7W have been achieved with (non-AR coated) SLDs array prototypes fabricated in-house maintaining the same output beam characteristics achieved with individual SLDs. A linear power-current characteristic up to 4A driving current has been achieved by adjusting the relative currents in the hammer-head SLD, achieving $0.04WA^{-1}$ slope efficiency.

Contents

List of Figures

List of Tables

List of Abbreviations and Acronyms

AR	Anti-Reflection
ASE	Amplified Spontaneous Emission
B-C	Butt-Coupling
BER	Bit Error Rate
CCD	Charge-Coupled Device
COD	Catastrophic Optical Damage
CW	Constant Wave
DH	Double-Heterostructure
DOP	Degree of Polarisation
ED	Etch Depth
EDC	Effective Dielectric Constant
EDFA	Erbium Doped Fibre Amplifier
ERI	Effective Refractive Index
FCA	Free-Carrier Absorption
FF	Far Field
FOG	Fibre Optic Gyroscope
FP	Fabry-Perot
FWHM	Full Width at Half Maximum
HH-SLD	*'Hammer-Head'* Superluminescent Diode
HR	High-Reflection
IBE	Ion Beam Etched
LD	Laser Diode
LED	Light Emitting Diode
L.H.S.	Left Hand Side
LI	Light-Current
LOC	Large Optical Cavity
MMF	Multi-Mode Fibre
MOVPE	Metal Organic Vapour Phase Epitaxy
NA	Numerical Aperture
NF	Near Field
OCT	Optical Coherence Tomography
OTDR	Optical Time Domain Reflectometry
OSA	Optical Spectrum Analyser
P-SLD	Parabolic Superluminescent Diode

QD	Quantum Dot
QW	Quantum Well
R.H.S.	Right Hand Side
RI	Refractive Index
s/c	Semiconductor
SG	Super Gaussian
SLD	Superluminescent Diode
SMF	Single-Mode Fibre
SOA	Semiconductor Optical Amplifier
S-SLD	Stripe Superluminescent Diode
TEC	Thermo-Electric Cooler
T-SLD	Tapered Superluminescent Diode
WDM	Wavelength Division Multiplexing
W-P	Wall-Plug
WS	Wide Stripe

List of Symbols

α_f	Free-carrier absorption loss in cladding layer
α_S	Scattering loss coefficient
A	Area of contact region
B_r	Bimolecular recombination coefficient
c	Speed of light
d	Active layer thickness
δ_f	Forward travelling photon density
δ_r	Reverse travelling photon density
E_x	Electric field component
E_g	Bandgap energy
E^e	Electron energy
E^h	Hole energy
E_{Fe}	Electron quasi-Fermi level
E_{Fh}	Hole quasi-Fermi level
E_c	Energy level of conduction band
E_v	Energy level of valence band
$f^e(E^e)$	Occupation probability of an electron in conduction band
$f^h(E^h)$	Occupation probability of a hole in valence band
FF_y	Vertical far field pattern
g	Material gain
g_m	Modal optical gain
Γ	Confinement factor
$\hbar\omega$	Photon energy
h	Planck's constant
I	Injection current
I_{th}	Threshold current
J	Current density
k_B	Boltzmann's constant
L	Length of injection contact
N	Carrier density
N_{tr}	Carrier density at material transparency

n	Refractive index
n_{eff}	Effective refractive index
n_c	Effective density of states in conduction band
n_v	Effective density of states in valence band
P_{IN}	Input signal intensity
P_{sp}	Forward travelling spontaneous emission contribution
P	Forward travelling photon density
Q	Reverse travelling photon density
Q_{sp}	Reverse travelling spontaneous emission contribution
q	Magnitude of electronic charge
R_0	Effective facet reflectivity (z=0)
R_L	Output facet reflectivity (z=L)
s	Length of ray
T	Temperature
τ_{sp}	Spontaneous recombination lifetime
θ_C	Critical angle for total internal reflection
v	Group velocity
W	Width of injection contact
x	Dimension in Cartesian coordinate system
y	Dimension in Cartesian coordinate system
z	Dimension in Cartesian coordinate system

Acknowledgments

First and foremost I'd like to thank my supervisor Dr. Federica Causa who has patiently put up with me for nigh on four years. All the questions have finally been asked and answered. A better supervisor there is not.

I'd also like to thank Dr. J. Sarma for all the stimulating chats and stories he has entertained me with throughout my studies. Also, I've never tasted an egg curry or a sloppy quite as spectacular. I'll be back to pick up my BBQ set one day.

My thanks go to Bookham Technology (and Marconi) and the EPSRC for funding my research.

To my device fabrication instructor and good friend Trevor Ryan I'd like to offer my humble thanks. You're patience is legendary. I hope you enjoy your retirement.

To all my friends, old and new, too many to name but a selected few: Aggelos, Delia, Mr Woo, Nicola, Jon, Harry, Jay, Dave, and last but by no means least Shalini (my guardian angel), I offer you my thanks, my love and I'll see you anon.

Thanks go to my parents for providing me with all the support and love I needed to finally reach this goal.

Lastly, to my darling Aphroditi, I couldn't have done this without you. You are everything to me.

Chapter 1
Introduction

The aim of this chapter is to provide the reader with an introduction to Superluminescent Diodes and to explain the purpose and objectives of this thesis. The chapter begins with an extensive review of the literature on SLDs and the main applications in which SLDs are now commonly used (Sections 1.1 to 1.3). The aims and objectives of the thesis are discussed in Section 1.4, concluding with the thesis layout.

1.1: Superluminescent Diodes – a review

The Superluminescent Diode (SLD) is an edge-emitting double-heterostructure (DH) semiconductor (s/c) optical source that emits light with a relatively broad spectral linewidth. The low coherence length and the possibility to achieve high power operation makes SLDs suitable for various applications including Optical Coherence Tomography (OCT), [1-1]-[1-4], Optical Time Domain Reflectometry (OTDR), [1-5], Fibre Optic Gyroscopes (FOGs), [1-6], [1-7], sensing, [1-8], [1-9], Wavelength Division Multiplexing (WDM) systems, [1-10]-[1-12], and short haul communications.

Superluminescent operation is achieved by the amplification of the spontaneous emission in a medium with positive optical gain (Amplified Spontaneous Emission, ASE). In the schematic of Figure 1.1 the Light-Current (LI) curve expected from a typical SLD is compared to that expected from typical Light Emitting Diodes (LEDs) and Laser Diodes (LDs). At low currents the SLD LI curve is linear (similar to that of LEDs) but the output power is very low because the absorption is still significant. Above transparency the onset of superluminescence is characterised by the typical 'knee' in the LI curve, when the characteristic is superlinear. When optical gain saturation becomes significant saturation is observed in the sublinear characteristic of the LI curve. In some cases thermal roll-over is also observed. However, to realise a high-power SLD the most important issue to address is the suppression of lasing. The various methods that have been used will be discussed in the following sections to review the relevant literature.

The first SLD was accidentally realised in 1971 by Kurbatov et al., [1-13], in an attempt to increase LD output power. Kurbatov hypothesised that reducing optical

feedback in a LD would prevent catastrophic degradation by eliminating localised emission at the device facet. In fact, at low driving currents lasing was prevented by the effective low facet reflectivity and superluminescent operation was observed. However, the homojunction diodes used by Kurbatov bear little resemblance to modern day devices as testing was carried out under extreme conditions (T≈75°K) with extremely high injection currents (I=750A).

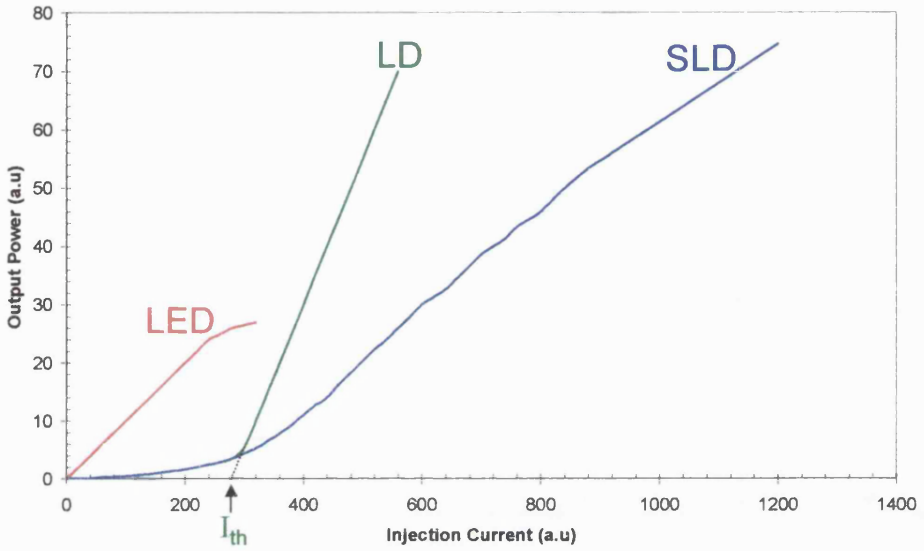

Figure 1.1: *Schematic representation of the LI characteristics expected from LEDs, LDs and SLDs.*

The first practical SLD was produced in 1973 by Lee et al., [1-14], and was fabricated from GaAlAs/GaAs DH material with testing carried out at room temperature. Lee introduced an absorption region into a device configuration similar to a stripe injection LD, Figure 1.2. The absorption region reduces optical feedback provided by the reflectivity of the (cleaved) crystal facets and results in SLD operation. An absorption region is simple to include in the device design and fabrication and, hence, it is a commonly used method for reducing facet reflectivity, [1-15]-[1-18]. However, an absorption region is not ideal for high power operation because at high injection current densities it becomes optically pumped and, therefore, feedback from the rear facet becomes sufficient to sustain laser operation. One method for reducing the accumulation of photo-excited carriers requires the addition of a grounded absorption region electrode, Figure 1.3, [1-19], [1-20]. A deep etch between the two electrodes is necessary to prevent a short-circuit.

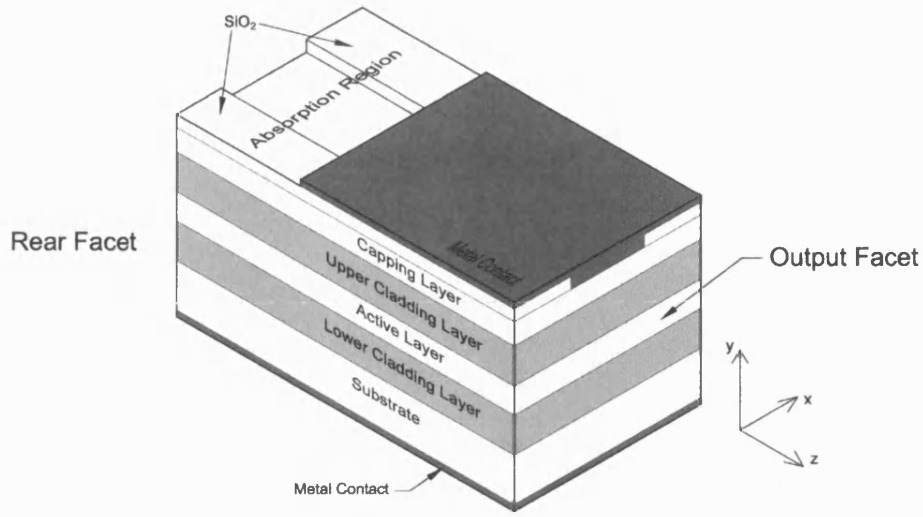

Figure 1.2: *Schematic of the first SLD fabricated from DH s/c material.*

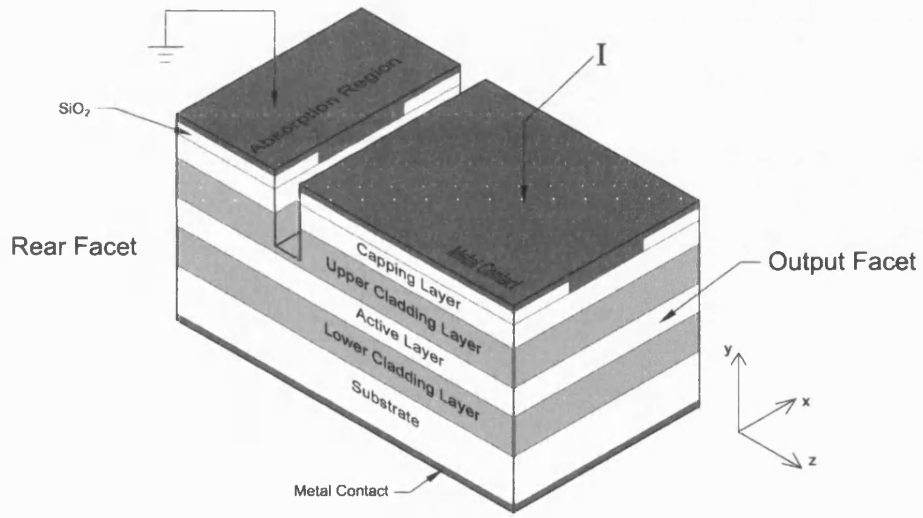

Figure 1.3: *Schematic of a SLD using an absorption region electrode to reduce optical pumping.*

Another and more common method to reduce optical feedback is to apply an Anti-Reflection (AR) coating onto one facet of the SLD. An AR coating is applied to a SLD by either sputtering or evaporating a thin film (usually one quarter wavelength) of material onto the output facet. The most widely reported materials used for AR coating are Aluminium Oxide (Al_2O_3), [1-21], Silicon Nitride (Si_3N_4), [1-22], [1-23], Silicon Oxide (SiO_x), [1-24], and Zirconium Oxide (ZrO_2), [1-25], which can reduce facet reflectivities to 0.1% – 2%.

In 1983 Kaminow et al., [1-26], replaced the absorption region with a High-Reflection (HR) coating (>90%) by evaporating gold onto the rear facet of a SLD. The HR coating, used in conjunction with an AR coated output facet, was useful to improve the effective output efficiency of a SLD by reducing the optical power lost in the absorption region, Figure 1.4. However, the product of the power reflectivity of the rear and front facets was designed to remain below 0.1% to realise significant superluminescent gain without laser operation. To achieve this, sophisticated multi-layer AR coatings with reflectivities of 0.02% were produced, [1-27]-[1-29]. The resulting SLDs were relatively efficient (wall plug efficiency of 6.5%), with relatively high output powers (350mW pulsed), [1-29]. However, at higher injection currents severe spectral modulation and, eventually, lasing were observed.

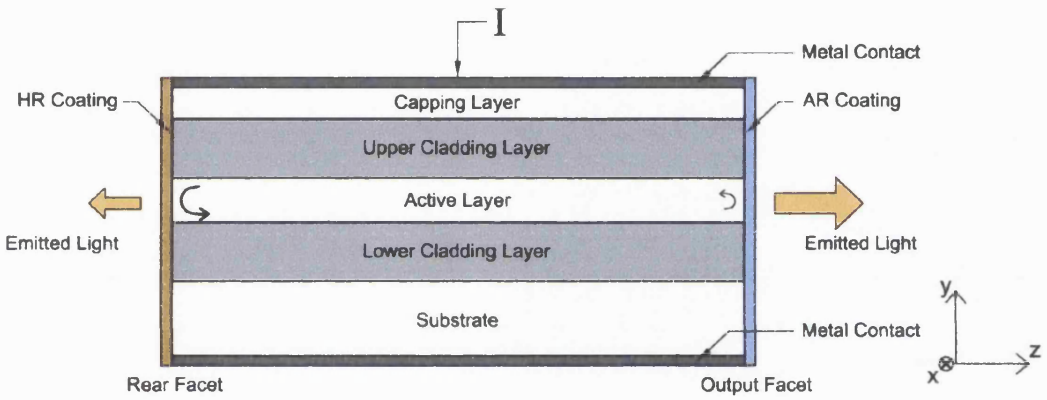

Figure 1.4: *Schematic of a SLD with HR coated rear and AR coated front (output) facets.*

Alternative methods of reducing effective facet reflectivity, without the need for long absorption regions or high quality AR coatings, include angling or bending the injection contact with respect to the output facet and etching v-groove deflectors behind the active region. Angled and bent injection contacts are designed to prevent optical feedback into the active region, Figure 1.5 (a) and (b), respectively. By angling or bending the stripe contact at an angle θ=5-7° with respect to the facet normal the combined effective power reflectivity was measured to be less than 0.0001%, [1-30]-[1-33]. With such low facet reflectivity angled contact SLDs can be operated at relatively large current densities (<3kAcm^{-2}) whilst still maintaining moderately low spectral modulation (>3%), [1-34]. However, a drawback associated with this category of SLDs is that the spatial output field profile is asymmetric and emerges at an angle with respect to the facet normal (e.g., 25° for θ=7°) making coupling to the fibre difficult.

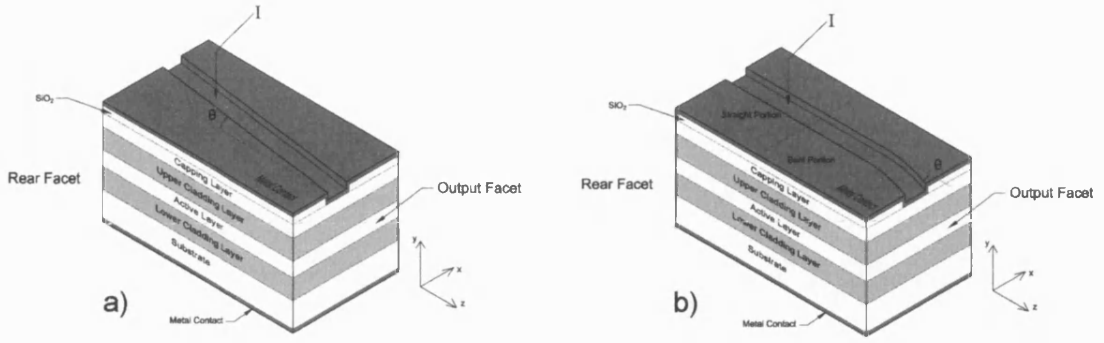

Figure 1.5: *a) SLD with the stripe injection contact at an angle θ with respect to the facet normal; b) SLD with a bent injection contact.*

The etched v-groove deflector introduced by Middlemast et al., [1-35], is a simple and inexpensive method for effectively reducing the rear facet reflectivity even for high power operation. In [1-35] the rear deflector was fabricated by chemically etching a v-groove through the active layer at 10° to the $(01\bar{1})$ plane, Figure 1.6. The v-groove deflects light travelling towards the rear facet out of the active layer into the substrate. Differently from the case of the rear absorption region discussed above, the efficiency of the etched deflector is not reduced by optical pumping and, therefore, SLD operation with low spectral modulation (~1%) can be maintained also at high injection current densities.

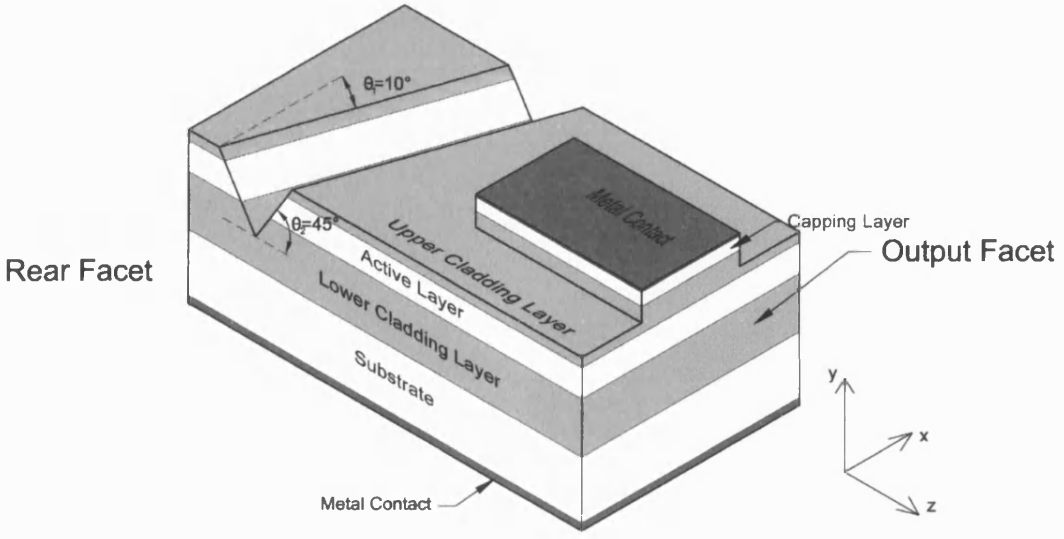

Figure 1.6: *Schematic of a SLD with an etched v-groove deflector.*

Significant improvement to the operating efficiency of SLDs was introduced with the tapered contact geometry, [1-35], [1-36], and in particular the angled taper geometry, Figure 1.7, discussed in [1-37] - [1-39]. With respect to the stripe geometry the advantage of the taper geometry is that the optical gain saturation in the active region is reduced especially at high current densities because optical feedback and, consequently, carrier depletion at the rear of the device, are reduced. In addition, the taper geometry is typically characterised by a broad output facet width (typically W≈100μm) which is practical to reduce the risk of Catastrophic Optical Damage (COD) at high power densities. High output powers, of the order of 1W, have therefore been achieved with taper and/or angled taper geometry SLDs, [1-35], [1-36], [1-38] and [1-40].

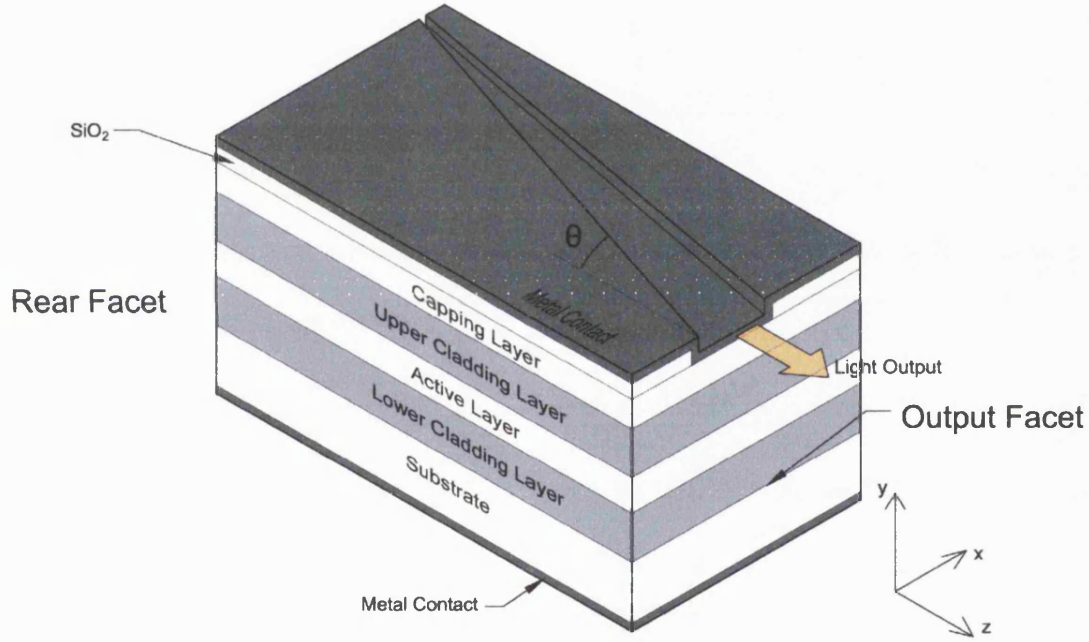

Figure 1.7: *Schematic of an angled taper contact geometry SLD.*

The taper contact geometry is also used for integrated SLD devices consisting of two regions: the Stripe-SLD (S-SLD) and the tapered Semiconductor Optical Amplifier (SOA), which are electrically pumped separately, Figure 1.8(a), [1-41]. Both regions are grown on the same wafer, with 100% coupling efficiency between them. The light emitted from the S-SLD is amplified by the SOA to produce relatively high output powers, [1-42]. To suppress lasing both facets of the integrated SLD are AR coated or, alternatively, the S-SLD and SOA are positioned at an angle with respect to the facets, [1-43].

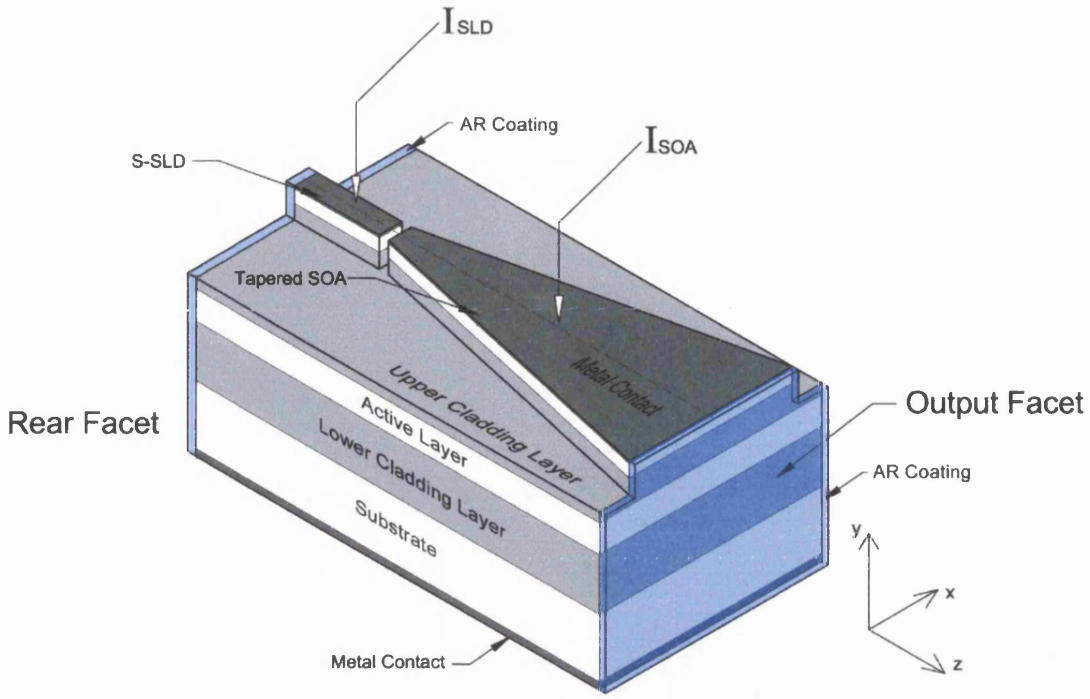

Figure 1.8: *Schematic of an integrated SLD: I_{SLD} is the injection current in the S-SLD; I_{SOA} is the injection current in the SOA.*

1.2: Recent developments

Recent developments described in the literature have been typically aimed at broadening the spectral width of SLDs by using specially designed Quantum Well (QW) and Quantum Dot (QD) materials. In fact, broadband SLDs are characterised by a short coherence length, and therefore, can be extremely useful to reduce Rayleigh backscattering in FOGs or to increase spatial resolution in OCT systems. In addition, for WDM systems, a broad wavelength range results in more spectrally sliced channels for data transmission and, hence, an increase in the system bandwidth. Several methods are available for increasing the spectral bandwidth of QW materials. These include segmenting the contact region of the SLD, [1-44], [1-45], QW intermixing by ion implantation [1-46], varying the material composition of multiple QWs, [1-47], and varying the width of QWs with the same material composition, [1-48]-[1-50]. Spectral bandwidths of approximately 100nm have been reported for SLDs emitting in the near infrared region (λ=1.5μm). However, typical problems that can arise with such sources, as discussed in [1-49], is that the output spectrum is irregular in shape and changes

significantly with driving current unless the material is carefully designed and grown, e.g., the SLDs fabricated from QD material described in [1-51]-[1-54].

1.3: Applications

SLDs are suitable for applications that require high-power optical sources with relatively high spatial and low temporal coherence. The SLD is most commonly used for OCT which is an in vivo imaging technique that uses optical interference to sense reflections from tissue homogeneities, [1-1]. A broadband source with a Gaussian-like profile increases the resolution and quality of OCT images. The depth of the image depends on the power coupled from the source into a single mode fibre, with typical useful powers of the order of a few milliwatts at IR wavelengths, [1-3].

For sensing applications including FOGs, [1-7], and force detection, [1-8], the light from an optical source is coupled to a single mode fibre. Signal noise, caused by Rayleigh backscattered light from the facet of the fibre, is reduced by using optical sources with low temporal coherence. Coupled powers of ~2mW into the single mode fibre are commonly reported for sensing applications with spectral widths of ~15nm at λ_{PEAK}=850nm, [1-7].

Spectrum slicing is a WDM technique in which narrow spectral bands are filtered from a broadband source. However, the filtering process severely reduces the output power available from an optical source resulting in low power sources like LEDs unsuitable for WDM applications. At present, SLDs with a spectral width of 50nm centred at λ_{PEAK}=1280nm are spectrally sliced into sixteen wavelength components. The coupled power into a single mode fibre from each component is approximately 0.3mW (CW).

1.4: Objectives and layout of this thesis

The main aim of this thesis is to investigate the properties of high-power SLDs with the purpose of improving device efficiency. The following objectives have been achieved during the course of this research programme:

- design, fabrication and characterisation of SLDs with various geometries;
- development of wavelength-dependent rate equation model to accurately simulate the light-current characteristics of SLDs with stripe or unconventional geometry;

- development of a ray model to simulate near and far field intensity profiles of SLDs of any geometry;
- wherever possible the experimental results have been interpreted using results from the in-house developed models;
- experimental estimate of SLD-to-fibre coupling efficiency by butt-coupling and by using a system of lenses;
- design and development of two new SLD designs to increase the power output and to achieve linear power-current characteristics.

This thesis is structured as follows:

Chapter 2 Description of semiconductor, QW material used to fabricate all devices discussed in this thesis. Detailed discussion of SLD operation with particular emphasis on optical gain and spontaneous emission contribution to ASE. Introduction of ray model to produce power-current characteristic curves, output spectra, photon and carrier density profiles for SLDs of any geometry. Flow diagrams are included to clarify the basic methods used in the model.

Chapter 3 Detailed description of ray model developed to simulate near and far field intensity profiles of SLDs of any geometry. Current spreading, carrier diffusion and optical saturation are included in the model by assuming a non-uniform two-dimensional carrier distribution.

Chapter 4 Experimental characterisation of stripe and tapered geometry SLDs. The measured profiles are interpreted in the context of the theoretical results predicted with the models presented in the preceding Chapters. The characterisation of parabolic geometry SLDs is also extensively discussed and comparisons with the theoretical model offer an excellent opportunity to validate the models described in the previous Chapters. An investigation into improving SLD efficiency is presented by analysing the effect of optical gain saturation on the device operational characteristics. The following device parameters have been analysed in detail from the theoretical and experimental point of view, to improve device efficiency: the output facet reflectivity (by applying AR coating), the device length and the presence of (effective) index-guiding regions along the length of the device.

Chapter 5 Coupling of in-house fabricated SLDs to multi-mode and single-mode optical fibres. Two coupling techniques have been used in the laboratory: butt-coupling and coupling using a system of lenses. The experimental results obtained using the above two techniques are presented together with a qualitative description of system losses. The advantage of using a refractive index matching gel with the butt-coupling technique is described. In particular experimental results obtained for the butt-coupling

efficiency seem to be in good agreement with the theoretical estimates calculated with the ray model.

Chapter 6 Two new SLD designs, namely the SLD arrays and the *'hammer-head'* SLDs, are presented. Justifications for the development of such new devices and the experimental characterisation obtained from in-house fabricated prototypes are presented in detail and interpreted using theoretical results obtained with the models developed in-house.

Chapter 7 Conclusions drawn from the research presented in this thesis and suggestions for future work.

References

[1-1] Tripathi R., Nassif N., Nelson S., Park B. H., and F.de Boer J., *Spectral Shaping for Non-Gaussian Source Spectra in Optical Coherence Tomography*, Optics Letters, Vol. 27, No. 6, March 2002, pp. 406-408.

[1-2] Podoleanu A. Gh., Rogers J. A., and Jackson D. A., *OCT En-face Images from the Retina with Adjustable Depth Resolution in Real Time*, IEEE Journal of Selected Topics in Quantum Electronics, Vol. 5, No. 4, July/August 1999, pp. 1176-1184.

[1-3] Ko T.H., Adler D.C., and Fujimoto J.G., *Ultrahigh Resolution Optical Coherence Tomography Imaging with a Broadband Superluminescent Diode Light Source*, Optics Express, Vol. 12, No. 10, May 2004, pp. 2112-2119.

[1-4] Mehta D. S., Sugai M., Hinosugi H., Saito S., Tekeda M., Kurokawa T., Takahashi H., Ando M., Shishido M., and Yoshizawa T., *Simultaneous Three-Dimensional Step-Height Measurement and High-Resolution Tomographic Imaging with a Spectral Interferometric Microscope*, Applied Optics, Vol. 41, No. 19, July 2002, pp. 3874-3884.

[1-5] Takada K., Yokohama I., Chida K., and Noda J., *New Measurement System for Fault Location in Optical Waveguide Devices Based on an Interferometric Technique*, Applied Optics, Vol. 26, No. 9, May 1987, pp. 1603-1606.

[1-6] Bohm K., Marten P., Petermann K., Weidel E., and Ulrich R., *Low Drift Fiber Gyro using a Superluminescent Diode*, Electronics Letters, Vol. 17, 1981, p.352.

[1-7] Burns W. K., Chen C.-L., and Moeller R. P., *Fiber-Optic Gyroscopes with Broad-Band Sources*, Journal of Lightwave Technology, Vol. LT-1, No. 1, March 1983, pp. 98-105.

[1-8] Budakian R., and Putterman S.J., *Force Detection using a Fiber-Optic Cantilever*, Applied Physics Letters, Vol. 81, No. 11, September 2002, pp. 2100-2102.

[1-9] Bock W.J., Nawrocka M.S., and Urbanczyk, *Universal Readout System for Temperature, Elongation and Hydrostatic Pressure Sensors Based on Highly Birefringent Fibers*, IEEE Transactions on Instrumentation and Measurement, Vol. 53, No. 1, February 2004, pp. 170-174.

[1-10] Sampson D. D., and Holloway W. T., *100mW Spectrally-Uniform Broadband ASE Source for Spectrum-Sliced WDM Systems*, Electronics Letter, Vol. 30, No. 19, September 1994, pp. 1611-1612.

[1-11] Mikulla B., Leng L., Sears S., Collings B. C., Arend M., and Bergman K., *Broad-Band High-Repetition-Rate Source for Spectrally Sliced WDM*, IEEE Photonics Technology Letters, Vol. 11, No. 4, April 1999, pp. 418-420.

[1-12] Glance B., Liou K.-Y., Koren U., Burrows E. C., Raybon G., Burrus C. A., Dreyer K., and Doerr C., *A Single-Fiber WDM Local Access Network Based on Amplified LED Transceivers*, IEEE Photonics Technology Letters, Vol. 8, No. 9, September 1996, pp. 1241-1242.

[1-13] Kurbatov L. N., Shakhidzhanov S. S., Bystrova L. V., Krapukhin V. V., and Kolonenkova S. I., *Investigation of Superluminescence Emitted by Gallium Arsenide Diode*, Soviet Physics – Semiconductors, Vol. 4, No.11, May 1971, pp. 1739-1743.

[1-14] Lee T.-P., Burrus C. A., JR., and Miller B. I., *A Stripe-Geometry Double-Heterostructure Amplified-Spontaneous-Emission (Superluminescent) Diode*, IEEE Journal of Quantum Electronics, Vol. QE-9, No. 8, August 1973, pp. 820-828.

[1-15] Kwong N. S. K., Lau K. Y., and Barchaim N., *High-Power High-Efficiency GaAlAs Superluminescent Diodes with Internal Absorber for Lasing Suppression*, IEEE Journal of Quantum Electronics, Vol. 25, 1989, pp. 696-704.

[1-16] Joindot I.M., and Boisrobert C. Y., *Peculiar Features of InGaAsP DH Superluminescent Diodes*, IEEE Journal of Quantum Electronics, Vol. 25, No. 7, July 1989, pp. 1659-1665.

[1-17] Imanaka K., *Cavity Length Dependence of Optical Characteristics in High Power Narrow Stripe GaAs Superluminescent Diodes*, IEEE Photonics Technology Letters, Vol.2, No. 10, October 1990, pp. 705-707.

[1-18] Patterson B. D., Epler J. E., Graf B., Lehmann H. W., and Sigg H. C., *A Superluminescent Diode at 1.3μm with Very Low Spectral Modulation*, IEEE Journal of Quantum Electronics, Vol. 30, No. 3, March 1994, pp. 703-712.

[1-19] Kwong N. S. K., Bar-Chaim N., and Chen T. T., *High-Power 1.3μm Superluminescent Diode*, Applied Physics Physics Letters, Vol. 54, 1989, pp. 298-300.

[1-20] Okamoto H., Wada M., Sakai Y., Hirono T., Kawaguchi Y., Kondo Y., Kadota Y., Kishi K., and Itaya Y., *A Narrow Beam 1.3-μm-Super Luminscent Diode Integrated with a Spot-Size Converter and a New Type Rear Absorbing Region*, Journal of Lightwave Technology, Vol. 16, No. 10, October 1998, pp. 1881-1887.

[1-21] Dutta N. K., and Deimel P. P., *Optical Properties of a GaAlAs Superluminescent Diode*, IEEE Journal of Quantum Electronics, Vol. QE-19, No. 4, April 1983, pp. 496-498.

[1-22] Eisenstein G., and Stulz L. W., *High Quality Antireflection Coating on Laser Facets by Sputtered Silicon Nitride*, Applied Optics, Vol. 23, No. 1, January 1984, pp. 161-163.

[1-23] Dutta N. K., Nelson R. J., Wright P. D., Besomi P., and Wilson R. B., *Optical Properties of a 1.3-μm InGaAsP Superluminescent Diode*, IEEE Transactions on Electron Devices, Vol. ED-30, No.4, April 1983, pp. 360-363.

[1-24] Zhao Y., Liu Y., Jiang X., Wang Z., Liu B., Xing J., Sun Z., Zhang X., Du G., *Comparison of Two Kinds of AlGaAs Terraced Substrate Inner Stripe Superluminescent Diodes*, pp. 1685-1689.

[1-25] Mamedov D. S., Prokhorov V. V., and Yakubovich S. D., *Superbroadband High-Power Superluminescent Diode Emitting at 920nm*, Quantum Electronics, Vol. 33, No. 6, 2003, pp. 471-473.

[1-26] Kaminow I. P., Eisenstein G., Stulz L. W., and Dentai A. G., *Lateral Confinement InGaAsP Superluminescent Diode at 1.3μm*, IEEE Journal of Quantum Electronics, Vol. QE-19, No. 1, January 1983, pp. 78-81.

[1-27] Kaminow I. P., Eisenstein G., and Stulz L. W., *Measurement of the Modal Reflectivity of an Antireflection Coating on a Superluminescent Diode*, IEEE Journal of Quantum Electronics, Vol. QE-19, No. 4, April 1983, pp. 493-495.

[1-28] Morrison C.B., Zinkiewicz L. M., Niesen J., and Figueroa L., *High-Power Superluminescent Diode with Reduced Coherence Length*, Electronics Letter, Vol. 21, No. 19, September 1985, pp. 840-841.

[1-29] Paoli L., Burnham R. D., and Smith D. L., *High-Power Superluminescent Light-Emitting Diodes with Ultra-Reflectivity Facet Coatings*, IEEE Transactions on Electron Devices, Vol. ED-32, No. 11, November 1985, p. 2534.

[1-30] Sugo M., Shibata Y., Kamioka H., Yamamoto M., and Tohmori Y., *High-power (>50mW) and wideband (>50nm) 1.3μm super-luminescent diodes*, Electronics Letters, Vol. 41, No. 8, April 2005.

[1-31] Takayama T., Imafuji O., Kouchi Y., and Yuri M., *100-mW High-Power Angled-Stripe Superluminescent Diodes with a New Real Refractive-Index-Guided Self-Aligned Structure*, Journal of Quantum Electronics, Vol. 32, No. 11, November 1996, pp. 1981-1986.

[1-32] Fu L., Schweizer H., Zhang Y., Li L., Baechle A. M., Jochum S., Bernatz G. C., and Hansmann S., *Design and Realization of High-Power Ripple-Free*

Superluminescent Diodes at 1300nm, IEEE Journal of Quantum Electronics, Vol. 40, No. 9, September 2004, pp. 1270-1274.

[1-33] Lin C.-F., and Juang C.-S., *Superluminescent Diodes with Bent Waveguide*, IEEE Photonics Technology Letters, Vol. 8, No. 2, February 1996, pp. 206-208.

[1-34] Tsai C.-H., Su Y.-S., Tsai C.-W., Tsai D. P., and Lin C.-F., *High-Power Angled Broad-Area 1.3μm Laser Diodes with Good Beam Quality*, IEEE Photonics Technology Letters, Vol. 16, No. 11, November 2004, pp. 2412-2414.

[1-35] Middlemast I., Sarma J., and Yunu S., *High Power Tapered Superluminescent Diodes Using Novel Etched Deflectors*, Electronics Letters, Vol. 33, No. 10, May 1997, pp. 903-904.

[1-36] Linder N., Butendeich R., Karnutsch C., Schmid W., Tautz S., Streubel K., Rurländer S., Schweizer H., and Scholz F., *900mW Continuous Wave Operation of AlInGaP Tapered lasers and Superluminescent Diodes at 640nm*, Conference on Lasers and Electro-Optics, Vol. 1, May 2004, pp. 667-668.

[1-37] Koyama F., Liou K.-Y., Dentai A. G., Tanbun-ek T., and Burrus C. A., *Multiple-Quantum-Well GaInAs/ GaInAsP Tapered Broad-Area Amplifiers with Monolithically Integrated Waveguide Lens for High-Power Applications*, IEEE Photonics Technology Letters, Vol. 5, No. 8, August 1993, pp. 916-919.

[1-38] Yamatoya T., Mori S., Koyama F., and Iga K., *High Power GaInAsP/InP Strained Quantum Well Superluminescent Diode with Tapered Active Region*, Journal of Applied Physics, Vol. 38, November 1999, pp. 5121-5122.

[1-39] Yunus S., *Development and Study of High Power Tapered Geometry Superluminescent Diodes*, PhD Thesis, University of Bath, 2002.

[1-40] Burrow L.D., Causa F., and Sarma J., *1.3W Ripple-free Superluminescent Diodes*, IEEE Photonics Technology Letters, accepted May 2005.

[1-41] Zhao Y., Devane G., Sun Z., Stair K.A., Liu Y., Du G., and Chang R.P.H., *The Embryonic Form of the Integrated Superluminescent Diode*, Semiconductor Science Technology, Vol. 12, 1997, pp. 567-579.

[1-42] Du G., Xu C., Liu Y., Zhao Y., and Wang H., *High-Power Integrated Superluminescent Light Source*, IEEE Journal of Quantum Electronics, Vol. 39, No. 1, January 2003, pp.149-153.

[1-43] Liu Y., Song J., Zeng Y., Wu B., Zhang Y., Qian Y., Sun Y., and Du G., *High-Power 1.5μm InGaAsP/InP Strained Quantum Wells Integrated Superluminescent Light Source with Tilted Structure*, Japanese Journal of Applied Physics, Vol. 40, No. 6A, June 2001, pp 4009-4010.

[1-44] Semenov A. T., Batovrin V. K., Garmash I. A., Shidlovsky V. R., Shramenko M.V., and Yakubovick S. D., *(GaAl0As SQW Superluminescent Diodes with*

Extremely Low Coherence Length, Electronics Letters, Vol. 31, No. 4, February 1995, pp. 314-315.

[1-45] Semenov A. T., Shidlovski V. R., Jackson D. A., Willsch R., and Ecke W., *Spectral Control in Multisection AlGaAs SQW Superluminescent Diodes at 800nm*, Electronic Letters, Vol. 32, No. 3, February 1996, pp. 255-256.

[1-46] Ong T.-K., Yin M., Yu Z., Chan Y.-C., and Lam Y.-L., *High Performance Quantum Well Intermixed Superluminescent Diodes*, Measurement Science and Technology, Vol. 15, May 2004, pp.1591-1595.

[1-47] Mikami O., Yasaka H., and Noguchi Y., *Broader Spectral Width InGaAsP Stacked Active Layer Superluminescent Diodes*, Applied Physics Letters, Vol. 56, No. 11, March 1990, pp. 987-989.

[1-48] Lin C.-F., Su Y.-S, Wu C.-H., and Shmavonyan G.S., *Influence of Separate Confinement Heterostructure on Emission Bandwidth of InGaAsP Superluminescent Diodes/Semiconductor Optical Amplifiers with Nonidentical Multiple Quantum Wells*, IEEE Photonics Technology Letters, Vol. 16, No. 6, June 2004, pp. 1441-1443.

[1-49] Lin C.-F., Wu B.-R., Laih L.-W., and Shih T.-T., *Sequence Influence of Nondentical InGaAsP Quantum Wells on Broadband Characteristics of Semiconductor Optical Amplifiers-Superluminescent Diodes*, Optics Letters, Vol.26, No. 14, pp. 1099-1101.

[1-50] Lin C.-F., Lee B.-L., and Lin P.-C., *Broad-Band Superluminescent Diodes Fabricated on a Substrate with Asymmetric Dual Quantum Wells*, IEEE Photonics Technology Letters, Vol. 8, No. 11, November 1996, pp.1456-1458.

[1-51] Zhang Z. Y., Wang Z. G., Xu B., Jin P., Sun Z. Z., and Liu F. Q., *High-Performance Quantum-Dot Superluminescent Diodes*, IEEE Photonics Technology Letters, Vol. 16, No. 1, January 2004, pp. 27-29.

[1-52] Heo D. C., Dong S. J., Choi W. J., Lee J. I., Jeong J. C., and Han I. K., *Characteristics of Superluminescent Diodes Utilizing $In_{0.5}Ga_{0.5}As$ Quantum Dots*, Japanese Journal of Applied Physics, Vol. 42, No. 8, August 2003, pp. 5133-5134.

[1-53] Heo D. C., Song J. D., Choi W. J., Lee J. I., Jung J. C., and Han I. K., *High Power Broadband InGaAs/ GaAs Quantum Dot Superluminescent Diodes*, Electronics Letters, Vol. 39, No. 11, May 2003, pp.863-865.

[1-54] Sun Z.-Z., Ding D., Gong Q., Zhou W., Xu B., and Wang Z.-G., *Quantum-Dot Superluminescent Diode: A Proposal for an Ultra-Wide Output Spectrum*, Optical and Quantum Electronics, Vol. 31, February 1999, pp. 1235-1246.

Chapter 2
Superluminescent Diode Structure and Operation

2.1: Introduction

In this Chapter the structure of SLDs and the optical properties relevant for SLD operation are presented. A model that simulates the Light-Current (LI) and spectral characteristic of different contact geometry SLDs is also presented.

The layer structure of the high-power QW s/c material used for SLD fabrication and corresponding vertical mode profiles are discussed in detail. The geometry and basic principles of operation of SLDs are discussed and compared with those of typical edge-emitting lasers.

The device model described in this chapter is based on the ray analysis to calculate the steady state longitudinal photon density distribution of a stripe geometry SLD (S-SLD). By solving the steady-state carrier conservation equation, the best approximation for a constant value of carrier density (N) is calculated for any injection current density. The photon distribution, the output power and the spectral characteristic of a SLD can then be calculated.

A method for adapting the ray model to simulate the characteristics of a longitudinally non-uniform geometry SLD, such as the tapered and parabolic SLD (T-SLD and P-SLD respectively), is presented in Section 2.9.

2.2: High-power semiconductor material structure

The SLDs presented in this thesis have been fabricated in-house from a MOVPE-grown, high power, Large Optical Cavity (LOC) strained InGaAs/GaAs/AlGaAs DH material with three 7.3nm QWs surrounded by 10nm GaAs barriers and is designated QT1614. The layer thickness, composition and doping information for QT1614 is summarised in Table 2.1. A detailed description of the fabrication procedure is described in Appendix A.

Table 2.1: *Epitaxial layers of the s/c QW material QT1614.*

Layer	Thickness	Composition	Doping	Dopant
Capping	0.18μm	GaAs	3.9×10^{19} cm^{-3}	Zn
Cladding	0.75μm	$Al_{0.41}$	2×10^{18} cm^{-3}	C
Guide	0.33μm	$Al_{0.2}$	undoped	
Barrier	100Å	GaAs	undoped	
QW	73Å	$In_{0.17}$/GaAs	undoped	
Barrier	100Å	GaAs	undoped	
QW	73Å	$In_{0.17}$/GaAs	undoped	
Barrier	100Å	GaAs	undoped	
QW	73Å	$In_{0.17}$/GaAs	undoped	
Barrier	100Å	GaAs	undoped	
Guide	0.33μm	$Al_{0.2}$	undoped	Si
Cladding	0.76μm	$Al_{0.41}$	9×10^{17} cm^{-3}	Si
Buffer	0.5μm	GaAs	1×10^{18} cm^{-3}	Si

To calculate the vertical mode profile supported by the s/c material the Effective Dielectric Constant (EDC) method is used, [2-1]. The vertical (y) (guided) mode profiles calculated for QT1614 are presented in Figure 2.1.

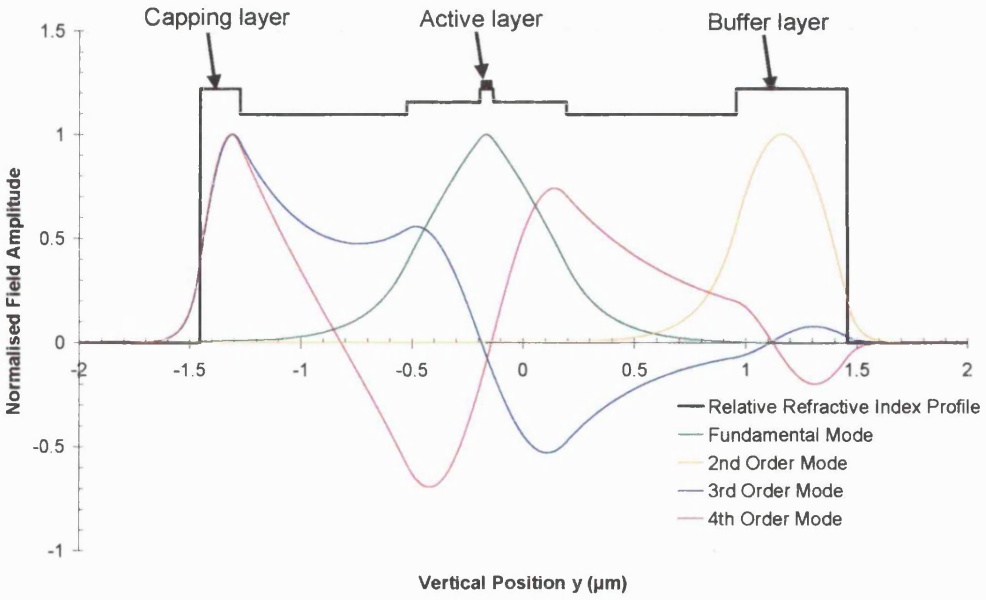

Figure 2.1: *Relative refractive index profiles for material QT1614 and corresponding vertical bound modes calculated with the EDC method.*

The vertical optical confinement factor, $\Gamma^{(m)}$, which is the fraction of optical power confined in the active layer, shown in Figure 2.2, is given by

$$\Gamma^{(m)} = \frac{\int_{-d/2}^{d/2} \left|E_x^{(m)}(y)\right|^2 dy}{\int_{-\infty}^{\infty} \left|E_x^{(m)}(y)\right|^2 dy} \tag{2.1}$$

where $E_x^{(m)}(y)$ is the electric field component of mode m and d is the active layer thickness.

From Figure 2.1 it is noted that the fundamental mode has the largest confinement factor in the active region and therefore the highest modal gain, as discussed in detail in Section 2.5.

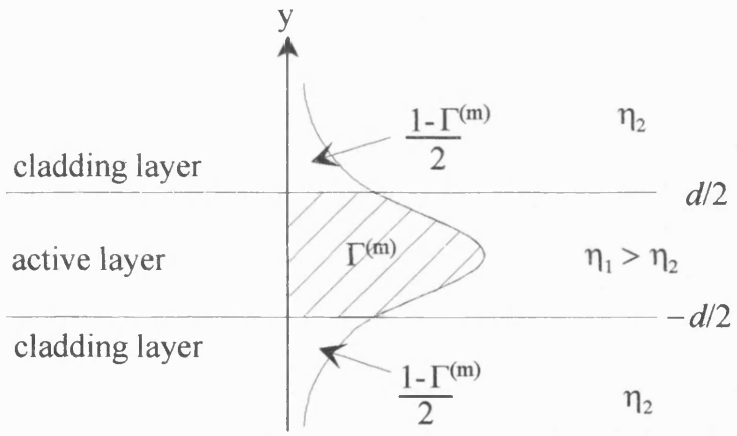

Figure 2.2: *Schematic showing the fundamental mode of a three layer symmetric slab waveguide. The hatched area shows the fraction of power of the mode confined to the active layer.*

A rib is ion beam etched into the capping and upper cladding layer to define the contact region of current injection. The rib is shallow so that there is no change in lateral effective refractive index but it is useful to reduce current spreading, Figure 2.3, [2-2].

The output facet of the device is cleaved. A groove with sides sloped at 45° with respect to the active layer (v-groove) is Ion Beam Etched (IBE) at the rear of the device to act as a deflector, Figure 2.4.

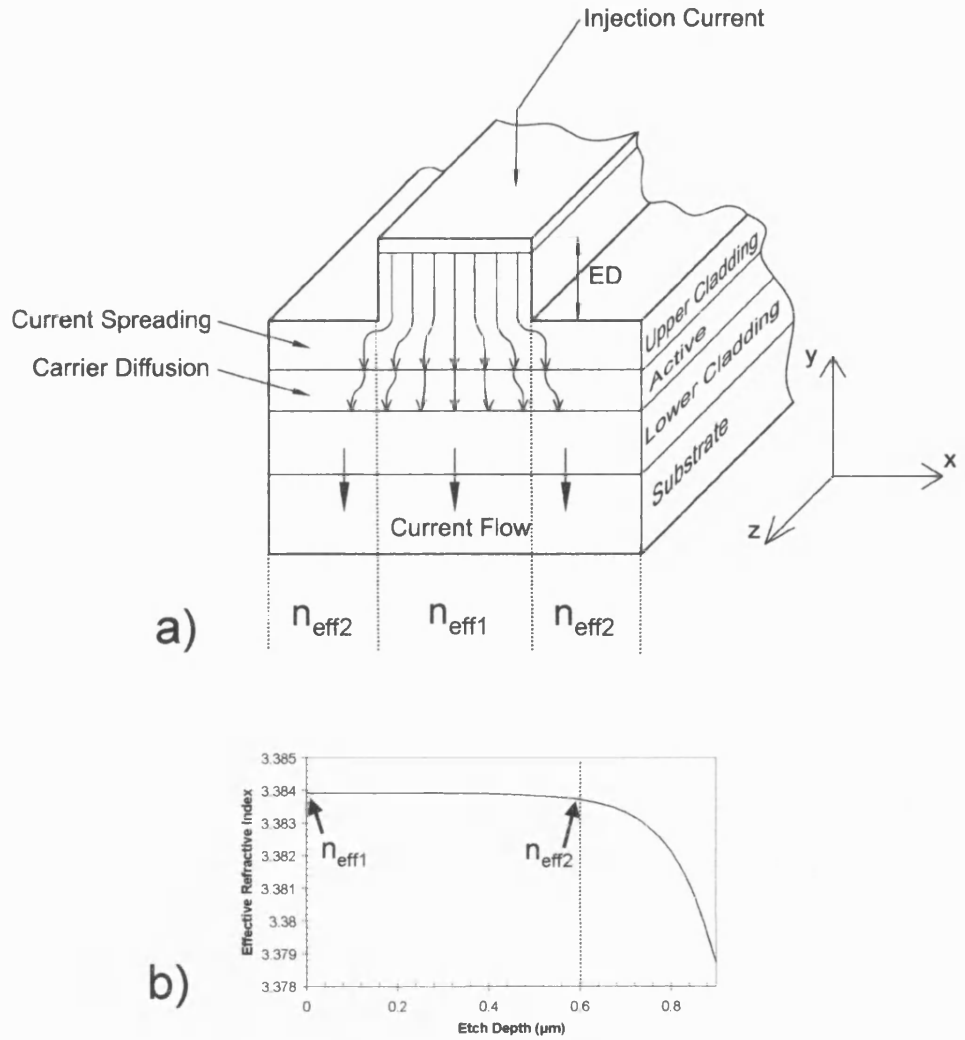

Figure 2.3: a) A *rib etched into the capping and upper cladding layers. ED is the etch depth.* n_{eff1} *and* n_{eff2} *are the effective refractive indices calculated with the EDC method. b) The variation of the effective refractive index as a function of the etch depth.*

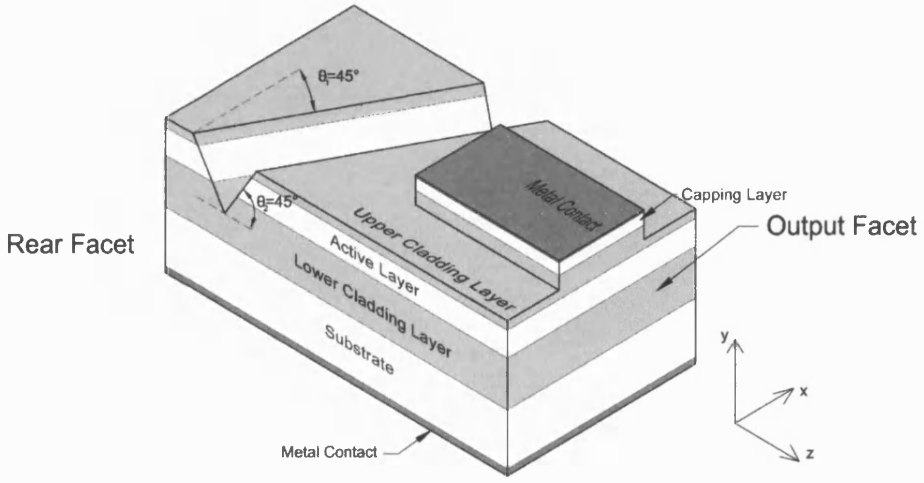

Figure 2.4: *Schematic of an in-house fabricated S-SLD with an etched v-groove deflector.*

2.3: SLD as a "Laser without a mirror"

A LD is an active optical oscillator, that is an optical amplifier with positive feedback. The positive feedback is provided by the reflectivity of the (cleaved) crystal facets, Figure 2.5a. To inhibit lasing in a cavity with gain it is necessary to avoid optical feedback, that is achieve zero reflectivity at one facet at least. Therefore, the resulting device will effectively be an optical amplifier of spontaneous emission (assuming no optical input), that is a SLD.

The SLDs described in this thesis have an absorption region designed at one end of the device to prevent the reflection of light back into the optical cavity, thereby eliminating the feedback. The absorption region for the SLDs takes the form of an etched v-groove deflector that deflects the backward travelling light into the substrate, Figure 2.5b, [2-3].

Because of the absence of feedback SLDs are incoherent optical sources, however it is to be noted that the spectral linewidth of a typical SLD is about an order of magnitude narrower than that of LEDs (e.g., the Burrus LED [2-4]) since SLDs operate with finite optical gain.

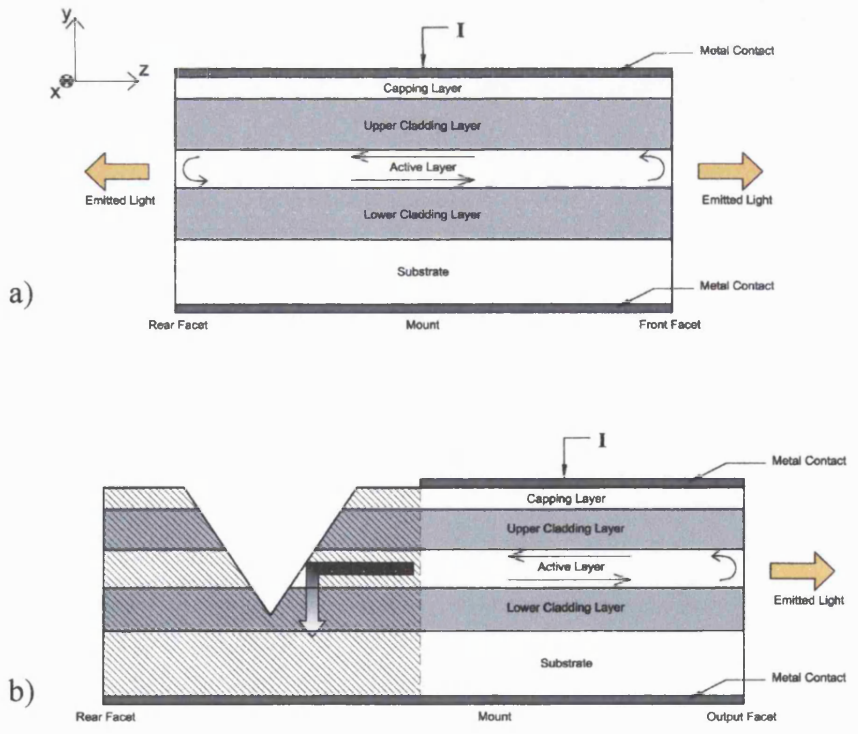

Figure 2.5: *Schematic illustrating the difference in operation between a LD and a SLD. In a), the LD is an oscillator. In b), the SLD has a lossy region to eliminate feedback.*

2.4: Optical gain in active semiconductor materials

Atoms in a s/c material are closely packed causing the energy levels of each atom to overlap and become indistinguishable from one another. The result is the transition of electrons from conduction to valence band over a broad spectral range, [2-5]. As a consequence the gain of the material changes with wavelength. The gain curves for a s/c material (gain as a function of photon energy, $\hbar\omega$) can be calculated by using the following expression:

$$g(\hbar\omega) = g_0 \frac{\sqrt{\hbar\omega - E_g}}{\hbar\omega}\left[f^e(E^e) + f^h(E^h) - 1\right] \qquad (2.2)$$

where g_0 is a material parameter that can be obtained from the literature, [2-5]; E_g is the bandgap energy; E^e is the energy of the electron; E^h is the energy of the hole; $f^e(E^e)$ is the occupation probability of an electron in the conduction band; $f^h(E^h)$ is the occupation probability of a hole in the valence band and $\hbar\omega$ is the photon energy.

To evaluate the gain in a material as a function of carrier density, N, the electron and hole quasi-Fermi levels, E_{Fe} and E_{Fh} respectively, must also be expressed in terms of N. The positions of the quasi-Fermi levels are calculated using the Joyce-Dixon approximation, [2-5],

$$E_{Fe} = E_c + k_B T\left[\ln\left(\frac{N}{n_c}\right) + \frac{1}{\sqrt{8}}\frac{N}{n_c}\right] \qquad (2.3a)$$

$$E_{Fh} = E_v + k_B T\left[\ln\left(\frac{N}{n_v}\right) + \frac{1}{\sqrt{8}}\frac{N}{n_v}\right] \qquad (2.3b)$$

where E_c and E_v are the energy levels of the conduction and the valence band respectively; N is the injected carrier density; k_B is Boltzmann's constant; T is temperature; n_c and n_v are the effective density of states in the conduction and valence bands and are material dependent.

By substituting the approximate values (2.3a) and (2.3b) for the quasi-Fermi levels into equation (2.2) it is possible to calculate the gain curves for any particular material once the value for g_o is known. The devices discussed in this thesis are fabricated from the s/c material described in Table 2.1. The gain curves obtained using

equation (2.2) for the $Ga_{0.83}In_{0.17}As$ active layer material are presented in Figure 2.6 for different values of injection carrier density (other material parameters used in the model are summarised in Table 2.2).

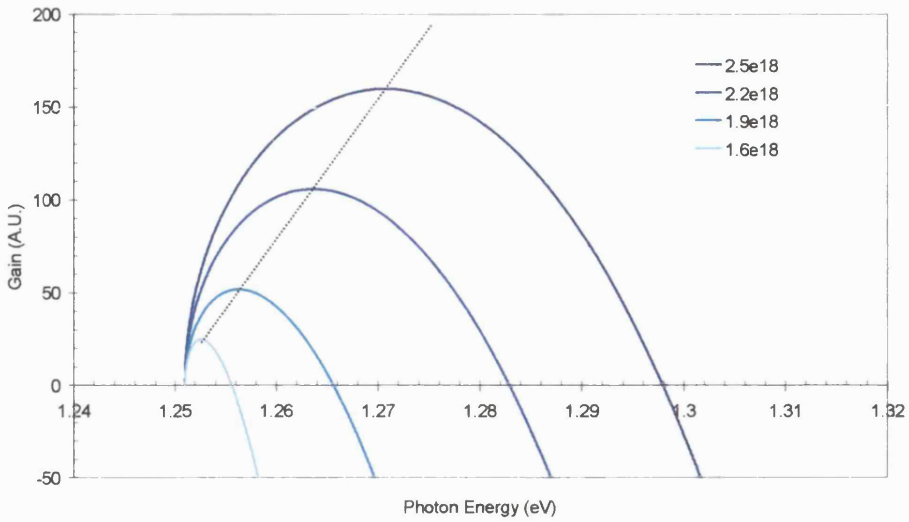

Figure 2.6: *Optical gain curves for $Ga_{0.83}In_{0.17}As$ material for various values of injection carrier density. The dotted line joins the maxima of the gain curves.*

The maximum value of the gain varies linearly with the injected carrier density, N, as follows:

$$g_{max} = A_0(N - N_{tr}) \tag{2.4}$$

where $A_0 \approx 1.5\times10^{-16}$ cm^2 and $N_{tr} \approx 1.45\times10^{18}$ cm^{-3} are material constants, Table 2.2. The theoretical differential gain (A_0) typically used for QW devices is ~10^{-15} cm^2 but experimental values are measured to be five times to one order of magnitude lower [2-6]. When $N = N_{tr}$ then g = 0, hence N_{tr} is known as the carrier density at material transparency. When the analysis of the device operation is done neglecting the wavelength dependence, then the value of g_{max} is generally used to describe the gain in the medium.

For QW structures a more accurate representation of optical gain is

$$g(N) = g_0 \ln (N / N_{tr}) \tag{2.5}$$

where g_0 is a material parameter. Equation (2.5) describes the non-linear gain effect at high current densities due to subband filling of the QW, [2-7]. However, in the device

model discussed in this chapter the saturation of the gain comes implicitly with the saturation of carriers. Also, for multiple QW materials, as used in this Thesis, the gain saturation caused by subband filling is significantly reduced. Therefore, for simplicity, equation (2.4) is used in the device model presented in section 2.8.

Table 2.2: *Material constants used to calculate the gain curves of Figure 2.6.*

Parameter	Value
g_0	5.7×10^{4}
A_0	1.5×10^{-16} cm^2
N_{tr}	1.45×10^{18} cm^{-3}

2.5: Modal gain

In an active device only the fraction of the mode in the active layer, defined by Γ in equation (2.1), is optically amplified. Therefore, the *modal gain* (g_m) is used to represent the net gain in a SLD:

$$g_m = \Gamma g + (1-\Gamma)\alpha_f + \alpha_s \qquad (2.6)$$

where g is the material gain, α_f is the free-carrier absorption (FCA) loss in the cladding layers and α_S is the scattering loss coefficient (cm^{-1}).

The FCA loss is equivalent to resistive loss and does not cause electron transitions. FCA is therefore only applicable if the optical signal wavelength is larger than that corresponding to the band gap of the material. Optical signals produced by emissions from within the active layer have energy larger or equal to the active layer band gap energy. The FCA term is neglected in the active layer, but not in the cladding layers. The mode can also suffer scattering losses due to rough surfaces between the active and cladding layers and that is accounted for by the loss coefficient α_S.

2.6: Spontaneous emission in a SLD

Photons produced by spontaneous emission are radiated isotropically and hence only a fraction (δ) of the photons produced will travel along the longitudinal (z) direction of the active region. The parameter δ is determined by the vertical refractive

index step between the cladding and the active layer and the stripe contact dimensions. The following expression is used to represent the fraction of spontaneous emission coupling to the forward and reverse travelling photon densities, δ_f and δ_r, respectively:

$$\delta_f = \delta_r = \frac{1}{2\pi}\frac{W}{L}\cos^{-1}\left(\frac{n_2}{n_1}\right) \tag{2.7}$$

where n_1 is the refractive index of the active layer; n_2 is the refractive index of the cladding layers; W is the width of the injection contact; L is the length of the injection contact. The derivations of δ_f and δ_r are summarised in Appendix B.

The spontaneous emission is wavelength-dependent and can be represented by a Gaussian curve $Z(\lambda)$, Figure 2.7, [2-8]. The expression for $Z(\lambda)$ is

$$Z(\lambda) = \frac{1}{\sqrt{2\pi}} e^{\left(\frac{-\lambda^2}{2a^2}\right)} \tag{2.8}$$

where a defines the width of the Gaussian curve.

The area under the curve $Z(\lambda)$ represents the total amount of spontaneous emission for a given injection current density:

$$G = \int_{\infty}^{-\infty} Z(\lambda)d\lambda \tag{2.9}$$

The fraction $\delta(\lambda)$ of spontaneous emission generated by a wavelength range $\Delta\lambda$ is obtained by

$$\delta(\lambda) = \frac{\Lambda\lambda}{G} \tag{2.10}$$

where $\Lambda\lambda$ is the spontaneous emission contribution for a wavelength range $\Delta\lambda$ and is given by

$$\Lambda\lambda_{\Lambda\lambda} = \int_{\lambda}^{\lambda+\Delta\lambda} Z(\lambda)d\lambda \tag{2.11}$$

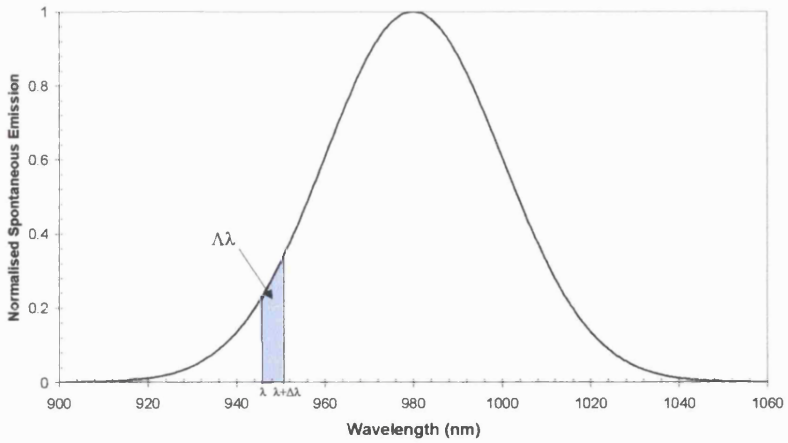

Figure 2.7: *The normalised spontaneous emission calculated for a GaInAs SLD as a function of wavelength. The peak of the Gaussian curve matches the peak wavelength for $Ga_{0.83}In_{0.17}As$. The shaded area is the spontaneous emission contribution ($\Lambda\lambda$) for a wavelength range ($\Delta\lambda$).*

2.7: The operational characteristics of SLDs

A SLD is an optical s/c device that operates with amplified spontaneous emission (ASE). Assuming for simplicity a constant injection carrier density in the active region, the change in photon density along the length of a SLD is given by the following rate-equations, [2-9]:

$$\frac{1}{\mathrm{v}}\frac{\partial P_\lambda}{\partial t} = -\frac{\partial P_\lambda}{\partial \mathrm{z}} + g_m(\lambda, N)P_\lambda + \frac{\delta(\lambda)\delta_f N}{\mathrm{v}\tau_{sp}} \qquad (2.12)$$

$$\frac{1}{\mathrm{v}}\frac{\partial Q_\lambda}{\partial t} = \frac{\partial Q_\lambda}{\partial \mathrm{z}} + g_m(\lambda, N)Q_\lambda + \frac{\delta(\lambda)\delta_r N}{\mathrm{v}\tau_{sp}} \qquad (2.13)$$

where P_λ is the forward travelling photon density; Q_λ is the reverse travelling photon density; $g_m(\lambda, N)$ is the (wavelength and carrier dependent) modal optical gain; $\delta(\lambda)$ is the fraction of spontaneous emission as a function of wavelength; v is the group velocity in the medium and τ_{sp} is the carrier dependent spontaneous recombination lifetime. The spontaneous recombination lifetime is written as, [2-10]:

$$\tau_{sp}(N) = \frac{1}{B_r N} \qquad (2.14)$$

where B_r is the bimolecular recombination coefficient.

The terms $g_m(\lambda,N)P_\lambda$ and $g_m(\lambda,N)Q_\lambda$ in equation (2.12) and (2.13) represent the ASE contribution. The spontaneous emission coupling to the forward and reverse travelling photon density is given by $\frac{\delta(\lambda)\delta_f N}{v\tau_{sp}}$ and $\frac{\delta(\lambda)\delta_r N}{v\tau_{sp}}$ respectively. A SLD will produce ASE only if the material optical gain is positive.

Associated with equations (2.12) and (2.13) is the carrier conservation rate equation to account for the injected carrier density:

$$\frac{\partial N}{\partial t} = \frac{1}{q}\frac{\partial J}{\partial d} - \int_0^\infty g_m(\lambda,N)(P_\lambda + Q_\lambda)d\lambda - B_r N^2 \qquad (2.15)$$

where J is the injection current density and q is the magnitude of electronic charge.

It can be seen from equation (2.15) that no non-radiative terms are included. Non-radiative recombination reduces the internal efficiency (η_i) of a device as follows, [2-7]

$$\eta_i = \frac{\int_0^\infty g_m(\lambda,N)(P_\lambda + Q_\lambda)d\lambda + B_r N^2}{\int_0^\infty g_m(\lambda,N)(P_\lambda + Q_\lambda)d\lambda + B_r N^2 + A_{nr}N + CN^3} \qquad (2.16)$$

where A_{nr} is parameter describing surface and defect non-radiative recombination mechanisms and C is the Auger recombination coefficient (~10^{-29} cm^6s^{-1}). The internal efficiency for GaInAs QW materials with an emission wavelength <1000nm is near unity, [2-11]. Therefore, non-radiative recombination can be neglected in the present model. However, to model materials with smaller bandgap energies the Auger recombination term CN^3 can be included in equation (2.15) to better represent the electron-hole recombination mechanisms.

2.8: Steady-state analysis for a S-SLD

Throughout this Section the following assumptions are made:

- The injection current density is constant across the contact region.
- No current spreading occurs within the device.
- The distribution of carriers under the contact is constant along all dimensions.
- Only the TE modal gain (g_m) is considered due to the suppression of the TM modal gain in strained QW materials, [2-12].

The geometry of the device to be modelled in this Section is a Fabry-Perot (FP) optical cavity of length L bound by parallel reflecting facets of reflectivity R_0 and R_L as indicated in the schematic of Figure 2.8. A small input signal intensity, P_{IN}, is given just inside the Fabry-Perot cavity at z = 0.

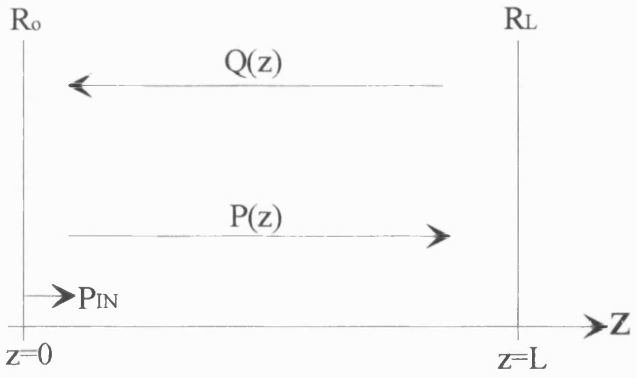

Figure 2.8: *Schematic diagram of an optical cavity bound by parallel facets with reflectivities* R_0 *and* R_L. *The direction in which the photon densities,* Q(z) *and* P(z), *travel is indicated.*

The boundary conditions associated with the FP cavity are as follows:

$$P(z=0) = P_{IN} + R_0 Q_0 \tag{2.17}$$

$$Q(z=L) = R_L P_L \tag{2.18}$$

where $P_L = P(z=L)$ and $Q_0 = Q(z=0)$.

The equations to be solved here are derived from equations (2.12), (2.13) and (2.14) by putting $\frac{\partial}{\partial t} = 0$, so that the steady state formulation becomes, [2-13]:

$$\frac{dP_\lambda}{dz} = g_m(\lambda, N)P_\lambda + \frac{\delta(\lambda)\delta_f N}{v\tau_{sp}} \tag{2.19}$$

$$\frac{dQ_\lambda}{dz} = -g_m(\lambda, N)Q_\lambda - \frac{\delta(\lambda)\delta_r N}{v\tau_{sp}} \tag{2.20}$$

$$\frac{J}{qd} = \int_0^\infty g_m(\lambda, N)(P_\lambda + Q_\lambda)d\lambda + B_r N^2 \tag{2.21}$$

The above set of equations is solved by using a numerical iteration scheme, Figure 2.9, in which N is kept constant at each iteration. Using this technique it is

possible to find an analytic solution to equations (2.17) - (2.19) at each iteration. The iteration procedure is terminated when a suitable value of N satisfies equation (2.21); such value best represents the given injection current density.

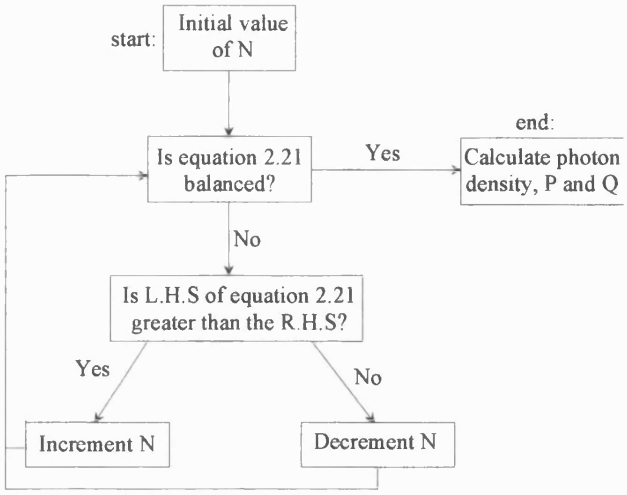

Figure 2.9: *Flowchart describing the numerical solution for the implementation of the carrier density,* N. *L.H.S. is the left-hand side and R.H.S. is the right-hand side.*

Assuming a constant value for the carrier density, $\overline{N} = const$, so that the gain is also constant, $\overline{g}_m = g_m(\lambda, \overline{N})$, the solutions to equations (2.19) and (2.20) for the forward and reverse travelling photon densities (derivation in Appendix C) are found to be

$$P_\lambda(z) = P_o e^{\overline{g}_m z} + (e^{\overline{g}_m z} - 1)P_{sp} \tag{2.22}$$

$$Q_\lambda(z) = Q_o e^{-\overline{g}_m z} + (e^{-\overline{g}_m z} - 1)Q_{sp} \tag{2.23}$$

where $P_0 = P(z=0)$.

In equations (2.22) and (2.23) P_{sp} and Q_{sp} are, respectively, the forward and reverse travelling spontaneous emission contributions:

$$P_{sp} = \frac{\delta(\lambda)\delta_f N}{\overline{g}_m \mathrm{v} \tau_{sp}} \tag{2.24}$$

$$Q_{sp} = \frac{\delta(\lambda)\delta_r N}{\overline{g}_m \mathrm{v} \tau_{sp}} \tag{2.25}$$

For S-SLDs, which have a uniform current injection contact width along z, the δ_f and δ_r fractions are equal, equation (2.7), and hence the values of P_{sp} and Q_{sp} are also equal. Section 2.8.3 presents an extension to the model where the device contact width varies longitudinally (e.g. tapered and parabolic contacts).

Expressions for P_0 and Q_0 in equations (2.22) and (2.23) can be obtained by substituting equations (2.22) and (2.23) into the boundary conditions. After some manipulation (Appendix D), it is found that the above expressions are

$$P_0 = \frac{P_{IN} + R_0 R_L e^{\bar{g}_m L}(e^{\bar{g}_m L} - 1)P_{sp} + R_0(e^{\bar{g}_m L} - 1)Q_{sp}}{1 - R_0 R_L e^{2\bar{g}_m L}} \tag{2.26}$$

$$Q_0 = R_L P_0 e^{2\bar{g}_m L} + R_L e^{\bar{g}_m L}(e^{\bar{g}_m L} - 1)P_{sp} + (e^{\bar{g}_m L} - 1)Q_{sp} \tag{2.27}$$

The total photon density just inside the FP cavity at z = L is, therefore,

$$P_L = \frac{P_{IN} e^{\bar{g}_m L}}{1 - R_0 R_L e^{2\bar{g}_m L}} + \frac{(e^{\bar{g}_m L} - 1)(R_0 e^{\bar{g}_m L} Q_{sp} + P_{sp})}{1 - R_0 R_L e^{2\bar{g}_m L}} \tag{2.28}$$

The first term in equation (2.28) contributes to the photon density only if there is an input signal intensity (P_{IN}). When modelling a SLD however, it is assumed that there is no optical pumping and hence P_{IN} = 0. The second term in equation (2.28) represents the ASE contribution. Equation (2.28) will be used to calculate the total output power from a SLD at different injection currents.

In the model the validity of equation (2.21) is verified by using the values of the forward and reverse travelling photon densities averaged along the length of the device (details in Appendix E), defined by:

$$P_{\lambda av}(\bar{N}) = \frac{1}{L}\int_0^L P_\lambda(z)dz \tag{2.29}$$

$$Q_{\lambda av}(\bar{N}) = \frac{1}{L}\int_0^L Q_\lambda(z)dz \tag{2.30}$$

Therefore, in the model formulation, equation (2.21) becomes:

$$\frac{J}{\mathrm{v}qd} = \sum_{\lambda} \bar{g}_m \left(P_{\lambda av}(\bar{N}) + Q_{\lambda av}(\bar{N})\right) + \frac{B_r \bar{N}^2}{\mathrm{v}} \qquad (2.31)$$

2.8.1: Simulating Light-Current characteristics and output spectrum of SLDs

To plot an LI curve or spectral characteristic for a SLD it is necessary to calculate the power emitted from the output facet for a range of injection currents. The power output is given by the energy flow rate through the output facet. Therefore,

Optical Power = Photon flux × Photon Energy

Photon flux = $(1 - R_L)\mathrm{v}P_L Wd$

Photon Energy = $\frac{hc}{\lambda}$

$$\therefore \quad Power = \frac{1}{\lambda}(1 - R_L)\mathrm{v}P_L Wdhc \text{ (Watts)} \qquad (2.32)$$

where W is the width of facet defined by the active layer; d is the active layer thickness.

The flowchart in Figure 2.10 shows the steps required to simulate the LI and spectral characteristic of a SLD.

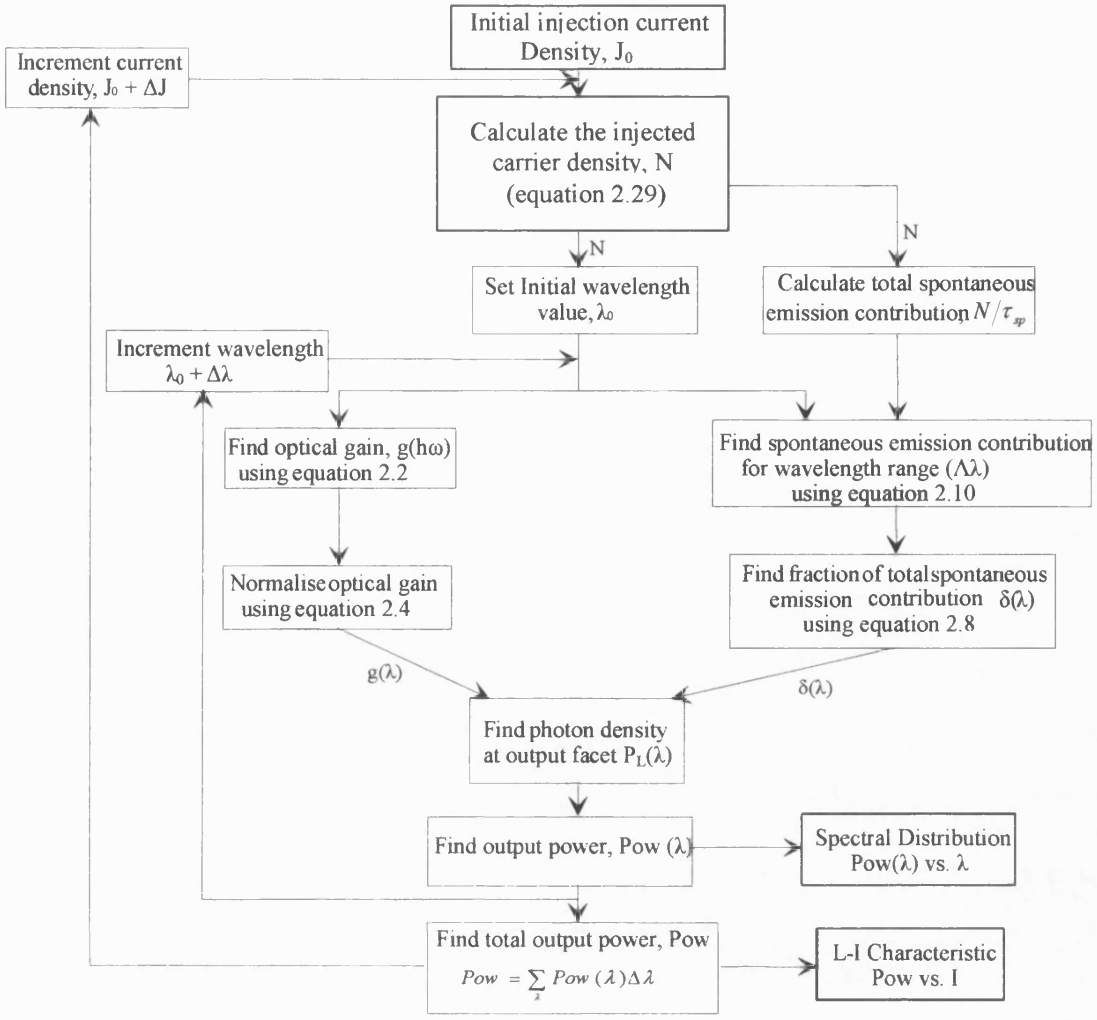

Figure 2.10: *Flowchart representing the model to calculate LI and spectral characteristics of a SLD.*

2.8.2: Longitudinal distribution of the carrier density

In the previous sections the carrier density is assumed to be constant to simplify the computational scheme. However, substituting the z-dependent photon density solutions, $P(z)$ and $Q(z)$, equations (2.22) and (2.23) respectively, into equation (2.21) the z-dependent carrier density profile is obtained. The process becomes straightforward only if the (modal) gain is kept constant to the value computed in the last iteration, $\overline{g}_m = g_m\left(\overline{N}\right)$. Hence, the equation defining the carrier density as a function of z, $N(z)$, is the following:

$$\frac{J}{qd} = \bar{g}_m\left[P_\lambda(z)+Q_\lambda(z)\right]+B_r\overline{N}^2 \tag{2.33}$$

Carrier density profiles computed by the model are presented in Figure 2.11 to show that at higher injection currents (significantly above transparency) the reflected signal, $Q(z)$, depletes the carrier at the rear of the device, which causes optical gain saturation [2-14].

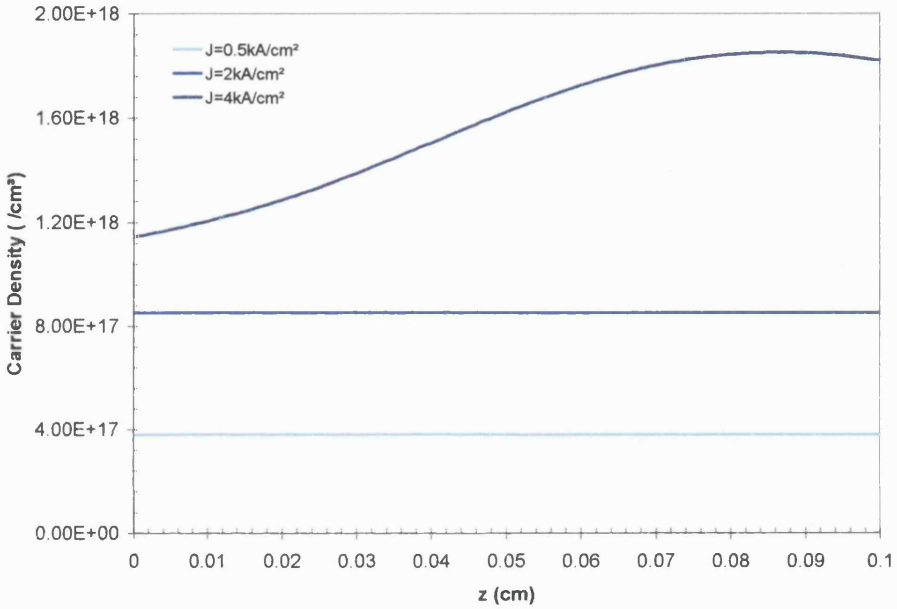

Figure 2.11: *Carrier density distributions as a function of z in a S-SLD for various current densities.*

2.9: Modelling SLDs with longitudinally non-uniform geometry

To apply the ray model presented in Section 2.8 to a SLD with longitudinally non-uniform geometry, e.g., tapered or parabolic contact SLDs (T-SLDs and P-SLDs), the gain region is divided into lateral sections of constant width, Figure 2.12. However, three other important changes also need to be made:

- The fraction of spontaneous emission coupling to the forward and reverse travelling photon densities (δ_f and δ_r) is to be calculated for each lateral section.
- The current density in each lateral section is assumed to be constant and equal to the injection current density for all lateral sections.

- The photon flux expression described in Section 2.8.1 is to exclude rays incident to the output facet with angle greater than the critical angle for total internal reflection, θ_C, (applies to sections with small length).

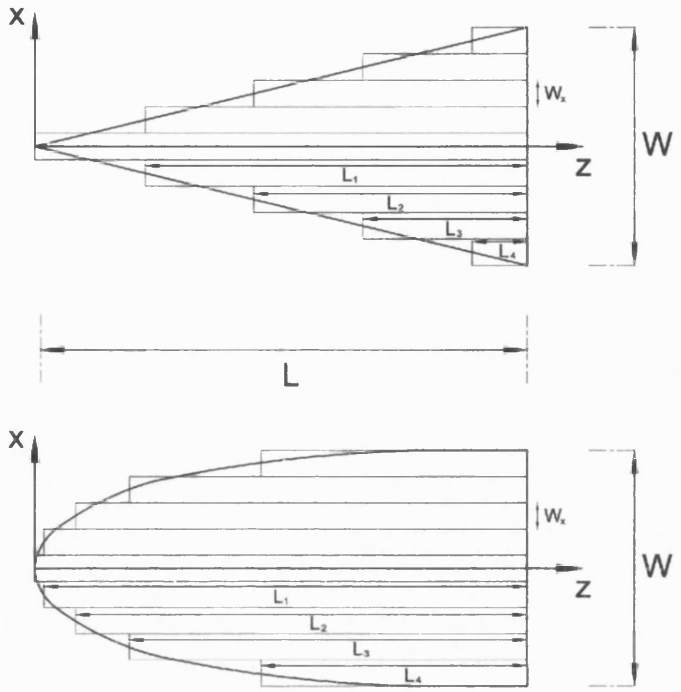

Figure 2.12: *Schematic showing the gain region of T-SLDs and P-SLDs divided into lateral sections of various lengths.*

In T-SLDs and P-SLDs the fraction of reverse travelling spontaneous emission coupling into the active region (Q_{sp}) is smaller than the fraction of forward travelling spontaneous emission (P_{sp}), therefore T-SLDs and P-SLDs are more efficient than S-SLDs since the optical gain saturation due to optical feedback is reduced as mentioned in Section 1.2. To calculate P_{sp} and Q_{sp} in each section of T-SLDs and P-SLDs equation 2.6 are is modified to account for the different lengths, L_X, of the lateral sections:

$$\delta_{fx} = \frac{1}{\pi}\tan^{-1}\left(\frac{W}{L_x}\right)\cos^{-1}\left(\frac{n_2}{n_1}\right) \tag{2.34}$$

$$\delta_{rx} = \frac{1}{\pi}\tan^{-1}\left(\frac{W_x}{L_x}\right)\cos^{-1}\left(\frac{n_2}{n_1}\right) \tag{2.35}$$

where W_x and L_X are the width and the length of each section respectively, Figure 2.12.

It can be seen from equations (2.34) and (2.35) that $\delta_{rx} < \delta_{fx}$ since the width of the overall geometry (W) is greater than the width of each lateral section (W_x). The total amount of optical feedback is also dependent on the number of lateral sections. The larger the number of lateral sections the smaller is W_x and hence δ_{rx}.

The current density of each lateral section (J_x) is assumed to be equal to the current density of the entire contact region (J) so that the optical gain is constant over the entire geometry. Hence,

$$J_x = J = \frac{I}{A} \tag{2.36}$$

where A is the area of the entire contact region and I is the injection current.

The photon flux leaving the output facet of the device depends on the critical angle for total internal reflection θ_c. Rays incident to the output facet with angles (with respect to the facet normal) greater than θ_c are not included in the expression for photon flux since they are reflected back into the gain region, Figure 2.13. The expression for photon flux becomes:

$$\text{Photon flux} = (1 - R_L)\text{v}P_L W_c d \tag{2.37}$$

where

$$W_c = 2L_x \tan\theta_c \tag{2.38}$$

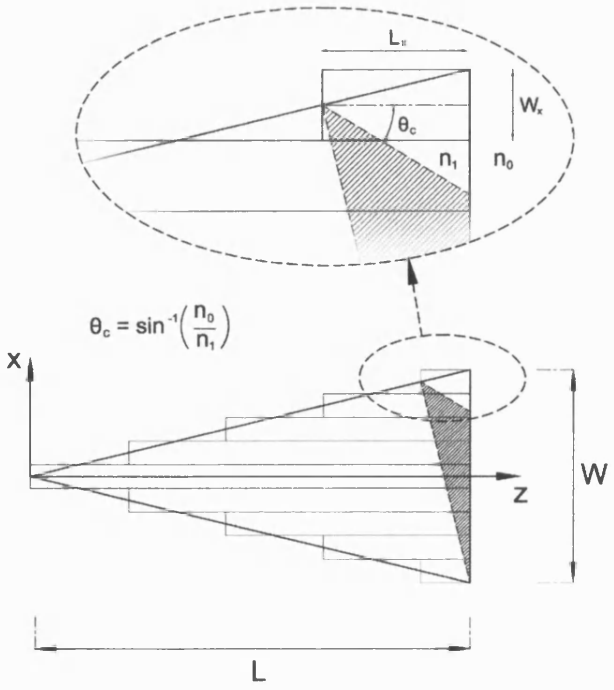

Figure 2.13: *Schematic showing the rays (hatched region) incident to the output facet that are totally internally reflected.*

Finally, the total power emitted from a device modelled in this fashion is calculated by summing the power from each lateral section. Also in the case of T-SLDs and P-SLDs the procedure shown in Figure 2.10 is used to find the output power from each section.

2.10: Summary

In this chapter the high-power (LOC) material structure used to fabricate the SLDs discussed in this thesis has been described together with a detailed analysis of the vertical mode profiles supported by the given epitaxy. The basic SLD device characteristics and principle of operation are also presented. Importantly, the role of the v-groove etched deflector in reducing the effective rear facet reflectivity has been high lighted.

A model based on the ray analysis was introduced. A method of using the model to calculate the photon density distribution, the output power and the spectral characteristic of a SLD was described. A modified model to account for longitudinally non-uniform SLD geometries has been discussed to calculate the LI characteristic of tapered or parabolic SLDs.

References

[2-1] Tulios P. P., and Knox R.M., *Image line integrated circuits for applications at millimetre wavelengths*, U.S. Army Electronics Command, Final Report, Rept. No. ECOM-73-0217-F, 1974.

[2-2] Yonezu H., Sakuma I., Kobayashi K., Kamejima T., Ueno M., and Nannichi Y., *A GaAs-Al_xGa_{1-x} Double Heterostructure Planar Stripe Laser*, Jap. J. of App. Phy., Vol. 12, No. 10, 1973, pp. 1585-1592.

[2-3] Middlemast I., *A Comprehensive Model of the Superluminescent Diode*, University of Bath, 1986, chapter 3.

[2-4] Burrus C.A., and Dawson R.W., *Small-Area High-Current-Density GaAs Electroluminescent Diodes and a Method of Operation for Improved Degredation Characteristics*, Applied Physics Letters, Vol. 17, No. 3, August 1970, pp. 97-99.

[2-5] Singh J., *Semiconductor Devices: An Introduction*, McGraw-Hill Inc.,1994, ISBN 0-07-113906-0.

[2-6] Xu L.M., Tan G.L., Xu J.M., Irikawa M., Shimizu H., Fukushima T., Hirayama Y., and Mand R.S., *Ultra-High Differential Gain in GaInAs-AlGaInAs Quantum Wells: Experimental and Modelling*, IEEE Photonics Technology Letters, Vol. 7, No. 9, September 1995, pp. 947-949.

[2-7] Agrawal G.P., and Dutta N.K., *Semiconductor Lasers*, Van Nostrand Reinhold, 1993, ISBN 0-442-01102-4.

[2-8] Wilson J., and Hawkes J.F.B., *Optoelectronics: An introduction*, Prentice-Hall International,1983, ISBN 0-13-6383955.

[2-9] Carroll J.E., *Rate equations in semiconductor electronics*, Cambridge University Press, Cambridge, 1985.

[2-10] Kressel H., and Butler J.K., *Semiconductor Lasers and Heterojunction LEDs*, Academic Press, London, 1977, Chapter 1.

[2-11] Catchpole K.R., *High external quantum efficiency of planar semiconductor structures*, Semiconductor Sci. and Tech., Vol. 19, 2004, pp. 1232-1235.

[2-12] ed. Zory P.S., *Quantum Well Lasers*, Academic Press, New York, 1993.

[2-13] Zhuraleva O.V., Kurnosov V.D., Kurnosov K.V., Lobintsov A.V., Romantsevich V.I., Simakov V.A., and Chernov R.V., *Study of the Spectral and Power Characteristics of Superluminescent Diodes*, Quantum Electronics, Vol.34., No. 1, 2004, pp. 15-19.

[2-14] Yunus S., *Development and Study of High Power Tapered Geometry Superluminescent Diodes*, PhD Thesis, University of Bath, 2002, Chapter3.

Chapter 3
Ray Model to Compute Near and Far Field Intensity Profiles

3.1: Introduction

In this Chapter a modified version of the ray model presented in Chapter 2 is used to simulate the Near Field (NF) and Far Field (FF) intensity profiles of SLDs. The difference between the model described here and that of Chapter 2 is that the optical rays in the SLD are now considered at all angles with respect to the output facet of the device. To simplify the computational method only the forward travelling photon density is considered. Equation (2.17) is solved here to compute the contribution of any ray to the output power as a function of the endpoint of the ray on the facet and the ray direction to compute the near and far field intensity profiles.

The wavelength-dependence is neglected in the ray model presented in this Chapter. However, differently from the model to compute the LI characteristic described in Chapter 2, the carrier density in the present model does vary across the device to account for current spreading and carrier diffusion, as discussed in Section 3.2. Optical saturation is also included in the model. SLDs with a longitudinally non-uniform geometry (T-SLDs and P-SLDs) are represented by using x and z dependent carrier density distributions also discussed in Section 3.2. The details of the model for computing the near and far field intensity profiles are described in Section 3.3.

3.2: Flexible (analytic) representation of the carrier density distribution

A non-uniform carrier density distribution dependent on the lateral (x) and longitudinal (z) variables is used in the ray model to account for current spreading, carrier diffusion and, importantly, longitudinally non-uniform geometry. The carrier density distribution is represented by a Super Gaussian function (SG) that is both x and z dependent, [3-1],

$$N(x,z) = N_{\max}(z)e^{-\left(\frac{2x}{2W(z)}\right)^{q(z)}} \qquad (3.1)$$

where at each longitudinal position z, $N_{max}(z)$ is the maximum current density; $W(z)$ is half the width of the active region; $q(z)$ is an integer defining current spreading and carrier diffusion.

The width of the SG function, $W(z)$, is varied to model any geometry SLD. The following expressions for the z-dependent contact width are used to model S-SLDs, T-SLDs and P-SLDs, respectively:

$$W(z) = W_F \tag{3.2}$$

$$W(z) = \frac{zW_F}{L} \tag{3.3}$$

$$W(z) = \sqrt{\frac{W_F{}^2 z}{L}} \tag{3.4}$$

where W_F is the width of the contact at the output facet ($z=L$); L is the length of the contact region. Figure 3.1 shows the normalised lateral carrier distributions for S-SLD, T-SLD and P-SLD at discrete points along the device length.

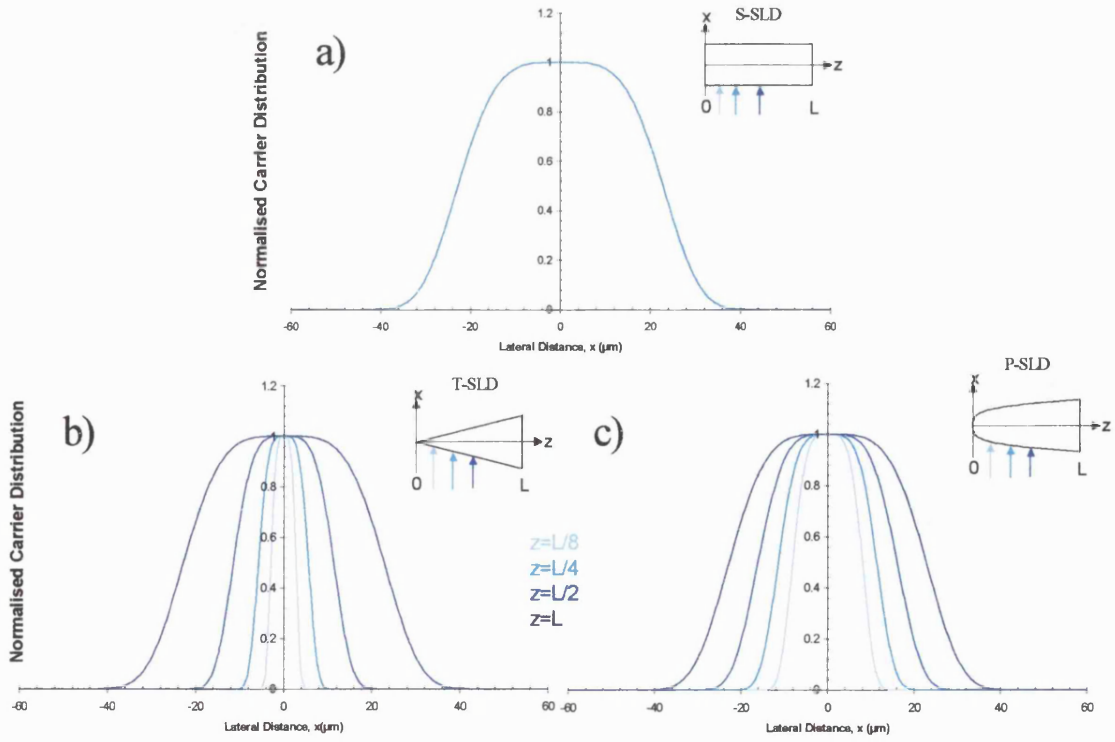

Figure 3.1: *Graphs showing the change in lateral carrier profile at distances along z (z=L/8, L/4, L/2, L) for (a) S-SLD, (b) T-SLD and (c) P-SLD.*

The function $q(z)$ is chosen to best represent current spreading and carrier diffusion for different geometries and levels of current injection. In T-SLDs and P-SLDs the carrier density profile varies from Gaussian-like where the rib width is small to almost rectangular where the rib width is large compared to the carrier diffusion length, Figure 3.2.

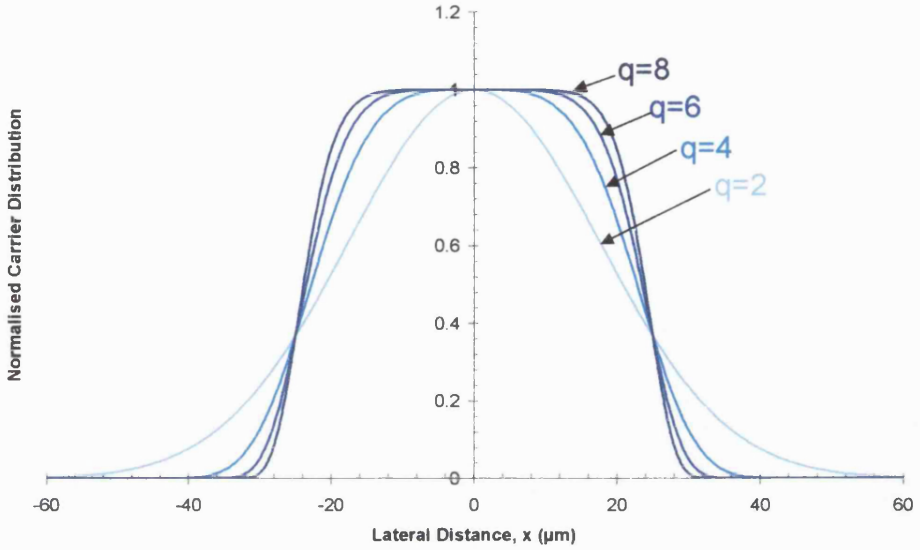

Figure 3.2: *Normalised carrier distributions for different values of q. Low values (q=2) best represent small contact width and low injection currents. High values (q>6) are used to best represent large contact widths and injection currents above material transparency (g_m>0).*

Optical gain saturation in SLDs is incorporated into the model by assuming a z-dependent peak value for the carrier density profile, $N_{max}(z)$, in equation (3.1). The profile is similar to the carrier density profile presented in Chapter 2, Figure 2.11.

3.3: Model formulation

In the ray model the forward travelling photon density rate equation (2.17) is solved to calculate the total photon density at the output facet of a SLD, [3-2]. Rays originating at any point inside the active region contribute to the total photon density at the output facet. In Chapter 2 the injected carrier distribution is assumed to be constant along all dimensions of the SLD. However, equation (2.17) can be re-written using a polar co-ordinate system as follows

$$\frac{dP(s,\theta)}{ds} = g_m(s,\theta)P(s,\theta) + \delta_f \frac{N(s,\theta)}{\tau_{sp} \mathrm{V}} \tag{3.5}$$

where s is the length and θ is the angle of each ray with respect to the output facet, Figure 3.3, $g_m(s,\theta)$ is the modal gain and δ_f is the spontaneous emission contribution.

The NF intensity profile is determined calculating

$$I(x) = \int_{\theta_{\min}}^{\theta_{\max}} P(s,\theta)d\theta \tag{3.6}$$

where θ_{min} and θ_{max} are the critical angles for total internal reflection given by

$$\theta_{\min} = \sin^{-1}\left(\frac{n_0}{n_1}\right) \tag{3.7}$$

$$\theta_{\max} = \pi - \theta_{\min} \tag{3.8}$$

where n_0 and n_1 are the refractive indices of air and the active layer respectively.

The spontaneous emission contribution, δ_f, in equation 3.5, is determined by the distance between the discretisation points, Figure 3.4. In the present model the spontaneous emission contribution is given by

$$\delta_f = \frac{1}{2\pi}\frac{\Delta x}{s}\cos^{-1}\left(\frac{n_2}{n_1}\right) \tag{3.9}$$

where Δx is the distance between the discretisation points on the x-axis.

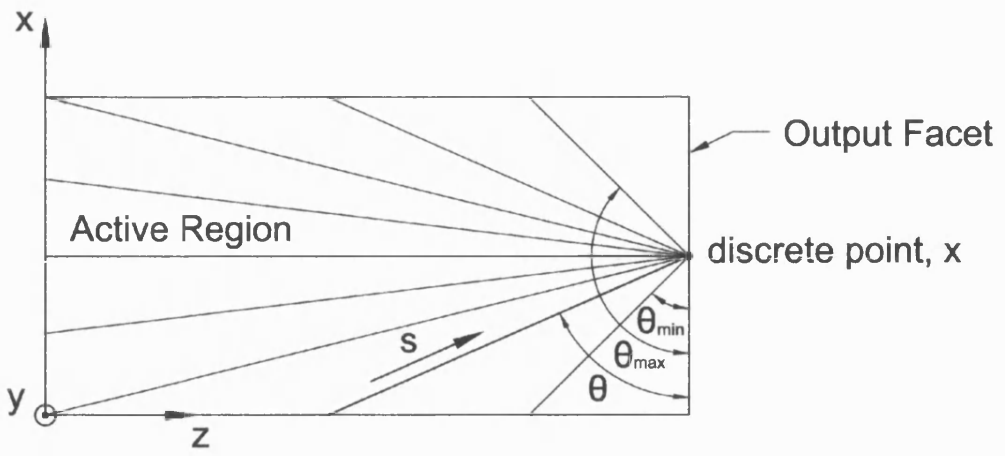

Figure 3.3: *Schematic representation of rays at different angles θ ($\theta_{min}<\theta<\theta_{max}$) with the same endpoint x on the output facet.*

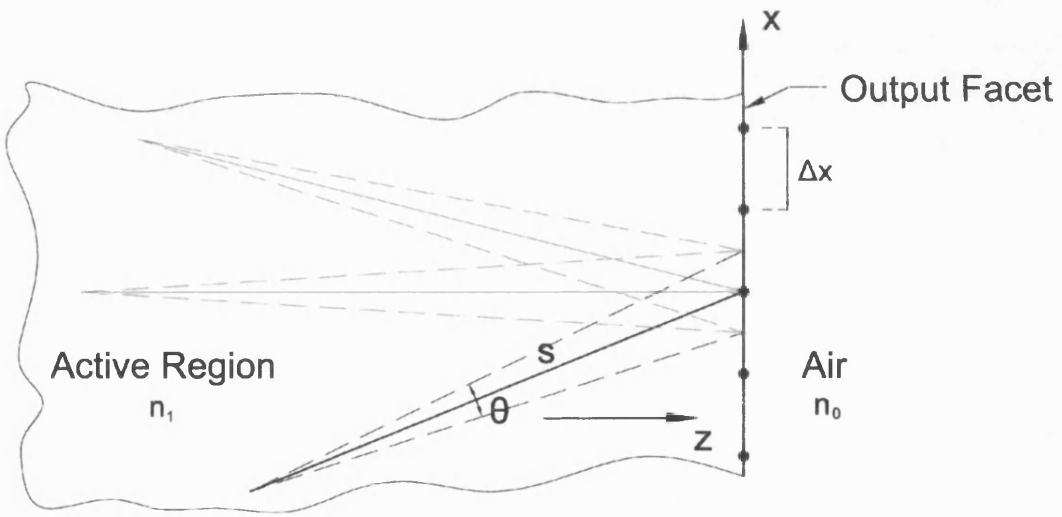

Figure 3.4: *Schematic showing various rays incident on the output facet of a SLD. The spontaneous emission contribution, δ_f, is dependent on the length of each ray, s, and the distance between discretisation points, Δx.*

The FF pattern is the angular distribution of field intensity emitted from the output facet, $I(\theta')$, calculated by

$$I(\theta') = \int_{-\infty}^{\infty} P(s,\theta)dx \tag{3.10}$$

The relationship between θ' and θ is given by

$$\theta' = \cos^{-1}\left(\frac{n_1}{n_0}\cos\theta\right) \tag{3.11}$$

where n_1 and n_0 are the refractive indices of the active region and air respectively, Figure 3.5.

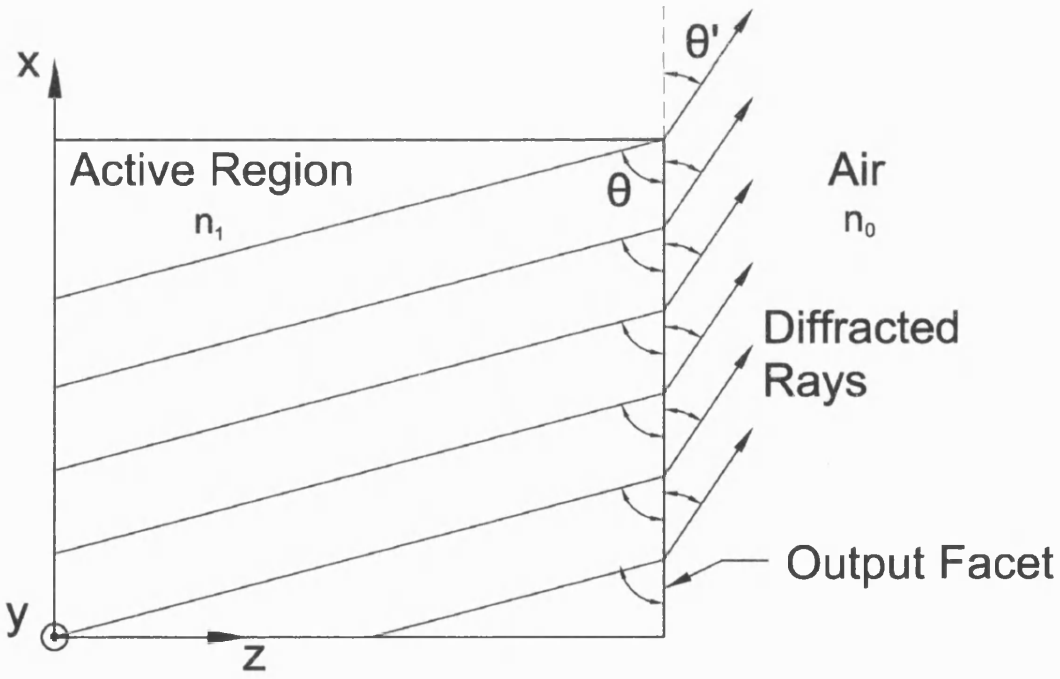

Figure 3.5: *Schematic showing rays with the same angle θ with respect to the output facet diffracting at the s/c air interface.*

3.4: Summary

A ray model that includes the lateral and longitudinal non-uniformity of the carrier density distribution in the active layer of the SLD has been presented. With this model the contribution to the total output power from rays originating at any point inside the active layer can be calculated. Importantly, with the ray model presented in this chapter the NF intensity profile and the FF pattern can be computed for SLDs with any injection contact geometry.

References

[3-1] Causa F., Sarma J., and Yunus S., *Characterization of angled tapered superluminescent LEDs*, Applied Optics, Vol.41, No.24, August 2002, pp.5045-5050.

[3-2] Causa F., and Sarma J., *A Realistic Model for the Output Beam Profile of Stripe and Tapered Superluminescent Light-emitting Diodes*, Applied Optics, Vol. 42, No. 21, July 2003, pp. 4341-4348.

Chapter 4
Characterisation of Stripe and Tapered SLDs

4.1: Introduction

This Chapter presents the theoretical and experimental characterisation of in-house fabricated S-SLDs and T-SLDs. An investigation into the effects of optical saturation to improve the efficiency of SLDs is also presented. The repeatability of the results discussed in this thesis has been proved by testing over two hundred SLDs and observing very similar trends to those presented in this Chapter.

The experimental results including the LI characteristics, spectral distributions, Degree of Polarisation (DOP), coherence curves, FF patterns and NF intensity profiles of S-SLDs and T-SLDs are presented in Section 4.2. The experimental and theoretical results for the P-SLD geometry are also included to further validate the ray models discussed in Chapters 2 and 3. The measurement techniques used to characterise the SLDs are described in Appendix F.

Results from the ray models are used to investigate optical gain saturation in SLDs and, therefore, interpret the experimental results. In addition, the ray models have been used also to investigate the best possible combination of device parameters (length, AR coating) to optimise the Wall-Plug (W-P) efficiency. Devices with partially etched ribs to provide a weak lateral effective refractive index step have also been fabricated to investigate the effect of index-guiding on the fraction of spontaneous emission coupled to the forward travelling photon density and, therefore on the output power and efficiency.

4.2: Characterisation of S-SLDs, T-SLDs and P-SLDs

The devices presented in this Chapter are fabricated from material QT1614 (unless otherwise stated), Section 2.1. They are all mounted p-side up onto copper heat sinks using silver loaded epoxy resin. The p-side is contacted with gold wire using a thermo-compression ultrasonic bonder. The measurements were taken from devices operating under pulsed conditions (5μs, 200Hz).

The injection contact geometry of the S-SLD, T-SLD and P-SLD is given in Figure 4.1; the device dimensions are summarised in Table 4.1.

Table 4.1: *Details of the dimensions of the S-SLDs, T-SLDs and P-SLDs fabricated in-house.*

Device name	W (μm)	L (μm)	Rib Etch Depth (μm)	D (μm)
S-SLD(25)	25	1000	0.6	200
S-SLD(50)	50	1000	0.6	200
S-SLD(100)	100	1000	0.6	200
T-SLD(50)	50	1000	0.6	200
T-SLD(100)	100	1000	0.6	200
T-SLD(200)	200	1000	0.6	200
P-SLD(100)	100	1000	0.6	200
P-SLD(50)	50	1000	0.6	200

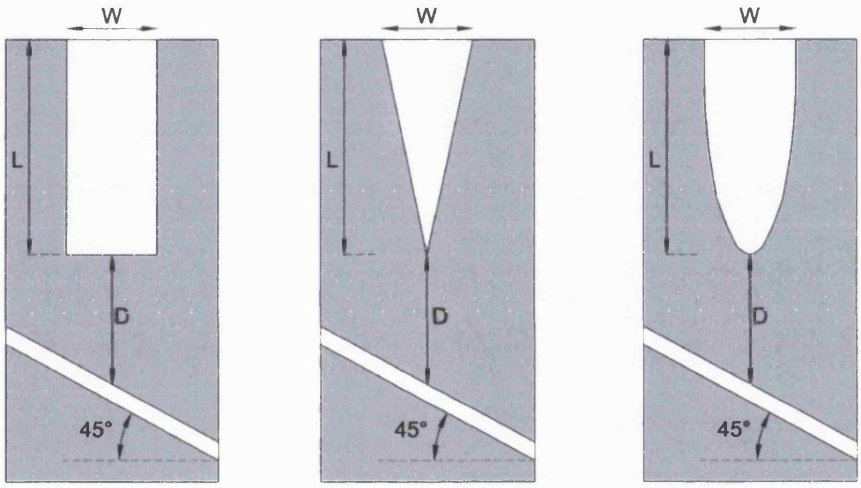

Figure 4.1: *Top view schematic of the S-SLD, T-SLD and P-SLD geometry.*

4.2.1: LI characteristic and W-P Efficiency

The LI characteristics of S-SLDs and T-SLDs are presented in Figure 4.2. Typical SLD LI curves have been observed from all devices: linear in the spontaneous emission regime (non positive optical gain), becoming super-linear at the on-set of superluminescence (ASE regime, positive optical gain) and then sublinear when gain saturation occurs. The theoretical LI curves computed using the model described in Chapter 2 are also plotted for comparison. The agreement between theory and experiment is good, indicating that the model satisfactorily represents the device operation. The input parameters that have been used in the model to simulate the SLD operational characteristics are summarised in Table 4.2.

Table 4.2: *Material and device parameters used in the ray model simulation.*

Material Constants	Value
B_r	1.0×10^{-10} (cm^3s^{-1})
A_0	1.5×10^{-16} (cm^2)
N_{tr}	1.45×10^{18} (cm^{-3})
α_s	-8 (cm^{-1})
α_f	-4 (cm^{-1})
R_0	0.0
Γ	0.12*

*The Γ per QW is calculated to be 0.04

The voltage-current (VI) characteristic and W-P efficiency of S-SLDs and T-SLDs are plotted in Figures 4.3 and 4.4 respectively. From the gradient of the VI curve the series resistance, R_S, of the device is extracted, [4-1]. The junction voltage, V_J, is calculated using

$$V_J = \frac{E_g}{q} \tag{4.1}$$

where E_g is the bandgap energy and q is the magnitude of electronic charge. The value of R_S is calculated to be 0.52Ω for both T-SLDs and S-SLDs and V_J = 1.21V comparing to 1.22V measured from the VI curve.

The efficiency of each device is described by the W-P efficiency that is given by

$$\text{W-P efficiency} = \frac{P_{OUT}}{IV} \times 100 \tag{4.2}$$

where P_{OUT} is the output power of the SLD, I is the injection current, and V is the voltage across the SLD.

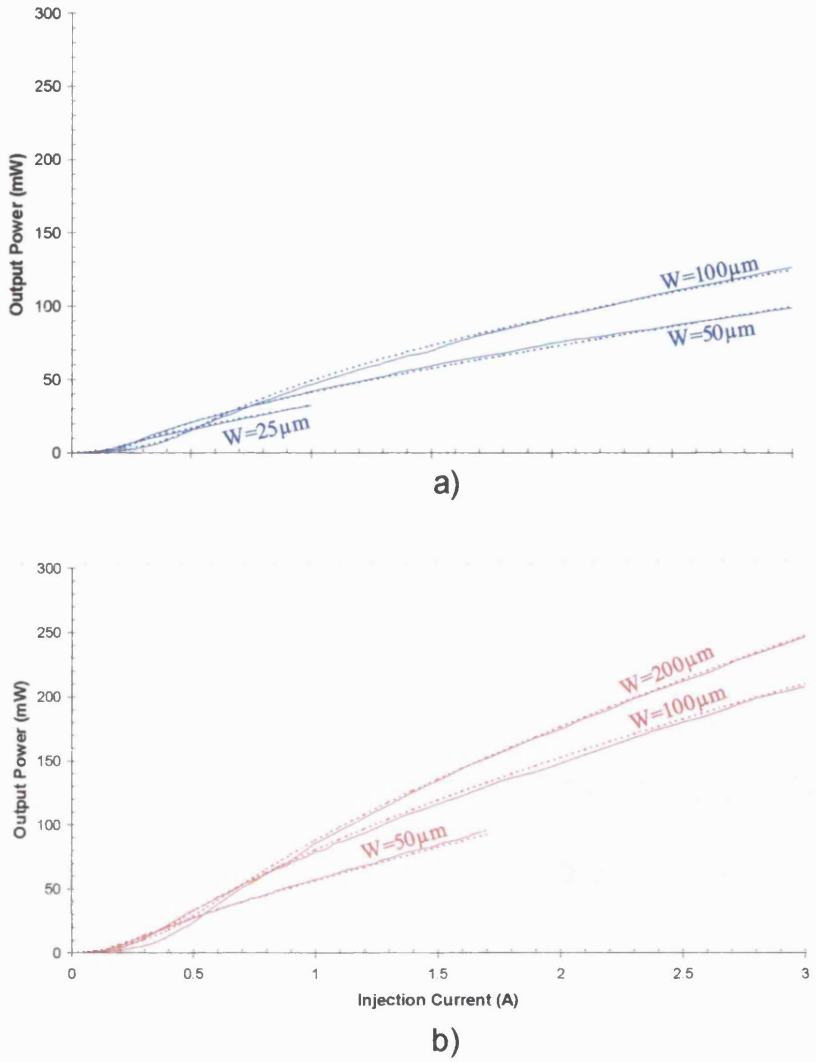

Figure 4.2: *Theoretical (dashed) and measured (solid) LI characteristics for (a) S-SLDs (blue) and (b) T-SLDs (red).*

The broad area devices, S-SLD(100) and T-SLD(200), in Figure 4.4 are more efficient than smaller area devices, S-SLD(25) and T-SLD(50) for I>500mA. The broad area devices have high saturation power because of the power density, which causes optical gain saturation, [4-2].

T-SLDs are typically more efficient than S-SLDs because the gain saturation due to optical feedback is reduced with a tapered geometry injection metal contact, [4-2], [4-3]. In tapered devices most of the optical feedback is dissipated in the lossy region around the gain region under the metal contact. This effect is noticeable when comparing the output optical power measured from S-SLDs and T-SLDs of either the same active volume, e.g. S-SLD(100) and T-SLD(200), or same width and length, e.g. S-SLD(100) and T-SLD(100). In both cases the optical output power and, hence, the W-P efficiency measured from T-SLDs is higher than that measured from S-SLDs. The

decrease in W-P efficiency after the peak value noticed for all devices is caused by optical gain saturation.

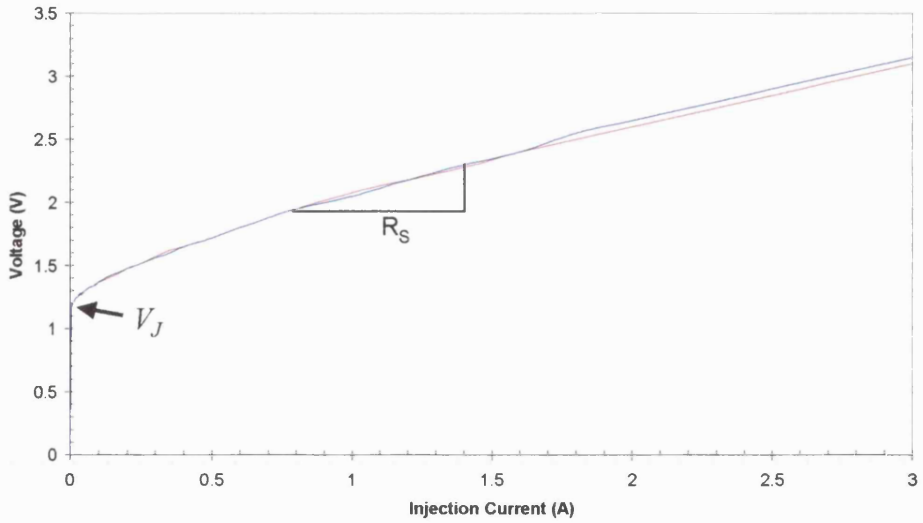

Figure 4.3: *Experimental VI characteristic measured from S-SLDs (blue) and T-SLDs (red).*

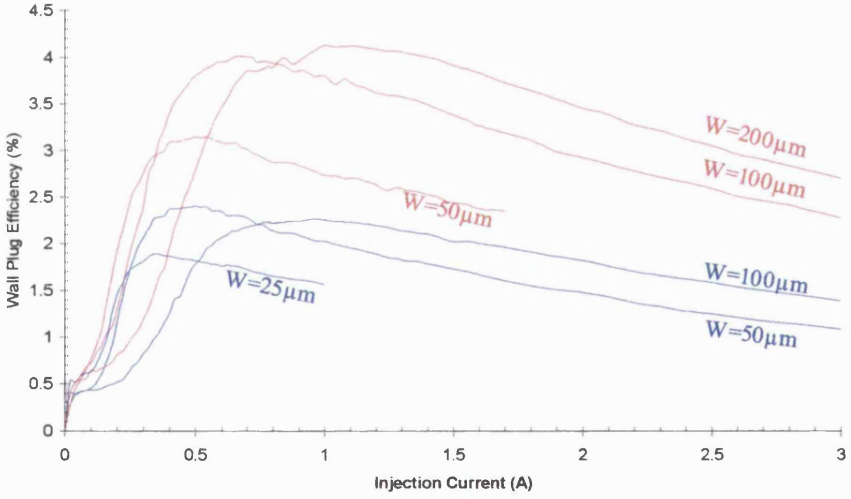

Figure 4.4: *Experimental W-P efficiency of S-SLDs (blue) and T-SLDs (red) with different widths (W).*

To visualise the effect of optical feedback on the gain in the device, the model described in Chapter 2 been used to compute the carrier density profile along the length of S-SLD(100) at various injection currents, Figure 4.5. At high injection currents (I>1A) the reflected signal from the output facet (optical feedback) depletes the carriers at the rear of the device (z=0) so that the optical gain in that region is significantly reduced.

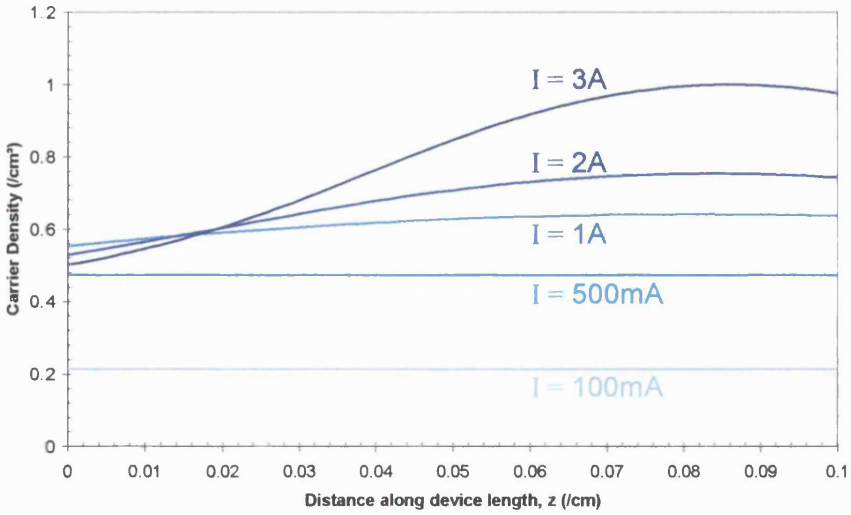

Figure 4.5: *Carrier distribution along z in S-SLD(100) computed for various injection currents.*

The experimental and theoretical LI characteristics of P-SLDs are plotted in Figure 4.6. The theoretical results are in good agreement with the experimental results and indicate the versatility of the model to simulate SLDs of various geometry.

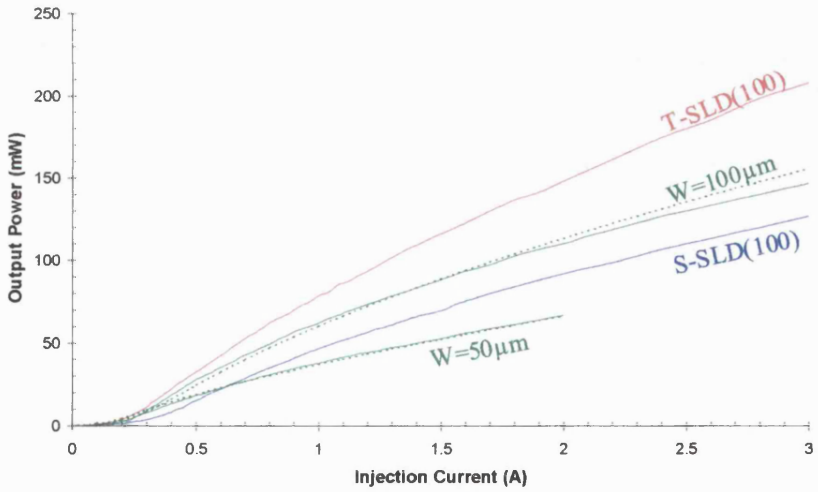

Figure 4.6: *Theoretical (dashed) and experimental (solid) LI characteristics obtained for P-SLDs (green) of different widths. S-SLD(100) and T-SLD(100) are included for comparison.*

The theoretical and experimental results measured from T-SLD(200) for a high-power, triple QW LOC DH material designated QT1137 is presented in Figure 4.7 to verify that the model can be used to calculate the characteristics of SLDs fabricated from different materials. Results obtained from material QT1614 are included for comparison. The structure, optical properties and material constants used by the model to compute the LI characteristic from SLDs fabricated from material QT1137 are in

Appendix G(i). The agreement between theory and experiment is good. The output power of QT1137 is 9% larger than QT1614 for all injection currents, which relates to a peak W-P efficiency increase of 0.4%.

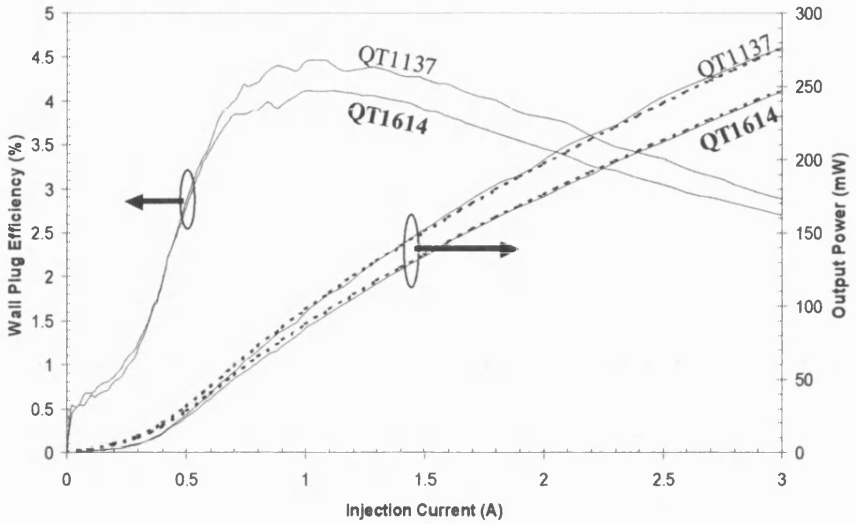

Figure 4.7: *Theoretical (dashed) and experimental (solid) LI characteristic and W-P efficiency of T-SLD(200) fabricated from QT1137 and QT1614.*

4.2.2: Spectral characteristics

Normalised spectral curves measured from S-SLD(50) using an Optical Spectrum Analyser (OSA) with 0.1nm resolution at various injection currents are presented in Figure 4.8. The Full Width at Half Maximum (FWHM) spectral width and peak wavelength (λ_{PEAK}) values for each injection current is presented in Figure 4.9. For increasing injection current the FWHM spectral width broadens slightly and λ_{PEAK} shifts to longer wavelengths. The red shift of the peak wavelength is attributed to a combination of gain saturation, [4-4], and heating effects in the active layer, [4-5]. The larger FWHM results from an increase in quasi-Fermi level separation and subsequent gain curve broadening at high carrier densities. Corresponding spectra obtained with the ray model are plotted in the inset of Figure 4.8 showing similar trends in λ_{PEAK} to the experimental results. To match the theoretical shift in λ_{PEAK} to the shift obtained experimentally the temperature variable (T) in equations 2.3 (a) and (b) is increased by ~0.05 nmK^{-1}. The theoretical and experimental spectra at I=500mA are similar but at I>500mA the gain curves computed using equation 2.2 do not fully represent the broadening effect due to saturation.

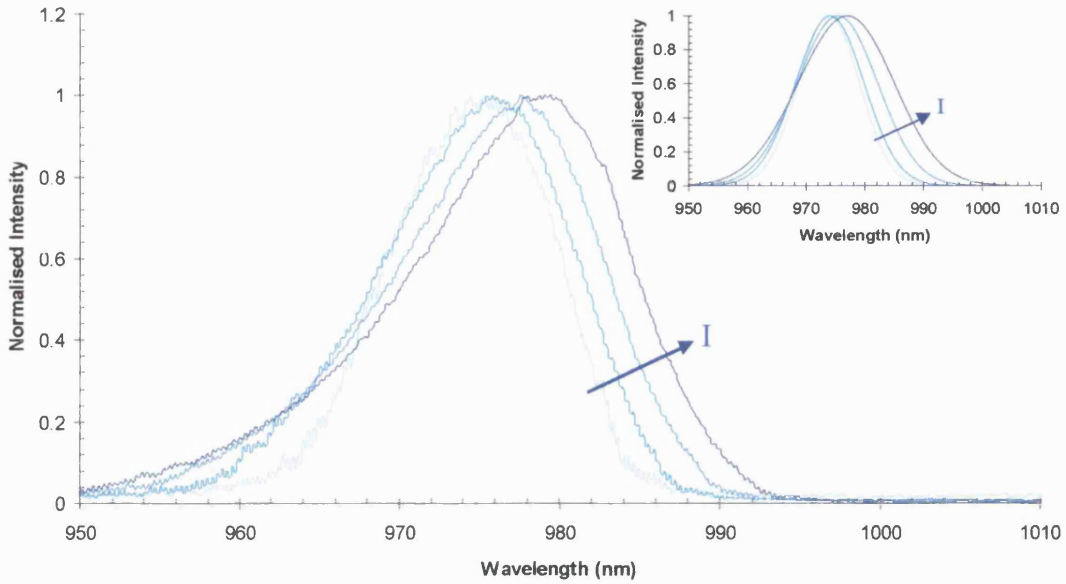

Figure 4.8: *Spectra measured from S-SLD(50)s for various injection currents. Corresponding theoretical results are shown in the inset.*

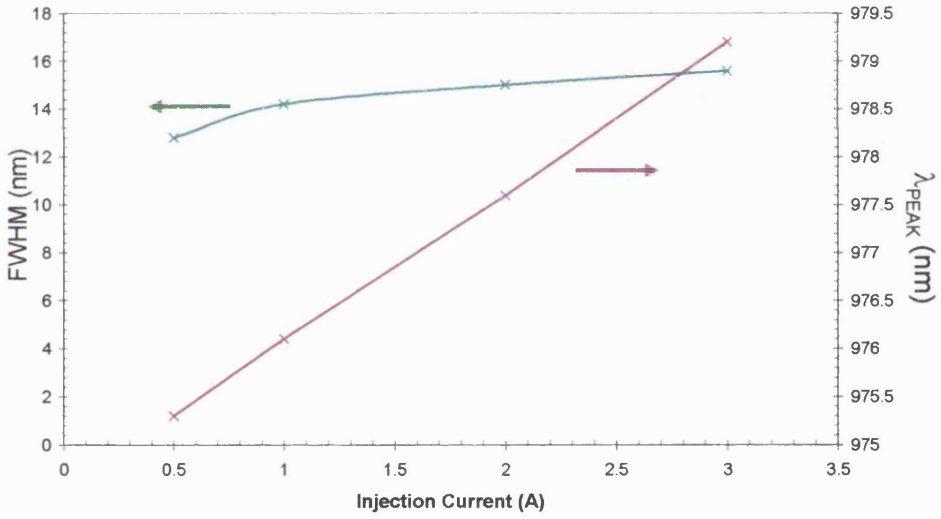

Figure 4.9: *Spectral FWHM and λ_{PEAK} for various injection currents.*

The normalised spectral distribution and corresponding coherence curves obtained from S-SLDs(50) and T-SLDs(100) at I=1A are compared in Figures 4.10 and 4.11 respectively. The coherence curves are calculated by taking the Fourier Transform of the measured spectral distributions. The Fourier conjugate ($2\pi/\lambda$) is used to express the coherence curves in terms of optical path length. The measured spectra

are almost indistinguishable with FWHM and λ_{PEAK} identical. The coherence length, calculated using the following expression, [4-6],

$$L_C = 0.66 \frac{\lambda_{PEAK}^2}{FWHM} \tag{4.3}$$

where the prefactor (0.66) is used for a Gaussian profile, is 45.1μm. Typically the spectral distribution measured from the in-house fabricated devices does not present a clear modulation, but a slight intensity fluctuation of 0.1dB, comparing well with other published results, [4-7], [4-8]. The spectral modulation is presented in the inset of Figure 4.10 (OSA resolution: 0.01nm). The mode spacing estimated from the intensity ripple at the peak of the measured spectrum is approximately 0.1nm, in agreement with the theoretical estimate of 0.119nm obtained considering 1200μm device length (including the injection metal contact length and the spacing between the rear of the contact and the rear deflector) and the theoretical modal effective refractive index $n_{eff,m}$=3.3205. The coherency curves show that there are no significant residual coherence peaks for either geometry suggesting that the etched deflector is very effective at suppressing optical feedback (Fabry-Perot modulation suppression).

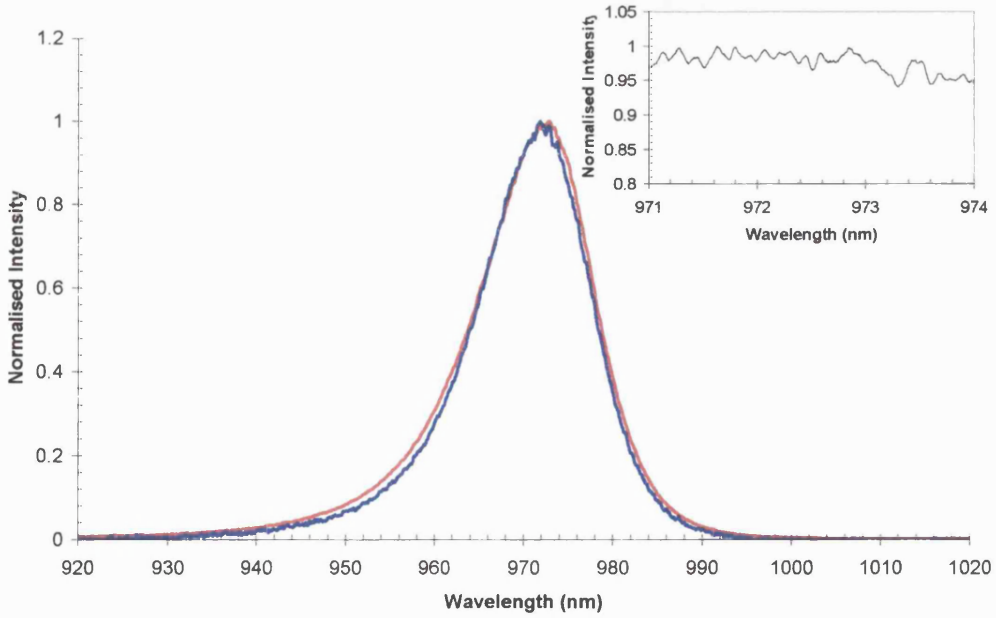

Figure 4.10: *Spectra measured from S-SLDs(50) (blue) and T-SLDs(100) (red) at I=1A. The intensity fluctuation at the peak of the spectral distribution is presented in the inset.*

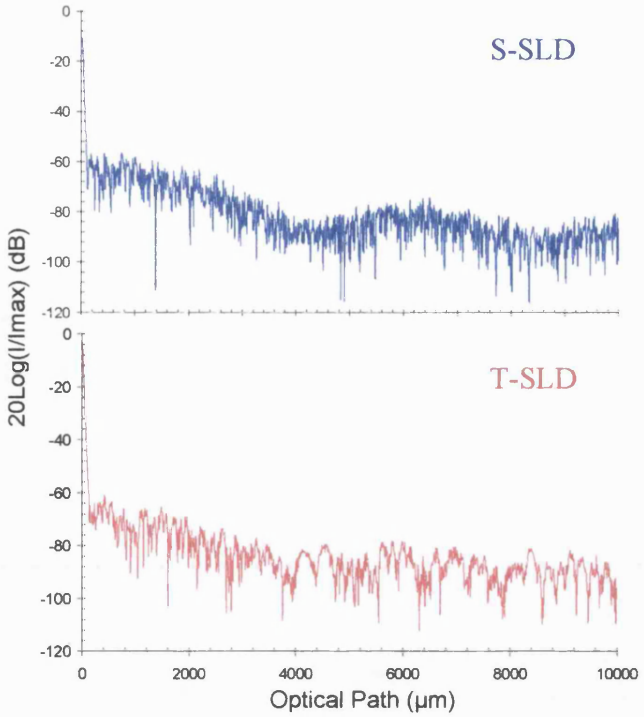

Figure 4.11: *Coherence curves obtained for S-SLDs(50) and T-SLDs(100) at I=1A.*

In an attempt to increase the FWHM spectral width and, therefore, to reduce the coherence length, a new s/c material (QT1819) was designed. The main modification to the epitaxy was in the active layer: the three QWs in the new material have different widths. The material structure and optical properties of material QT1819 are found in Appendix G(ii). The spectra of material QT1819 is compared to material QT1614 for S-SLD(50) at I=3A in Figure 4.12. The FWHM spectral width is 40.0nm, almost a factor of three increase over QT1614, and λ_{PEAK} is 1000nm. The coherence length is 16.5μm making SLDs fabricated from QT1619 a good optical source for OCT applications, [4-9].

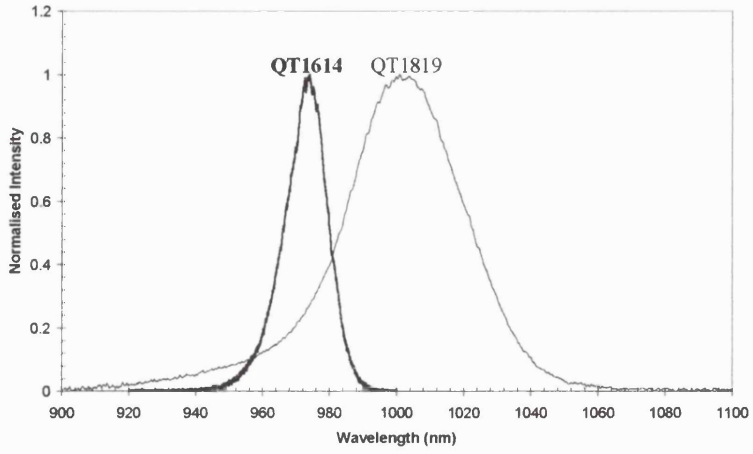

Figure 4.12: *Spectra measured from S-SLD(50) fabricated from QT1819 and QT1614.*

4.2.3: Near and far field characteristics

The theoretical and experimental NF intensity profiles of S-SLD(50) and T-SLD(100) for various injection currents are plotted in Figure 4.13 (a) and (b) respectively. The theoretical results are in good agreement with the experimental results. A reduction in the tail of the profiles is expected at higher currents because the effect of current spreading and carrier diffusion becomes relatively less significant. This effect is incorporated into the ray model by increasing the q term in the SG function, equation (3.1).

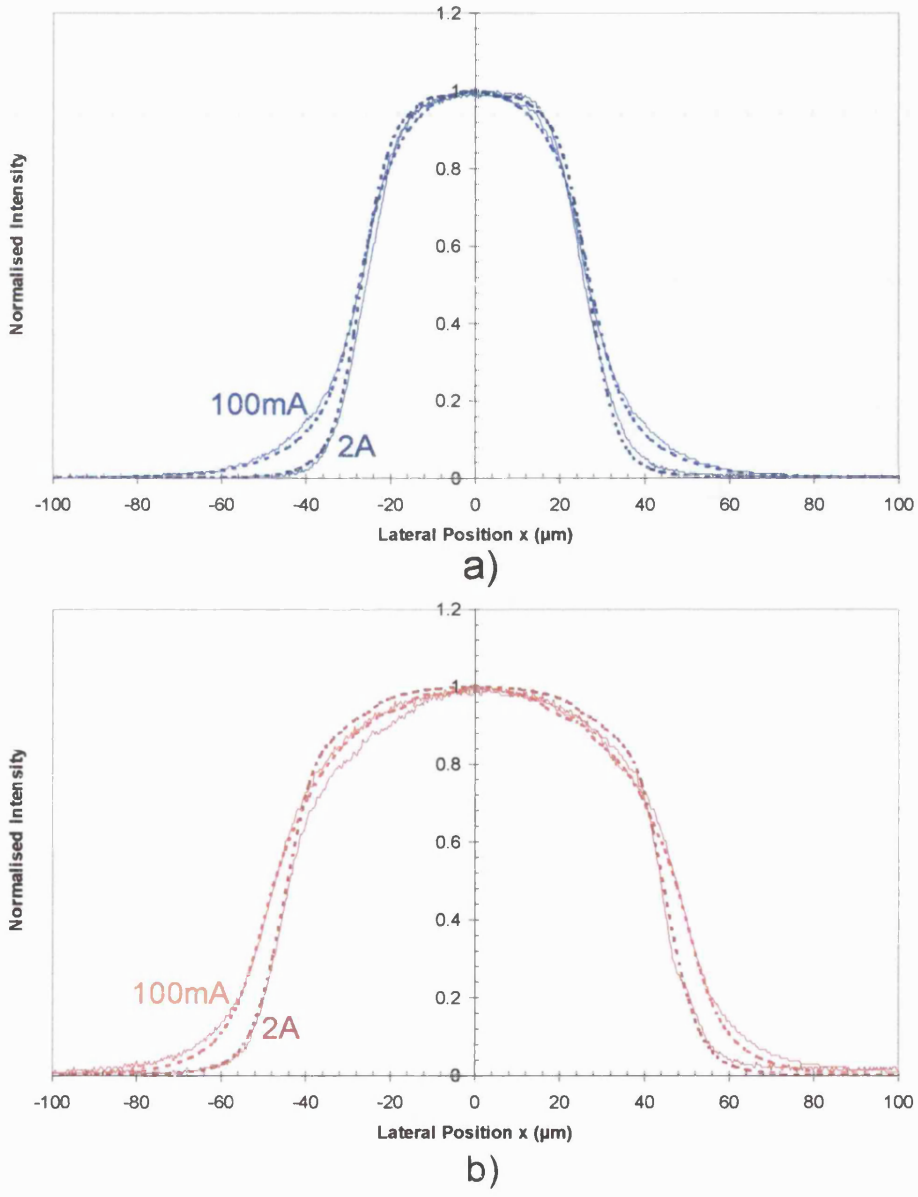

Figure 4.13: *Theoretical (dashed) and experimental (solid) NF intensity profile measured from (a) S-SLDs(50) and (b) T-SLDs(100) at various injection currents.*

The theoretical and experimental vertical FF patterns (FF_y) measured from S-SLDs and T-SLDs for various injection currents are plotted in Figure 4.14. The FF_y, which is computed by taking the Fourier Transform of the fundamental vertical mode supported by the material, is given by

$$FF_y(k_y) = \frac{1}{2\pi}\int_{-\infty}^{\infty} E_x(y)e^{(ik_y y)}dy \qquad (4.4)$$

where $E_x(y)$ is the electric field component discussed in Section 2.2 and

$$k_y = k_0 \sin\theta_v \qquad (4.5)$$

where k_0 is the free space wave number.

The vertical mode profile is material dependent and, hence, it typically remains unchanged with current. The FF_y FWHM measured from in-house fabricated devices is 46.3°, comparing well with the theoretical estimated value of 46.8°.

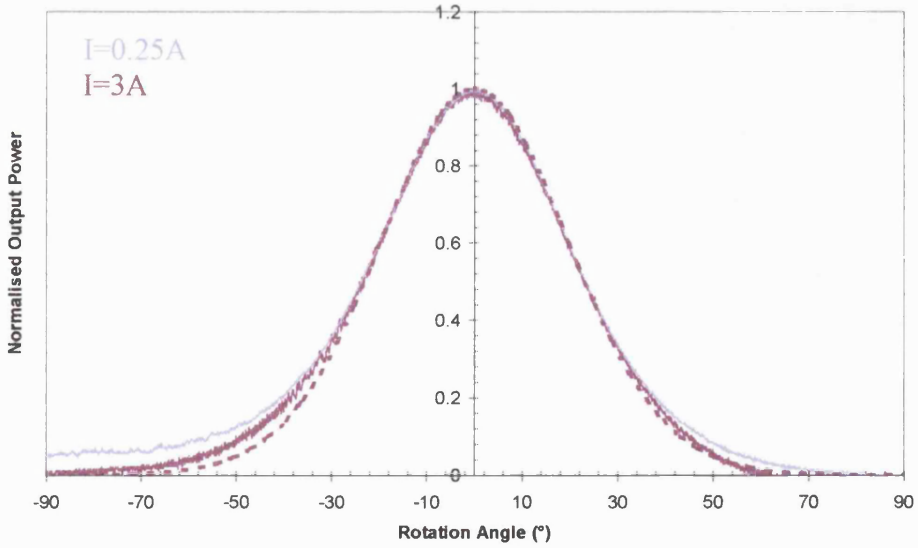

Figure 4.14: *Theoretical (dashed) and experimental (solid) vertical FF pattern measured from SLDs at various injection currents.*

The theoretical and experimental lateral FF patterns measured from S-SLDs(50) and T-SLDs(100) are presented in Figure 4.15 (a) and (b) respectively. In all cases the theoretical results from the model seen to be in good agreement with the

measured results, indicating that the model is accurate. In general, the broad FF typical of spontaneous emission at low currents reduces to the typical bell-shaped characteristic of ASE. After the onset of optical gain saturation the FWHM beam width increases slightly (15% for T-SLDs and 30% for S-SLDs). This trend is clearly seen in Figure 4.16, which presents the change in FF FWHM with injection current for T-SLDs and S-SLDs. For all SLDs, the lateral FWHM reaches a minimum value at the same injection current corresponding to the maximum W-P efficiency. This indicates that the lateral FF FWHM is affected by optical gain saturation. With the onset of optical saturation the contribution of rays that are perpendicular to the output facet is slightly (relatively) reduced resulting in an increase in the FWHM beam width.

For future reference, the direction in which the beam divergence is larger is typically referred to as the *'fast axis'*. Therefore, in this case, the y-axis (vertical) is the fast axis while the x-axis (lateral) is generally the *'slow axis'*.

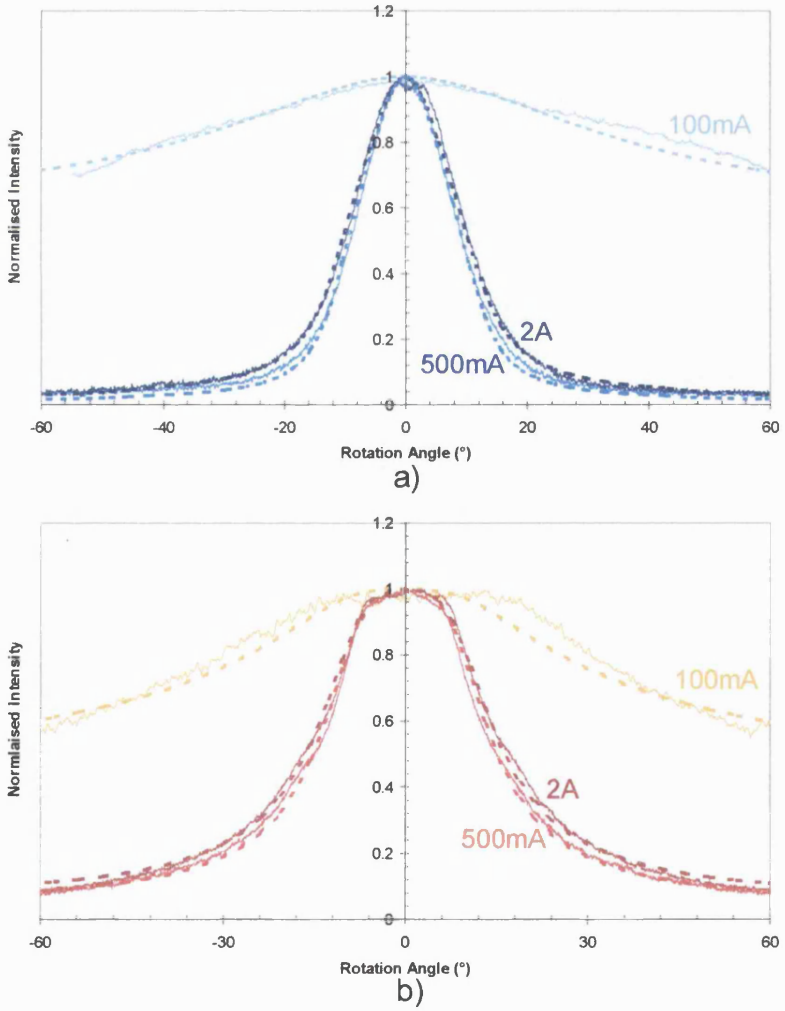

Figure 4.15: *Theoretical (dashed) and experimental (solid) lateral FF pattern measured from (a) S-SLDs(50) and (b) T-SLDs(100) at various injection currents.*

The lateral far field, measured from S-SLDs have a characteristic 'triangular' profile derived from the fact that the rays perpendicular to the output facet present the highest gain. On the other hand, the lateral far field measured from T-SLDs have a 'flat-top' profile as expected for an injection metal contact of triangular geometry. In both cases, the profiles are rounded because of current spreading and carrier diffusion effects, [4-10]. The 'flat-top' and 'triangular' profile of T-SLDs and S-SLDs are plotted in Figure 4.17 along with intermediate cases provided by partially tapered SLDs.

Experimental lateral far field profiles measured from P-SLDs at different injection currents are presented in Figure 4.18. Corresponding theoretical profiles results are also shown obtaining an excellent agreement with the experimental results, therefore, indicating the versatility of the model to simulate SLDs of various geometries.

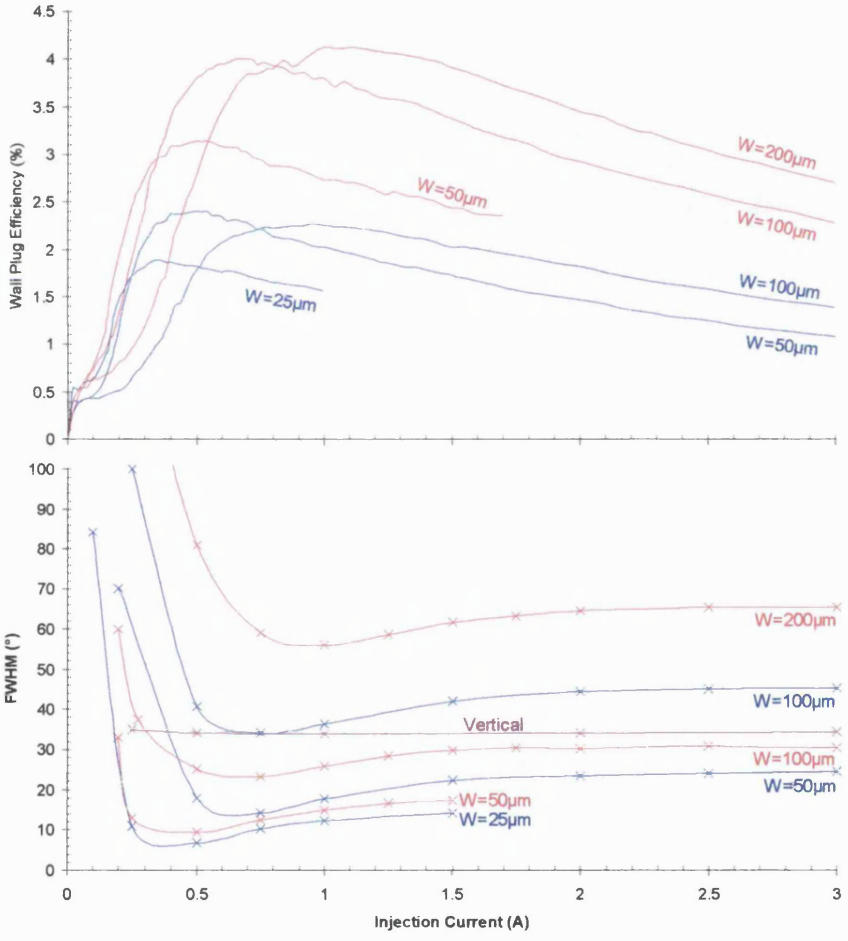

Figure 4.16: *The change in vertical and lateral FF FWHM at various injection current measured from S-SLDs (blue) and T-SLDs (red) and corresponding W-P efficiencies.*

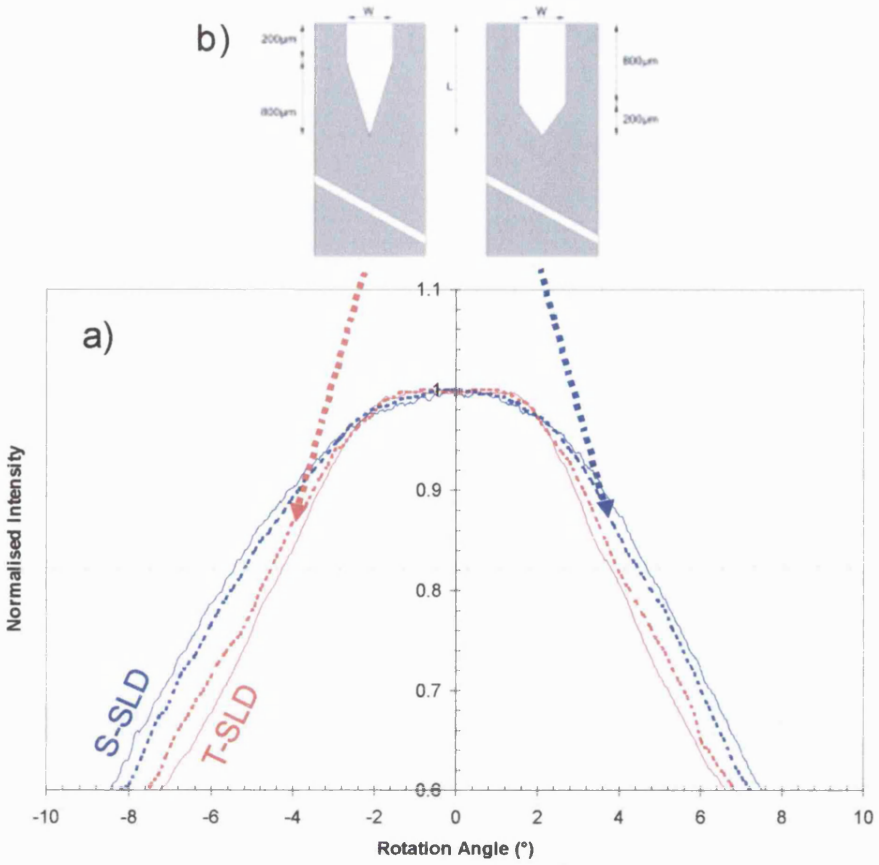

Figure 4.17: (a) *The 'flat-top' and 'triangular' profiles measured from S-SLDs (blue), T-SLDs (red) and partially tapered SLDs (dashed). (b) Top view schematic of partially tapered SLDs is also shown for clarity.*

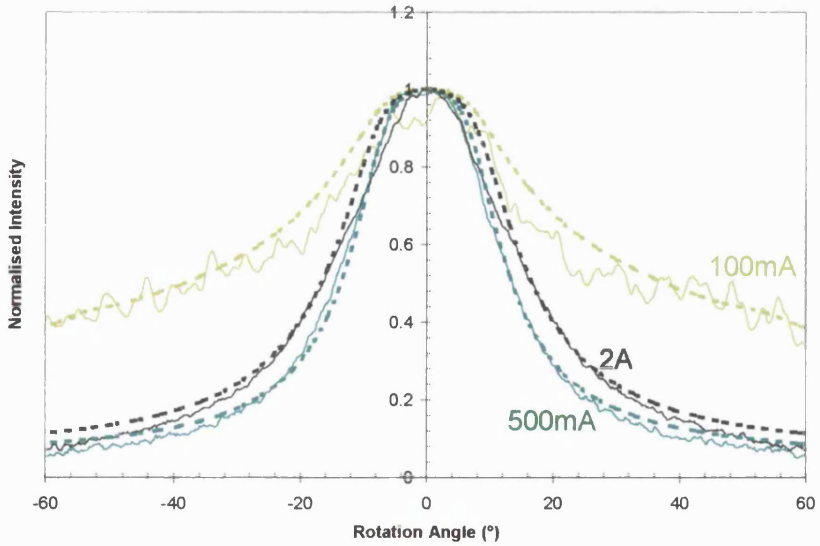

Figure 4.18: *Theoretical (dashed) and experimental (solid) lateral FF pattern measured from P-SLD at various injection currents.*

4.2.4: Degree of Polarisation

The degree of light polarisation is defined as

$$DOP = \frac{P_{TE} - P_{TM}}{P_{TE} + P_{TM}} \qquad (4.6)$$

where P_{TE} and P_{TM} are the power contributed by TE and TM polarised light (radiation) respectively.

Since the material used to fabricate the devices is comprised of strained QWs the SLD output is expected to be mainly TE polarised, in fact, the DOP measured from both S-SLDs and T-SLDs reaches the value of 0.97, corresponding to dominant TE polarisation, immediately after the on-set of ASE operation, Figure 4.19. The insets in Figure 4.21 present polarisation resolved radiation patterns measured at 2A injection current, confirming that TM-polarised emission is purely spontaneous (Lambertian profile) while TE-polarised emission is dominated by optical gain (ASE) resulting in a $cos^n(\theta)$ profile with n ~ 12.

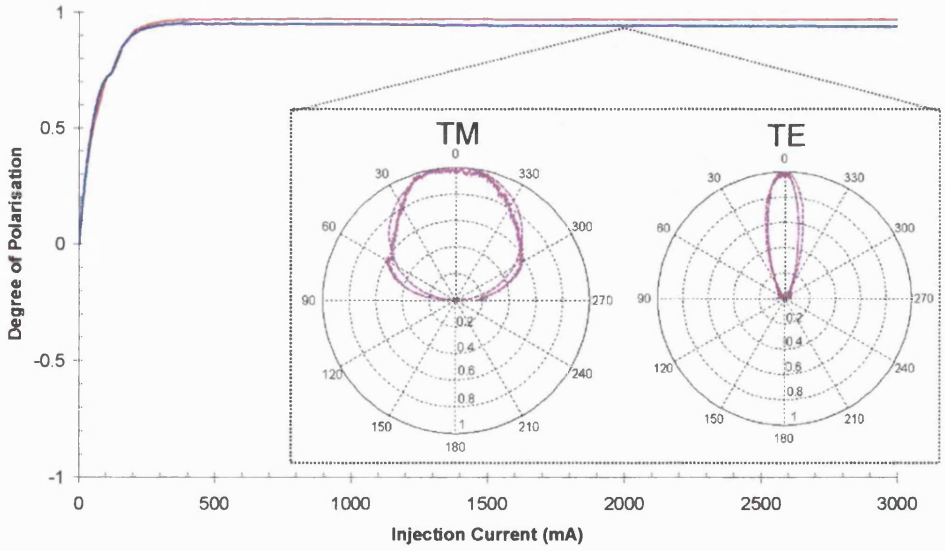

Figure 4.19: *DOP measured from high power S-SLDs (blue) and T-SLDs (red) fabricated in-house from strained QW semiconductor material. The insets represent polarisation resolved (TM and TE) radiation patterns: solid line: profiles measured from S-SLDs at I=2A; dotted line: theoretical profiles obtained using cos(θ) for TM and $cos^n(\theta)$ with n=12 for TE polarisation.*

4.3: Techniques to improve the SLD W-P efficiency

Optical saturation has a negative effect on the efficiency of a SLD and is caused by large photon densities depleting the carriers at the rear of the device active region. Optical feedback from the output facet is amplified, thereby significantly reducing the carrier density (and optical gain) in the active region. The most common method for reducing the amplified feedback is to apply an AR coating onto the output facet of the SLD, [4-11]. Also, the possibility of modifying the SLD geometry to reduce optical saturation is discussed by using modelling results to find the optimum device length to maximise the optical power output.

An alternative method was proposed in [4-12] whereby the fraction of spontaneous emission coupled into the forward travelling photon density is increased by incorporating an index-guided region in the device. The result is a reduction of power lost to the lossy region outside the active region.

4.3.1: AR coatings

AR coatings have been applied by sputtering a thin film of ZrO_2/TiO_2 onto the SLD output facet using an electron beam gun, Appendix H. The AR coated devices presented here are all fabricated from material QT1137.

The theoretical and experimental LI characteristic and W-P efficiency measured from AR coated S-SLD(100) and T-SLD (200) are plotted in Figures 4.20 (a) and (b) respectively. The LI characteristic measured using CW drive current is presented in the inset. Optical output powers in excess of 1.3W are measured at 3A from AR coated T-SLD(200), the highest SLD output power presented in literature to the best knowledge of the author, [4-13], with a maximum 16% W-P efficiency. With respect to un-coated T-SLDs the output power measured from the AR coated devices presents a factor of five increase in output power and W-P efficiency with a corresponding shift and flattening of the W-P efficiency peak at higher currents. The optical power saturation point is estimated from the change of slope efficiency against input current. As expected, it is found that the optical power saturation point changes before and after AR coating, obtaining 0.6A and 0.8A, respectively for S-SLDs, and 0.8A and 1.5A respectively for T-SLDs. The SLDs tested under CW operation achieved output power in excess of 67mW at I=600mA from AR coated T-SLDs(200), an improvement of 64-70% improvement with respect to non-AR coated devices. Thermal roll-over is observed at the maximum CW optical power level achieved (67mW), corresponding to 600mA and

850mA input current for AR T-SLDs(200) and AR S-SLDs(100), respectively. The results presented in the inset of Figure 4.20 (a) indicate that maximum CW output power is limited by the thermal properties of the s/c material used to fabricate the SLDs (corresponding to approximately 2MWcm^{-2} internal power density at the facet). However, it is noticed that also under CW operation T-SLDs are more efficient than S-SLDs.

The theoretical results were computed by changing the output facet reflectivity of the T-SLD and S-SLD to 1.5% and 1.7% respectively. All other material constants remained unchanged.

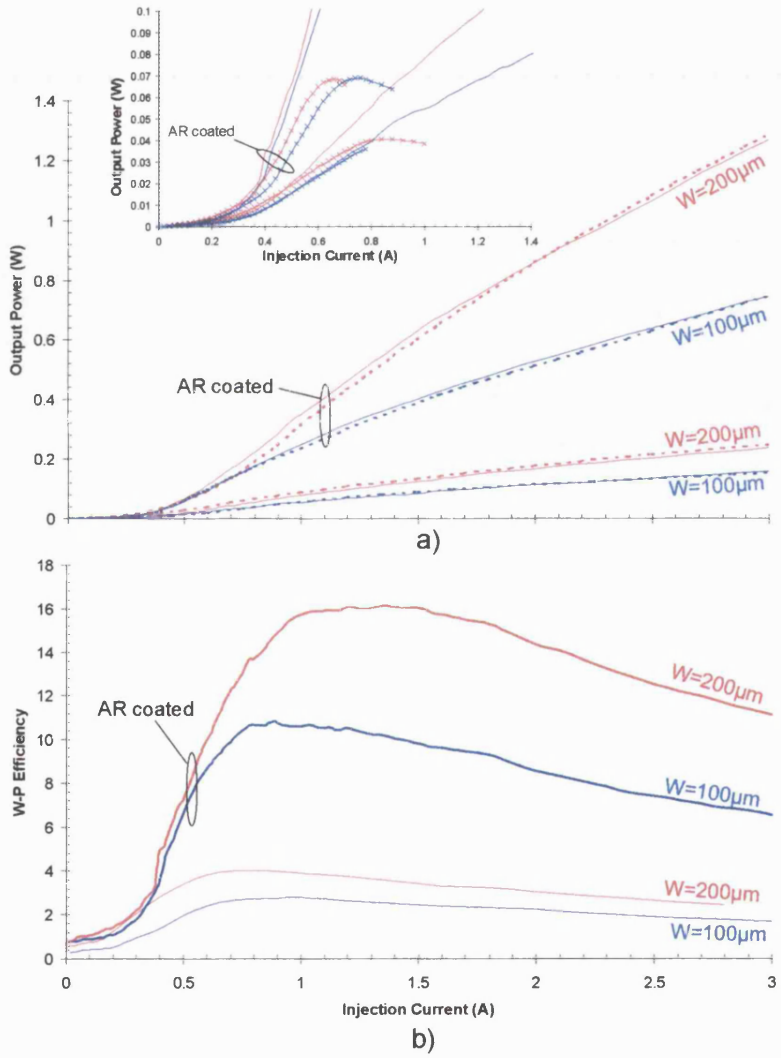

Figure 4.20: (a) *Theoretical (dashed) and experimental (solid) LI characteristics obtained from S-SLD(100) (blue) and T-SLD(200) (red) before and after AR coating. The LI characteristic measured using a CW drive current for the same devices before and after AR coating is presented in the inset (symbol: X). (b) Experimental W-P efficiency obtained from S-SLD(100) (blue) and T-SLD(200) (red) before and after AR coating.*

The spectra, intensity ripple and corresponding coherence curves measured from T-SLDs(200) at I=2A before and after AR coating are plotted in Figures 4.21 (a), (b) and (c), respectively. The spectra measured from T-SLDs(200) before and after AR coating are similar but wider after AR coating. The broader spectra is a result of Fabry-Perot modulation suppression provided by the AR coating and is evident in the reduced intensity ripple presented in Figure 4.21 (b). Qualitatively, from Figure 4.21 (c), it is noticed that the coherence curve for AR coated T-SLD(200) has less pronounced secondary sub-peaks with respect to that of the non-AR coated T-SLD(200).

The simulated carrier density distribution and photon density distribution obtained for S-SLD(50) at I=2A for various output facet reflectivities is plotted in Figures 4.22 (a) and (b), respectively. For the ideal case, R_0=0.0 and R_L=0.0, the carrier densities at the front and rear facet are the same. Depletion at the rear (z=0) of the active region is reduced due to a decrease in the reflected optical signal at the output facet. In turn the amplification of the forward travelling photon density is increased resulting in a more efficient device, as shown in Figure 4.23. However, high quality AR coatings that approach the ideal case are difficult to achieve and usually require multiple layers.

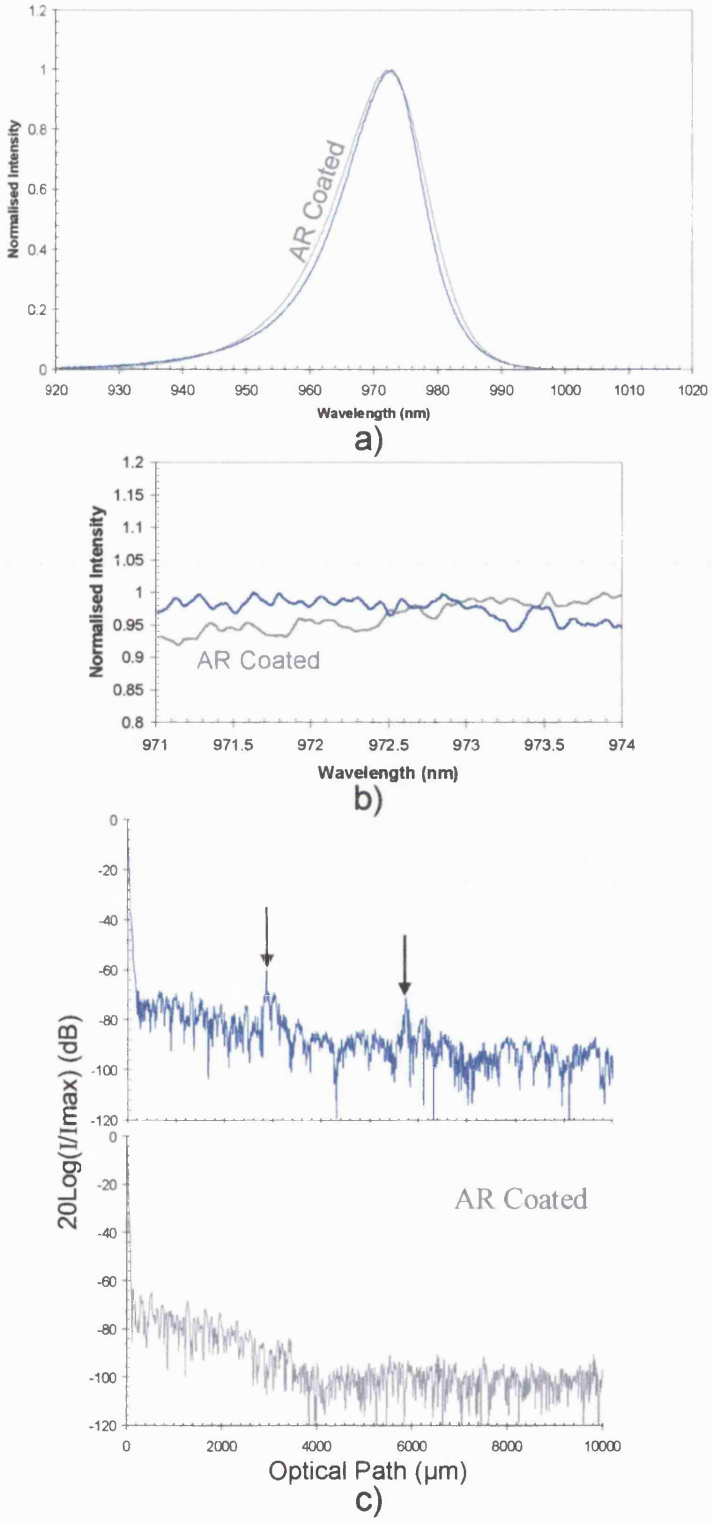

Figure 4.21: (a) *Spectra measured from T-SLDs(200) at I=2A before and after AR coating. (b) The intensity fluctuation at the peak of the spectral distribution. (c) Coherence curve measured from T-SLDs(200) at I=2A before and after AR coating. Arrows indicate the sub-peaks in the non-AR coated coherence curve.*

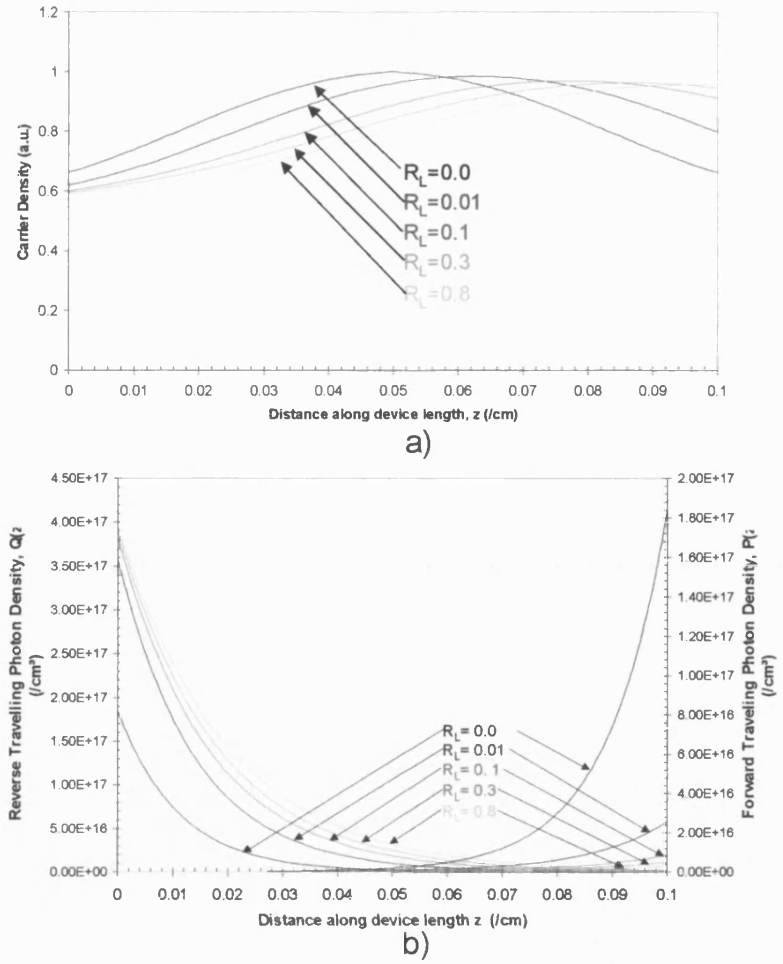

Figure 4.22: (a) *Simulated carrier distribution along the length of S-SLD(50) at I=2A for various output facet reflectivities. (b) Simulated forward and reverse photon density distributions along the length of S-SLD(50) at I=2A for various output facet reflectivities.*

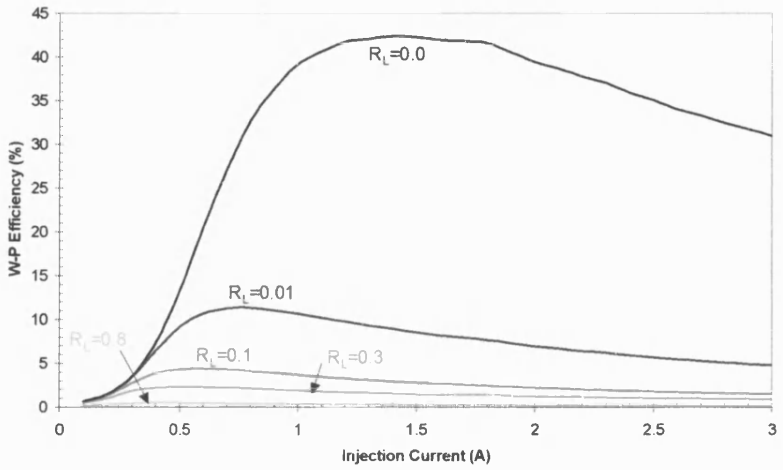

Figure 4.23: Simulated W-P efficiency calculated for S-SLD(50) for various output facet reflectivities assuming VI curve presented in Appendix G(i), Figure G(i).2.

4.3.2: S-SLD Optimum length

The optimum length (L_{OPT}) of a S-SLD is obtained using the model described in Chapter 2. The simulated output power of S-SLD(50) for various device lengths and currents is plotted in Figure 4.24. Experimental results are included for comparison. The optimum length for S-SLD(50) is presented in Table 4.3 for various injection currents.

Table 4.3: *Optimum lengths of S-SLD(100) for various injection currents*

Injection current (mA)	Optimum length (mm)
500	605
1000	655
2000	705
3000	750

At I=3A, a 15% increase in output power is obtained from S-SLDs with an optimum length compared to S-SLDs with L=1mm. A similar increase is obtained for all injection currents. The optimum length of a SLD depends on the optical saturation level and the injection current density. Considering a constant injection current, a device with active region length smaller than L_{OPT} is less efficient due to large optical saturation. A device with length greater than L_{OPT} has a smaller current density and hence smaller optical gain due to the larger active region area.

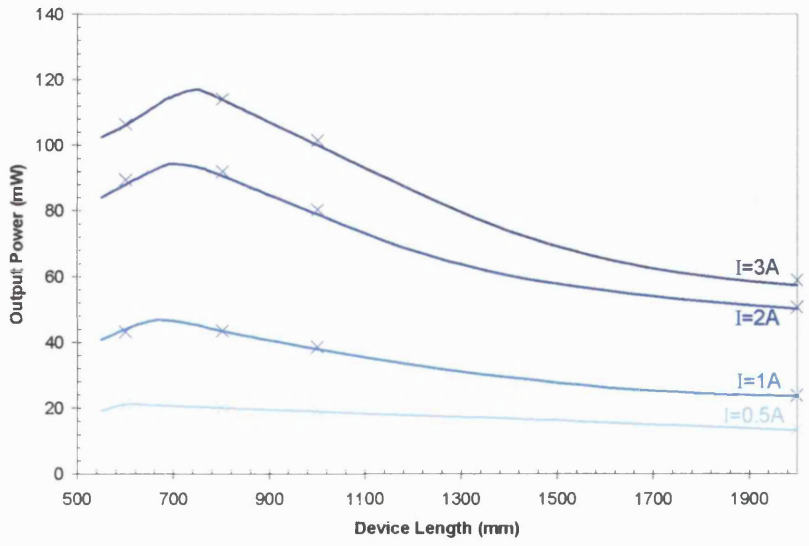

Figure 4.24: *Simulated output power of S-SLD(50) for various active region lengths and injection currents. X: Experimental data.*

The optimum length also depends on the output facet reflectivity, R_L, and device contact width as both effect optical saturation and current density respectively. The change in optimum length with varying output facet reflectivity, assuming R_0=0, and injection current is presented in Figure 4.25. An increase in output facet reflectivity, and hence greater optical saturation, decreases the optimum length value of the S-SLD. Conversely, less optical saturation in the rear of the active region, provided by low facet reflectivities, slightly increases the value of L_{OPT}. An increase in SLD contact width results in a smaller value for L_{OPT} so that the current density required for optimum efficiency is kept constant.

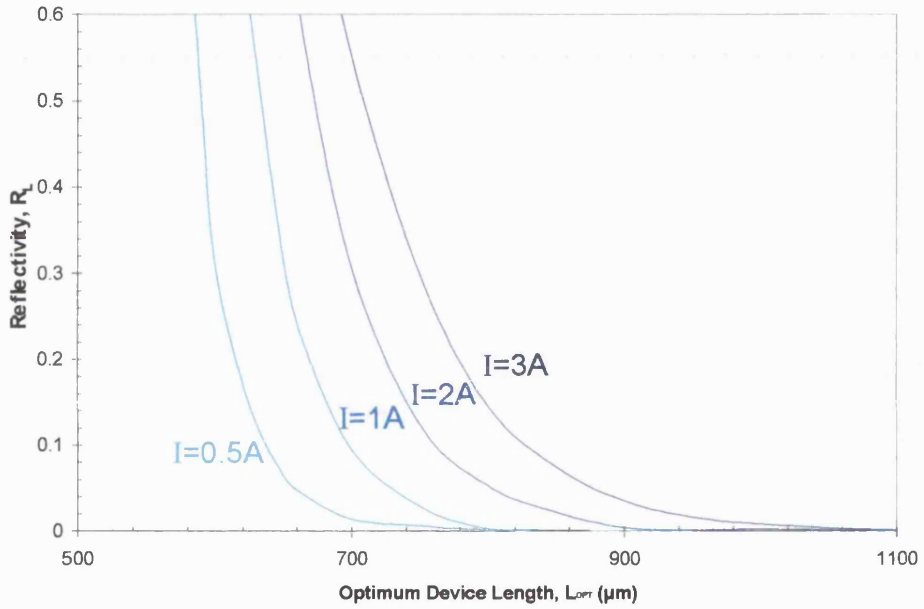

Figure 4.25: *Simulated optimum length of S-SLD(50) as a function of output facet reflectivity and injection current.*

4.3.3: Gain - index guided S-SLDs and T-SLDs

The devices presented so far have been fabricated with a shallow etched rib providing essentially current confinement but no lateral (effective) refractive index-guiding. The fraction of spontaneous emission coupled to the forward travelling photon density, δ_f, Chapter 2: equation (2.6), depends on the dimensions of the current injection region (W and L) and on the lateral Effective Refractive Index (ERI) step, provided by a deeply etched rib, Chapter 2: Figure 2.3, [4-12]. However, lateral ERI guiding will also increase the feedback provided by output facet reflections with the

result of increased optical saturation. The effect of an ERI guiding region incorporated in the SLD design is investigated in this Section.

The S-SLD and T-SLD structures investigated are described in Figure 4.26. The sections where ERI guiding is provided along the etched rib (shaded regions in Figure 4.26) are characterised by 0.9μm etch depths, corresponding to a 0.15% (lateral) ERI step.

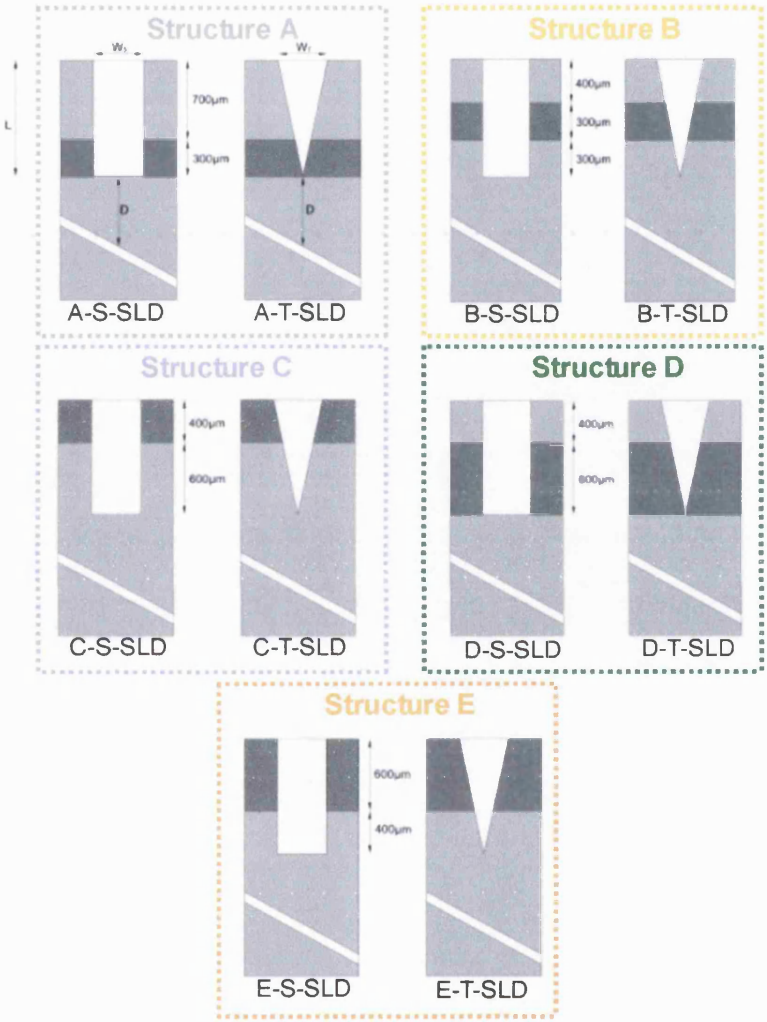

Figure 4.26: *Top view schematic of S-SLD and T-SLD with ERI guiding sections along the rib length. The rib section with RI guiding is shaded: W_S is 50μm; W_T is 100μm; L is 1mm.*

The LI characteristic and W-P efficiency of the gain-index guided S-SLDs and T-SLDs are plotted in Figures 4.27 and 4.28 respectively. From all the structures, an increase in W-P efficiency, compared to gain-guided SLDs, is only measured from A-S-SLDs and D-S-SLDs. The increase in output power is 8% for A-S-SLDs and 22% for D-S-SLDs at I=3A. The improvement in W-P efficiency is due to the ERI guiding at the

rear of the active region increasing δ_f for rays that contribute the most power. In addition, the combination of weak guiding at the output facet and ERI guiding at the rear of the active region will not significantly increase optical feedback or optical gain saturation, [4-12]. For the other partially index-guided S-SLD structures the W-P efficiency is reduced, indicating that the ERI guiding increases optical saturation by increasing δ_r.

On the other hand, the W-P efficiency for all T-SLD structures incorporating ERI guiding regions is reduced. In fact, in such devices ERI guiding significantly increases the amount of optical feedback coupling with the rear of the active region, Figure 4.29, and hence, increases optical saturation.

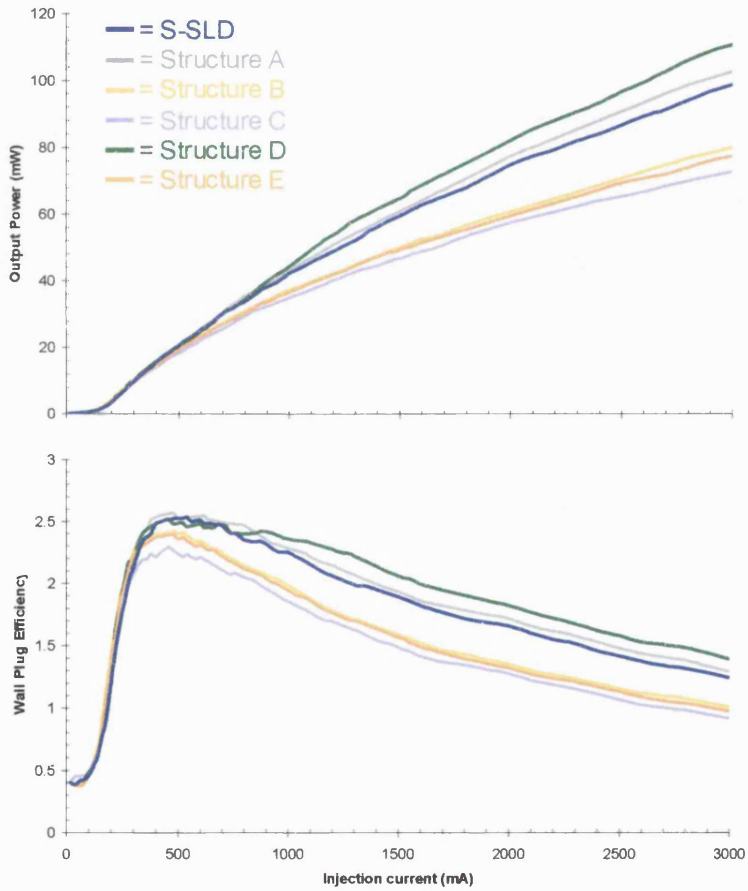

Figure 4.27: *Experimental LI characteristic and W-P efficiency for gain-index guided S-SLDs*

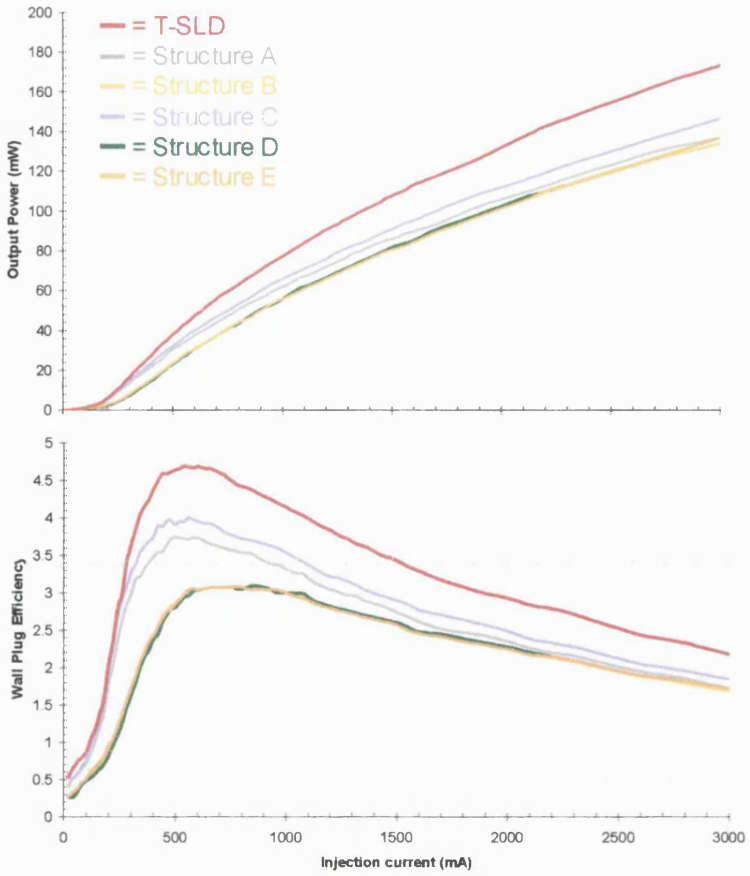

Figure 4.28: *Experimental LI characteristic and W-P efficiency for gain-index guided T-SLDs*

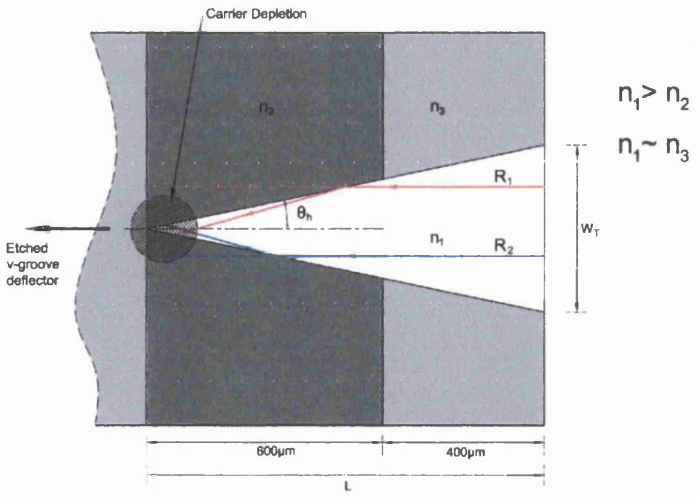

Figure 4.29: Schematic showing the ERI guiding of rays (R_1 and R_2) originating from the output facet of a D-T-SLD. The increase in optical feedback coupling with the rear of the active region causes additional optical saturation.

The change in lateral FF FWHM with injection current for D-S-SLDs and D-T-SLDs is plotted in Figure 4.30. After the onset of optical gain saturation the FWHM beam width increases 50% for the D-T-SLD compared to 30% for the T-SLDs. The change in FWHM for D-S-SLDs and S-SLDs is the same indicating equal amounts of saturation for high injection currents. The lateral FF pattern for the above mentioned SLDs at I=1A is presented in the inset of Figure 4.30. The FF pattern is similar for the S-SLDs but broader for the D-T-SLD compared to the T-SLD indicating an increase in gain saturation.

The spectral distribution and coherence curves for D-S-SLD and S-SLD at I=2A are presented in Figures 4.31 (a) and (b), respectively. The spectra measured from the D-S-SLD and the S-SLD are similar. The coherence curve shows a larger secondary sub-peak for the D-S-SLD than the S-SLD indicating a slight increase in spectral modulation for gain-index guided SLD.

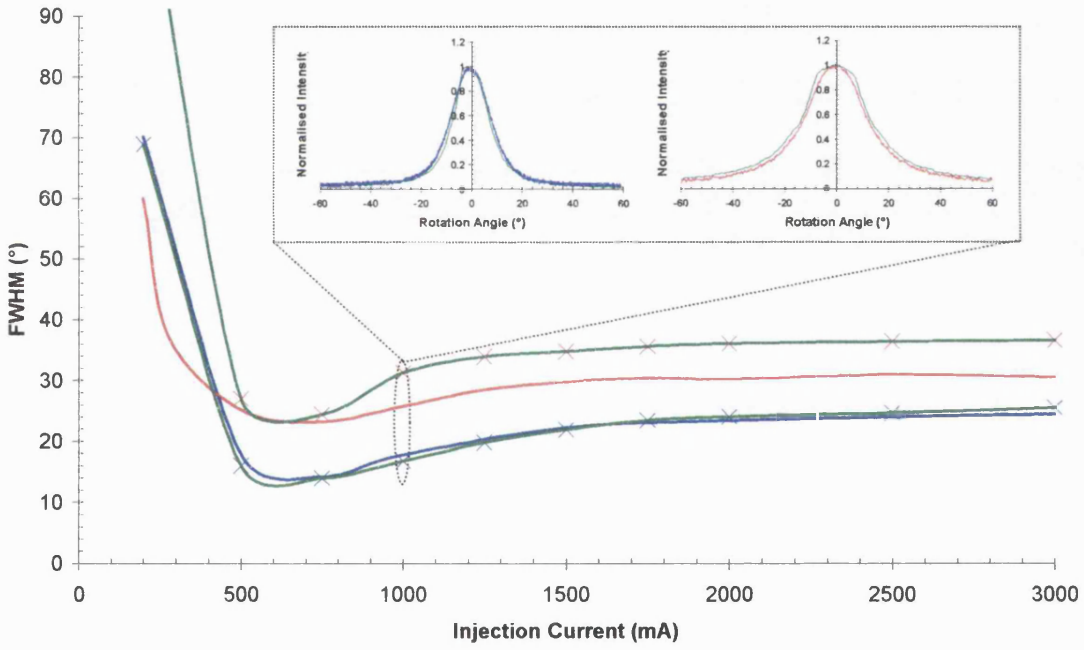

Figure 4.30: *The change in lateral FF FWHM with injection current measured from D-S-SLDs (green with blue cross), D-T-SLDs (green with red cross), S-SLDs (blue) and T-SLDs (red). Corresponding FF patterns comparing D-S-SLDs (green) and D-T-SLDs (green) to S-SLDs (blue) and T-SLDs (red) at I=1A respectively are presented in the inset.*

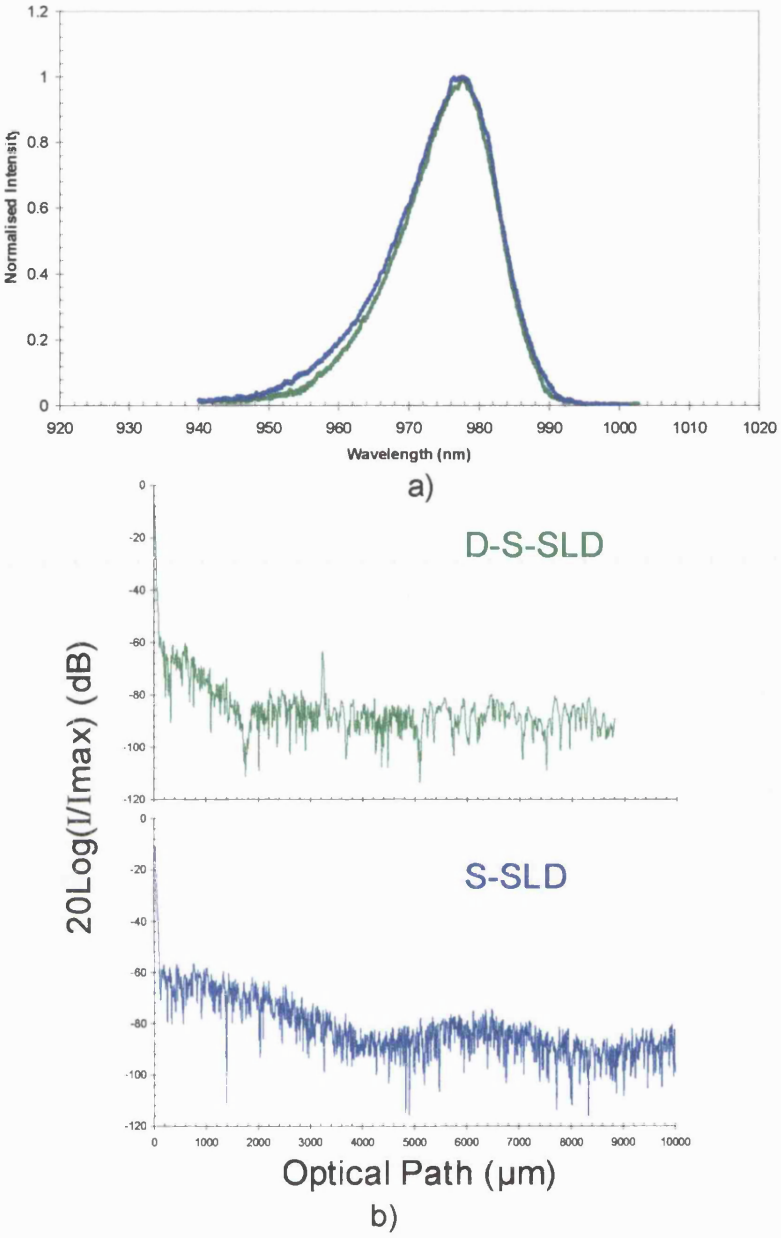

Figure 4.31: (a) *Spectra measured from D-S-SLDs (green) and S-SLDs (blue) at I=2A. (b) Coherence curves measured from D-S-SLDs (green) and D-T-SLDs (blue) at I=2A.*

4.4: Summary

In this Chapter the theoretical and experimental characterisation of in-house fabricated S-SLDs and T-SLDs was presented. The results obtained from the models described in Chapters 2 and 3 compare well with the theoretical results and can be used to simulate the operational characteristics of SLDs with any contact geometry. The effect of optical saturation on the characteristics of SLDs was discussed.

This Chapter also described an investigation into techniques to improve SLD efficiency. Three methods of improving SLD efficiency were described: AR coatings, active region length optimisation and ERI guiding. The AR coatings provided a factor of five increase in W-P efficiency for T-SLDs and S-SLDs with output powers in excess of 1.3W and 16% peak W-P efficiency.

A method of finding the optimum length of a S-SLD using the model described in Chapter 2 was presented. The optimum length was shown to be dependent on optical saturation and current density. The effect of different output facet reflectivities, drive currents and device dimensions on the optimum length was discussed.

An increase of 22% in output power and 0.15% W-P efficiency was obtained from an ERI guided S-SLD when the index-guiding region was situated at the rear of the metal contact. ERI guiding in T-SLDs significantly increased optical saturation and therefore reduced device efficiency.

References

[4-1] Kapon E., Ed., *Semiconductor Lasers II: Materials and Structures*, Academic Press, London, 1999

[4-2] Koyama F., Liou K.-Y., Dentai A. G., Tanbun-ek T., and Burrus C. A., *Multiple-Quantum-Well GaInAs/ GaInAsP Tapered Broad-Area Amplifiers with Monolithically Integrated Waveguide Lens for High-Power Applications*, IEEE Photonics Technology Letters, Vol. 5, No. 8, August 1993, pp. 916-919.

[4-3] Middlemast I., Sarma J., and Yunus S., *High Power Tapered Superluminescent Diodes Using Novel Etched Deflectors*, Electronics Letters, Vol. 33, No. 10, May 1997, pp. 903-904.

[4-4] Goebel E.O., Hildebrand O., and Lohnert K., *Wavelength Dependence of Gain Saturation in GaAs Lasers*, IEEE Journal of Quantum Electronics, Vol. QE-13, No. 10, October 1977, pp. 848-854.

[4-5] Kressel H., and Butler J.K., *Semiconductor Lasers and Heterojunction LEDs*, Academic Press, London, 1977, Chapter 14.

[4-6] Goodman J.W., *Statistical Optics*, John Wiley and Sons, New York, 1985.

[4-7] L. Fu, H. Schweizer, Y. Zhang, L. Li, A. M. Baechle, S. Jochum, G. C. Bernatz, S. Hansmann, *Design and Realization of High-Power Ripple-Free Superluminescent Diodes at 1300nm*, IEEE J. Quantum Electronics, Vol. 40, No. 9, September 2004, pp.1270-1274.

[4-8] T.-K. Ong, M. Yin, Z. Yu, Y.-C. Chan, Y.-L. Lam, *High performance quantum well intermixed superluminescent diodes*, Meas. Sci. Technol., Vol.15, 2004, pp. 1591-1595.

[4-9] A. V. Zvyagin, K. K. M. B. Dilusha Silva, S. A. Alexandrov, T. R. Hillman, J. J. Armstrong, T. Tsuzuki, D. D. Sampson, *Refractive index tomography of turbid media by bifocal optical coherence refractometry*, Vol. 11, No. 25, Optics Express, December 2003, pp. 3503-3517.

[4-10] Causa F., and Sarma J., *Realistic Model for the Output Beam Profile of Stripe and Tapered Superluminescent Light-emitting Diodes*, Applied Optics, Vol. 42, No. 21, July 2003, pp. 4341-4348.

[4-11] Dutta N. K., Nelson R. J., Wright P. D., Besomi P., and Wilson R. B., *Optical Properties of a 1.3-μm InGaAsP Superluminescent Diode*, IEEE Transactions on Electron Devices, Vol. ED-30, No.4, April 1983, pp. 360-363.

[4-12] Alphonse G. A., Connolly J. C., Dinkel N. A., Palfrey S. L., and Gilbert D. B., *Low Spectral Modulation High-Power Output from a new AlGaAs*

Superluminescent Diode/ Optical Amplifier Structure, Applied Physics Letters, Vol. 55, No. 22, November 1989, pp. 2289-2291.

[4-13] Burrow L.D., Causa F., and Sarma J., *1.3W Ripple-free Superluminescent Diodes*, IEEE Photonics Technology Letters, accepted May 2005.

Chapter 5
Coupling Superluminescent Diodes to Optical Fibres

5.1: Introduction

An investigation into SLD to optical fibre coupling is presented in this chapter. Two methods of fibre coupling are described: Butt-Coupling (B-C) and system of lenses coupling. Coupling into single-mode and multi-mode fibres is discussed for T-SLDs and S-SLDs including the analysis of misalignment and system (i.e. scattering, reflections and attenuation) losses and the theoretical analysis of coupling to the fibre.

A brief review of s/c optical source to optical fibre coupling methods is presented in Section 5.2. The B-C technique is described in Section 5.3 and includes: the procedure and equipment needed for the measurements, a theoretical model to compute B-C efficiency based on the SLD radiation pattern and optical properties of the fibre, and the experimental results. A coupling technique using a system of lenses is described in Section 5.4 with corresponding experimental results.

5.2: Methods of coupling

Effective power coupling between optical source and optical fiber is a concern for many applications. Low loss coupling is essential for optimal performance, as high loss coupling means an optical source has to be operated at a higher power level than necessary resulting in reduced device lifetime. As a consequence optical source to fibre coupling is an important field of research.

The method of coupling an optical source to a fibre depends on the application considered. For applications where space is limited (e.g., integrated circuits, [5-1]) non-intrinsic optics such as lenses are inappropriate. For such situations B-C the fibre to the source is the best technique. However, if the output beam of the source is divergent then simple B-C, to single-mode fibres in particular, is inefficient. Various methods for improving B-C efficiency, without increasing physical size, include: tapered hemispherical end fibres, Figure 5.1a, [5-2]; microlens fibres, Figure 5.1b, [5-3]; graded index fibres, Figure 5.1c, [5-4]; and conical wedge shaped fibres, Figure 5.1d, [5-5]. Each of these methods improves the acceptance angle of a single-mode or multi-mode fibre.

For applications where coupling efficiency is of primary importance (e.g., Optical fibre communication systems) then external optics (system of lenses) are required, [5-6]. The drawback of using a lens system is the ultra fine tolerances required for lens alignment. Misalignment in a lens system drastically reduces the coupling efficiency. An advantage of using a lens system is the property of beam aberration correction through the appropriate choice of lenses. By correct selection of the lenses, light can be focused to a small spot size (few μm diameter) achieving 1:1 aspect ratio. A wide range of lenses is commercially available to correct aberrations including astigmatism, coma, chromatic, distortion and field curvature. In addition, sophisticated AR coatings can be applied to a lens to improve light transmission at the expense of increased system costs.

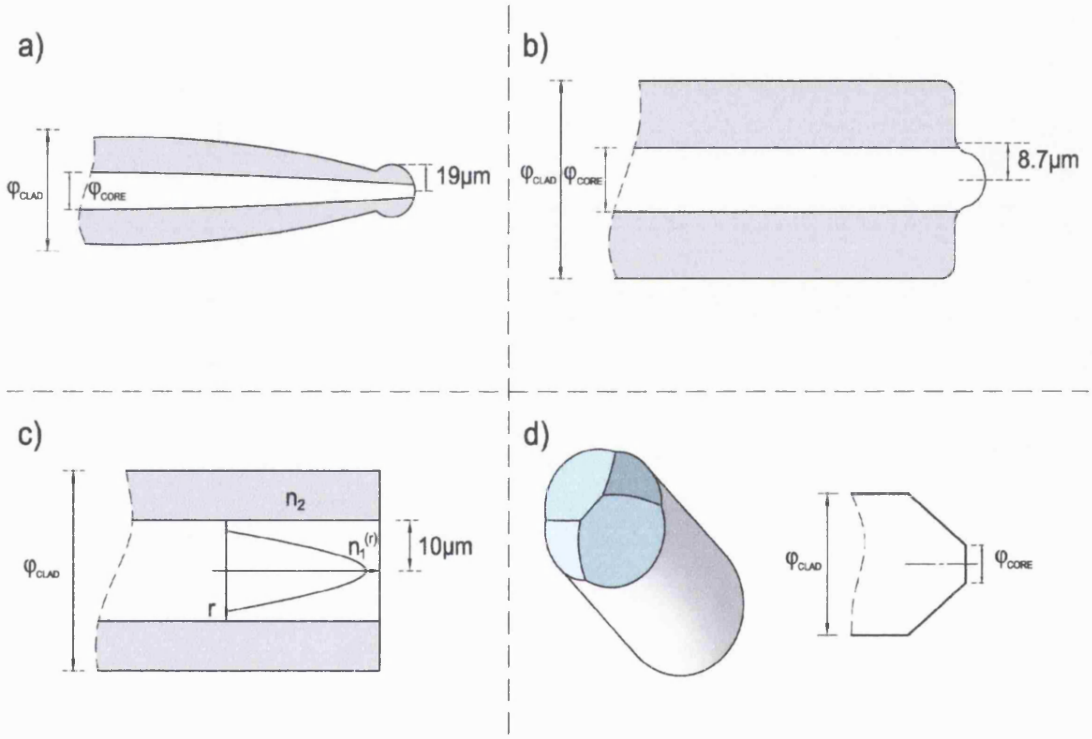

Figure 5.1: *Schematic showing various methods for increasing the acceptance angle of a fibre: a) Hemispherical end fibres, b) Microlens fibres, c) Graded index fibres, and d) Conical wedge shaped fibres.* φ_{CORE} *is the core diameter, and* φ_{CLAD} *is the cladding diameter.*

5.3: Butt-coupling technique

B-C is the simplest method used for coupling light from an optical source to an optical fibre. This technique involves placing the optical fibre, whether Single-Mode Fibre (SMF) or Multi-Mode Fibre (MMF), into close proximity (~20μm) of the emitting edge of the source, as represented in Figure 5.2 where the SLD is used as the optical source. The fibre position (x, y, z) and orientation (angular) are adjusted to achieve maximum coupling. An index-matching gel is placed in between the fibre and the SLD to reduce reflection losses. The equipment used to perform the measurement with this technique is shown in Figure 5.3.

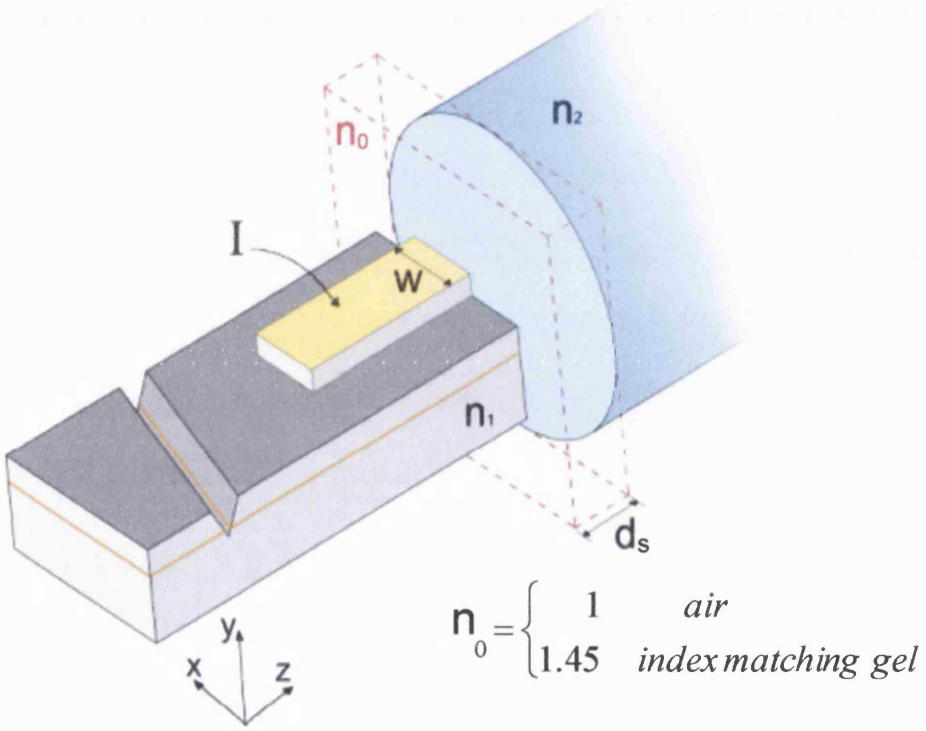

Figure 5.2: *Schematic representation of B-C a SLD to an optical fibre:* n_1 *is the s/c material refractive index,* n_2 *is the fibre glass refractive index,* n_0 *is the refractive index of the surrounding medium,* W *is the SLD stripe contact width, and* d_s *is the fibre to SLD distance.*

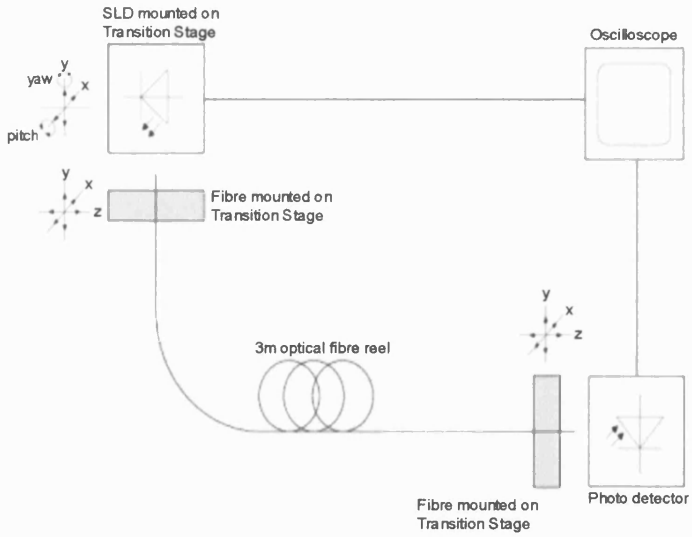

Figure 5.3: *Experimental apparatus used to measure the SLD- to-fibre B-C efficiency.*

5.3.1: Theoretical estimation of the B-C efficiency

The coupling efficiency is found experimentally by the ratio

$$\eta_{B,\exp} = \frac{P_{FIBRE}}{P_{SLD}} \times 100 \tag{5.1}$$

where $\eta_{B,exp}$ is the experimental butt coupling efficiency, P_{FIBRE} is the output power measured at the end of the optical fibre, and P_{SLD} is the output power measured directly from the SLD.

To calculate the coupling efficiency using the ray model described in Chapter 3, the Numerical Aperture (NA) and core diameter (φ_{CORE}) of the fibre must be known. From the NA the acceptance angle of the fibre can be calculated using

$$\theta_a = \sin^{-1}\left(\frac{NA}{n_0}\right) \tag{5.2}$$

where θ_a is the acceptance angle of the fibre, n_0 is the refractive index of the medium outside the fibre. The acceptance angle is used in conjunction with the lateral FF pattern (FF_x, calculated using the model) and vertical FF pattern (FF_y, Section 4.2.3) to

find the ratio of power accepted by the fibre to the overall power emitted by the SLD using the following formula

$$\eta_{x,y} = \frac{\int_{-\theta_a}^{\theta_a} FF_{x,y}(\theta_{h,v})d\theta_{h,v}}{\int_{-\pi}^{\pi} FF_{x,y}(\theta_{h,v})d\theta_{h,v}} \tag{5.3}$$

where η_x is the lateral coupling efficiency; θ_h is the horizontal emission angle of light from the SLD; and similarly in the vertical direction.

The simulated butt coupling efficiency, $\eta_{B,sim}$, is calculated using, [5-7],

$$\eta_{B,sim} = M\frac{\eta_x\eta_y}{\eta_x + \eta_y} \tag{5.4}$$

and

$$M = \begin{cases} 1 & W < \varphi_{CORE} \\ \dfrac{\pi\left(\frac{\varphi_{CORE}}{2}\right)^2}{Wd} & W > \varphi_{CORE} \end{cases} \tag{5.5}$$

where M is the core mismatch parameter, W is the width of the SLD active region, and d is the thickness of the SLD active layer.

5.3.2: Experimental butt-coupling results

The experimental and theoretical B-C efficiencies obtained from in-house fabricated S-SLDs and T-SLDs into step index SMFs and MMFs are presented. Table 5.1 describes the properties of the fibres used in the laboratory.

Table 5.1: *Properties of the step index SMF and MMF in optical coupling measurements.*

Fibre Property	SMF	MMF
Core diameter, ϕ_{CORE} (μm)	10	400
Cladding diameter (μm)	125	425
NA	0.20	0.39
Cut-off wavelength (nm)	920	-
Attenuation (dB/km)	3.5	8
Length (m)	3	3

The B-C efficiency curves measured from S-SLDs and T-SLDs coupled to a MMF (with and without index-matching gel) is plotted in Figures 5.4. The maximum and saturation B-C efficiencies, η_{max} and η_{sat}, respectively, obtained are presented in Table 5.2 for each case considered. η_{sat} is the decrease in B-C efficiency from the maximum value to the value measured at the highest injection current.

Table 5.2: *Maximum and saturation B-C efficiency (with and without index-matching gel) measured from S-SLDs and T-SLDs coupled to MMF.*

Device type	Without index-matching gel		With index-matching gel	
	η_{max}	η_{sat}	η_{max}	η_{sat}
S-SLD(25)	53.7	11.6	76.1	9.3
S-SLD(50)	50.7	8.8	83.9	10.8
S-SLD(100)	46.8	18.0	77.1	14.9
T-SLD(50)	51.2	5.8	85.8	8.5
T-SLD(100)	46.6	12.6	70.6	13.5
T-SLD(200)	38.1	12.1	59.0	8.3

The highest efficiency obtained is 85.8% measured from T-SLDs(50) with index-matching gel. However, the maximum optical power coupled to the MMF is ~750mW when AR coated T-SLDs(200) is used in conjunction with the index-matching gel.

The change in B-C efficiency is closely related to the change in FF pattern FWHM, [Chapter 4, Figure 4.16], and the maximum B-C efficiency value coincides with the minimum lateral FF FWHM value for each device. With the application of the index-matching gel 20-35% increase in B-C efficiency is typically achieved since the reflection and scattering losses are, in fact, minimised.

A schematic summarising the major sources of loss in the system is presented in Figure 5.5. The relevant losses in the B-C system are: reflection losses (α_R) at the fibre to air interfaces, scattering losses (α_{SCAT}) due to surface roughness and non uniform fibre cleave, alignment losses (α_{ALIGN}), and attenuation losses in the fibre (α_f). Therefore, the total losses in the B-C system are

$$\alpha_{tot} = \alpha_{R1} + \alpha_{SCAT1} + \alpha_{ALIGN} + \alpha_f + \alpha_{R2} + \alpha_{SCAT2} \tag{5.6}$$

where

$$\alpha_f \cong 0.03\ dB \tag{5.7}$$

$$\alpha_{R1} = \alpha_{R2} = \left(\frac{n_2 - n_0}{n_2 + n_0}\right)^2 \approx 0.18dB \tag{5.8}$$

The application of the RI matching gel reduces the losses due to α_R and α_{SCAT}.

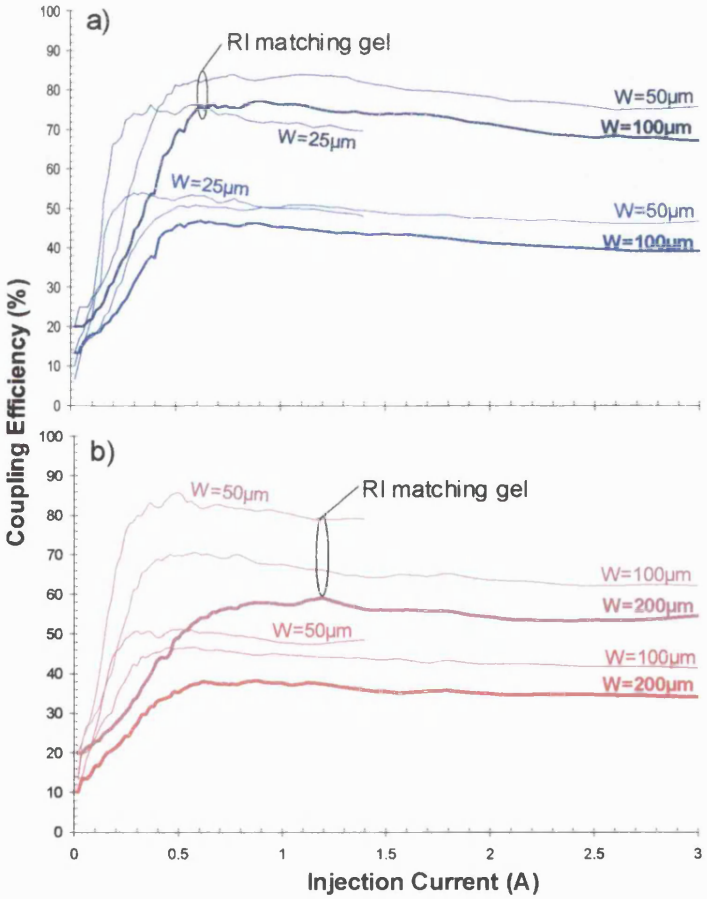

Figure 5.4: *Experimental B-C efficiency results obtained from (a) S-SLDs and (b) T-SLDs coupled to a step index MMF, with and without the application of a RI matching gel.*

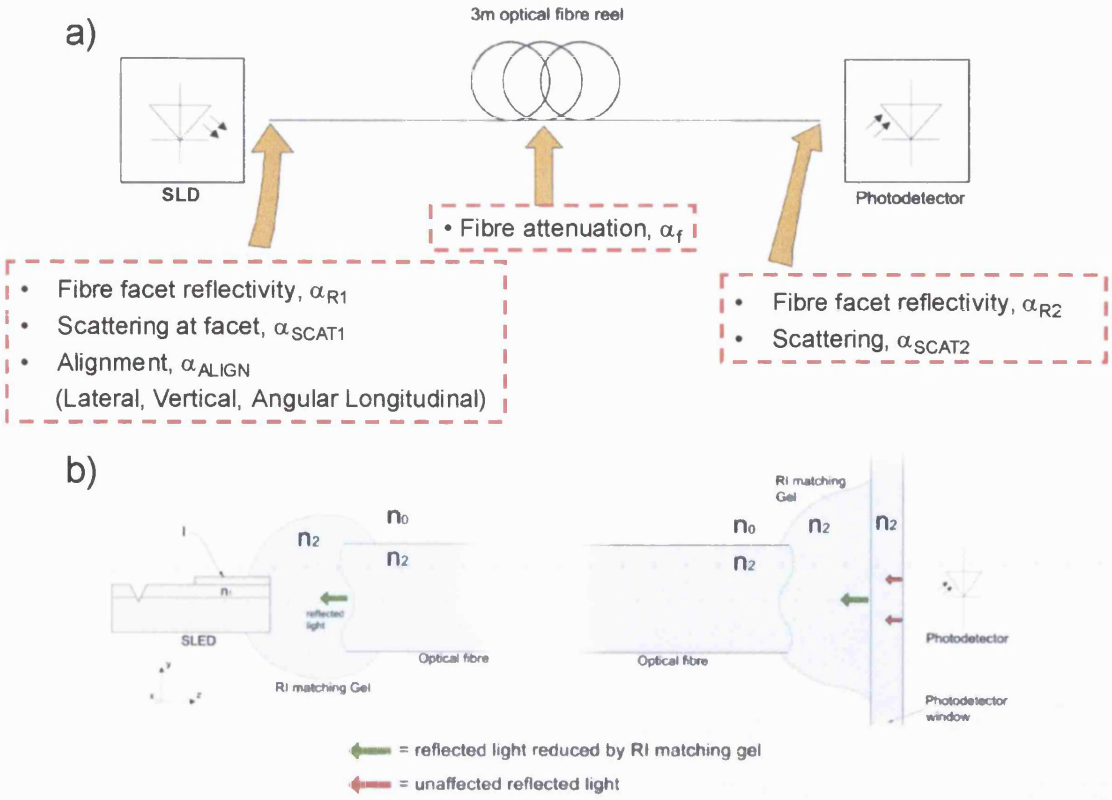

Figure 5.5: (a) *Schematic showing the losses in a B-C system:* α_R *is the reflection losses at the fibre to air interfaces,* α_{SCAT} *is the scattering losses due to surface roughness and non uniform fibre cleave,* α_{ALIGN} *is the alignment losses, and* α_f *is the attenuation losses in the fibre.*
(b) Schematic representation of B-C SLD to fibre with the application of index-matching gel. n_0, n_1, *and* n_2 *are, respectively, the refractive indices of air, SLD active layer material, and glass (and index-matching gel).*

The theoretical B-C efficiency obtained for S-SLDs and T-SLDs coupled to the MMF are compared to the experimental results in Figure 5.6. The theoretical results (which include optical saturation effects) seem to closely reproduce the trends observed in the experimental results, although slightly high efficiency values are obtained (by approximately 8%) since the system losses are not included in the model.

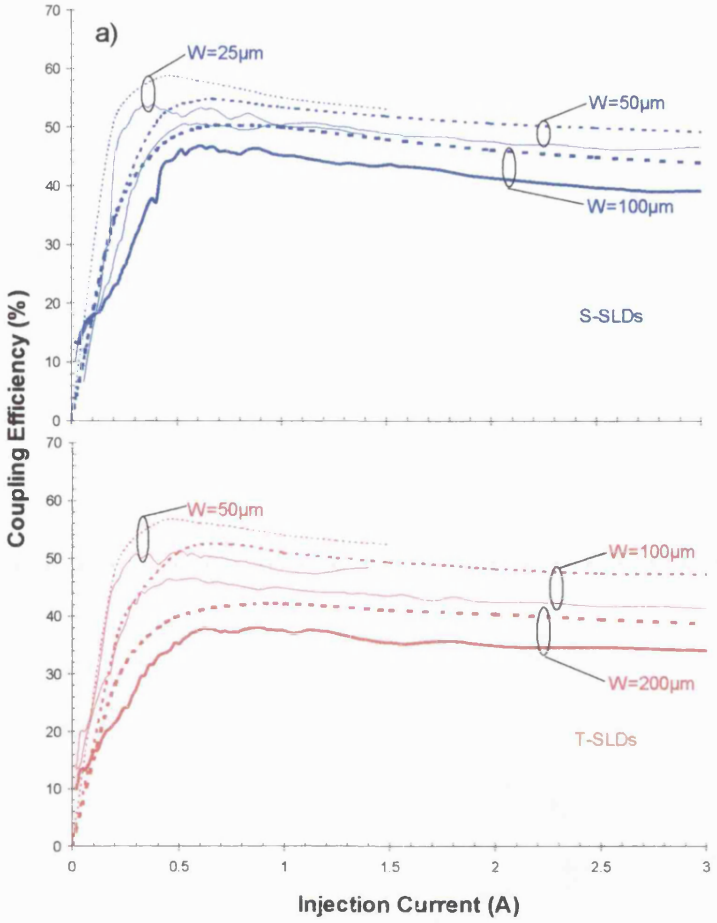

Figure 5.6: *Theoretical (dashed) and experimental (solid) B-C efficiency obtained for (a) S-SLDs and (b) T-SLDs coupled to a MMF.*

The B-C efficiency (with and without index-matching gel) and the theoretical B-C efficiency of S-SLDs coupled to SMF are plotted in Figure 5.7. The theoretical and experimental maximum B-C efficiencies are presented in Table 5.3.

Table 5.3: *Maximum experimental (with and without index-matching gel) and theoretical B-C efficiencies obtained for S-SLDs coupled to SMF.*

Device type	Experimental η_{max}	Experimental η_{max} with index-matching gel	Theoretical η_{max}
S-SLD(25)	2.2	5.6	3.9
S-SLD(50)	1.1	2.2	1.8
S-SLD(100)	0.7	1.0	1.5

The maximum power coupled to the SMF is ~7.45mW when AR coated S-SLD(100) is used in conjunction with the index-matching gel. The B-C efficiencies are much lower for SMFs than MMFs due to a smaller acceptance angle and more significantly to the core diameter to SLD width mismatch ($M=\frac{\pi\left(\frac{\varphi_{CORE}}{2}\right)^2}{Wd}$, since $\phi_{CORE} << W$).

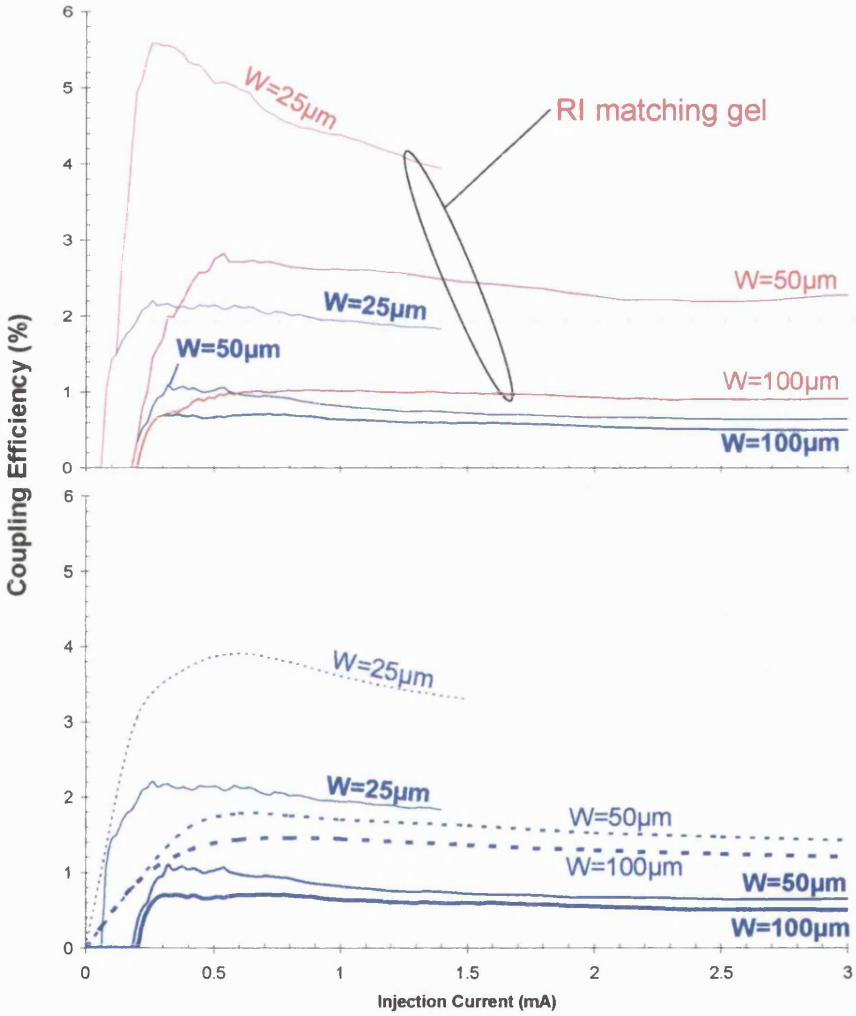

Figure 5.7: *The B-C efficiency with (red line) and without (blue line) index-matching gel and corresponding theoretical results (dashed line) obtained for S-SLD - to - SMF butt-coupling.*

The lateral (x) and vertical (y) normalised coupling efficiencies for S-SLD to optical fibre (MMF and SMF) misalignment, [5-8], are plotted in Figure 5.8. S-SLD(50) is used in this case. For the MMF there is no significant vertical or lateral misalignment loss until the S-SLD approaches the edge of the fibre core. The alignment tolerance in SLD-to-MMF butt-coupling is high compared with that associated with the SMF. Light is coupled from the SLD to the SMF only if the fibre remains within the dimensions of the emitting area of the SLD facet. Therefore, as expected, the vertical alignment tolerance

in this case is particularly small (3μm). Similar trends have been observed with SLDs of different geometries.

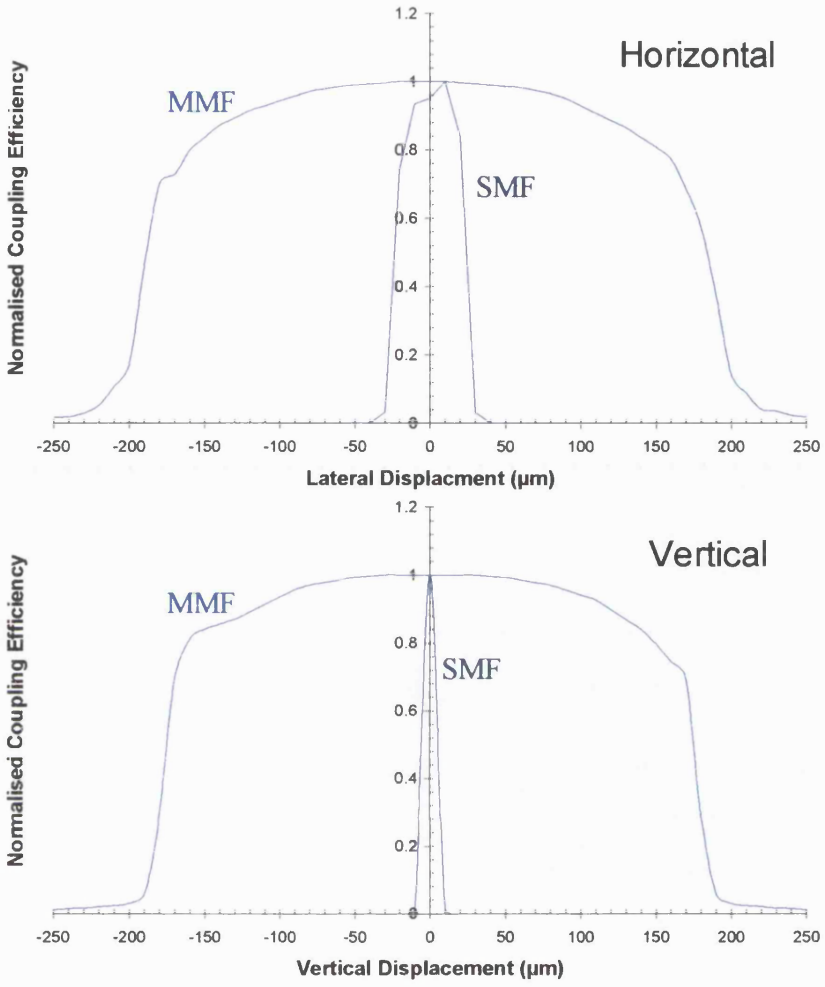

Figure 5.8: *The lateral (x) and vertical (y) normalised coupling efficiencies for S-SLD to optical fibre misalignment.*

5.4 System of lenses coupling to SMF

To increase the efficiency of optical source to SMF coupling a system of lenses is used. The system of lenses coupling technique captures and focuses the light emitted from an optical source into an optical fibre. With this technique aberrations that are inherent to the source (such as astigmatism) can be corrected before coupling to the fibre. The beam emitted from SLDs does not (usually) have a 1:1 aspect ratio. The vertical FWHM beam width is typically larger than the lateral FWHM. On the other hand, for wide SLDs (e.g., S-SLD(100) and T-SLD(200)) the reverse occurs. Therefore it is possible to design the SLD to achieve equal vertical and lateral FWHM (e.g., S-

SLD(100), Chapter 4: Figure 4.16). The system of lenses technique described here is designed to correct the beam astigmatism so that a spot close to 1:1 aspect ratio is achieved.

A triple-lens configuration is used to couple light into a SMF, Figure 5.9. An aspheric lens is positioned close to the source to capture the emitted beam and collimate the fast (y) axis. A cylindrical lens is used to collimate the slow (x) axis to achieve a circular spot. The resulting collimated beam is then focussed into the SMF using another aspheric lens. The position of each lens must be centred on an alignment axis that originates from the SLD facet normal and ends at the fibre facet normal.

The optical properties of the lenses used in the measurements are described in Table 5.4. The lens selection is based on a simple ray tracing approach recommended by most optics catalogues.

Table 5.4: *Optical properties of the lenses used in the coupling system of Figure 5.11.*

Lens type	**Focal length (mm)**	**Diameter (mm)** - Aspheric **Width** × **Height (mm)** - cylindrical	**NA**
Aspheric1 (collimating)	12.0	12.0	0.44
Cylindrical	25.0	10.0 × 25.0	0.20
Aspheric2 (focussing)	33.0	52.0	0.62

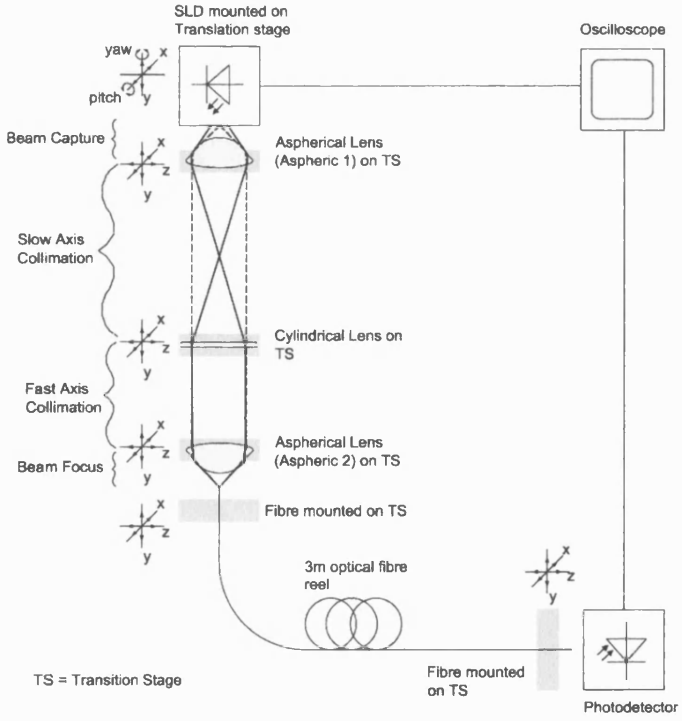

Figure 5.9: *Schematic showing the equipment and lens system used for SLD- to-SMF coupling.*

5.4.1 Experimental system of lenses coupling results

The coupling efficiency and coupled power of S-SLDs and T-SLDs into a SMF using the triple-lens system are plotted in Figure 5.10. The maximum coupling efficiencies and coupled power at I=3A obtained using S-SLDs and T-SLDs are presented in Table 5.5.

Table 5.5: *Maximum coupling efficiencies and coupled power at I=3A measured from S-SLDs and T-SLDs - to - SMF coupling using lenses.*

Device type	η_{max}	Coupled Power at I=3A (mW)
S-SLD(25)	23.3	7.3 (at I=1A)
S-SLD(50)	21.5	20.9
S-SLD(100)	18.7	23.0
T-SLD(50)	20.9	11.7 (at I=1A)
T-SLD(100)	19.2	39.2
T-SLD(200)	17.1	42.0

The variation in coupling efficiencies between the devices is 6% with the S-SLDs being more efficient than the corresponding T-SLD with the same active volume. S-SLDs have a narrower lateral beam width than the corresponding T-SLDs resulting in better coupling to the collimating aspheric lens. The maximum power coupled into the SMF is 42mW achieved using a T-SLD(200). The coupling efficiency is half the value of the efficiencies found in literature for similar devices, [5-9], and this is attributed to the precision of the equipment used and the quality of the lenses (e.g., the lenses are not AR coating). The power coupled into the fibre using the system of lenses technique is not significantly affected by optical saturation since the limits imposed by the NA of the system are more restrictive.

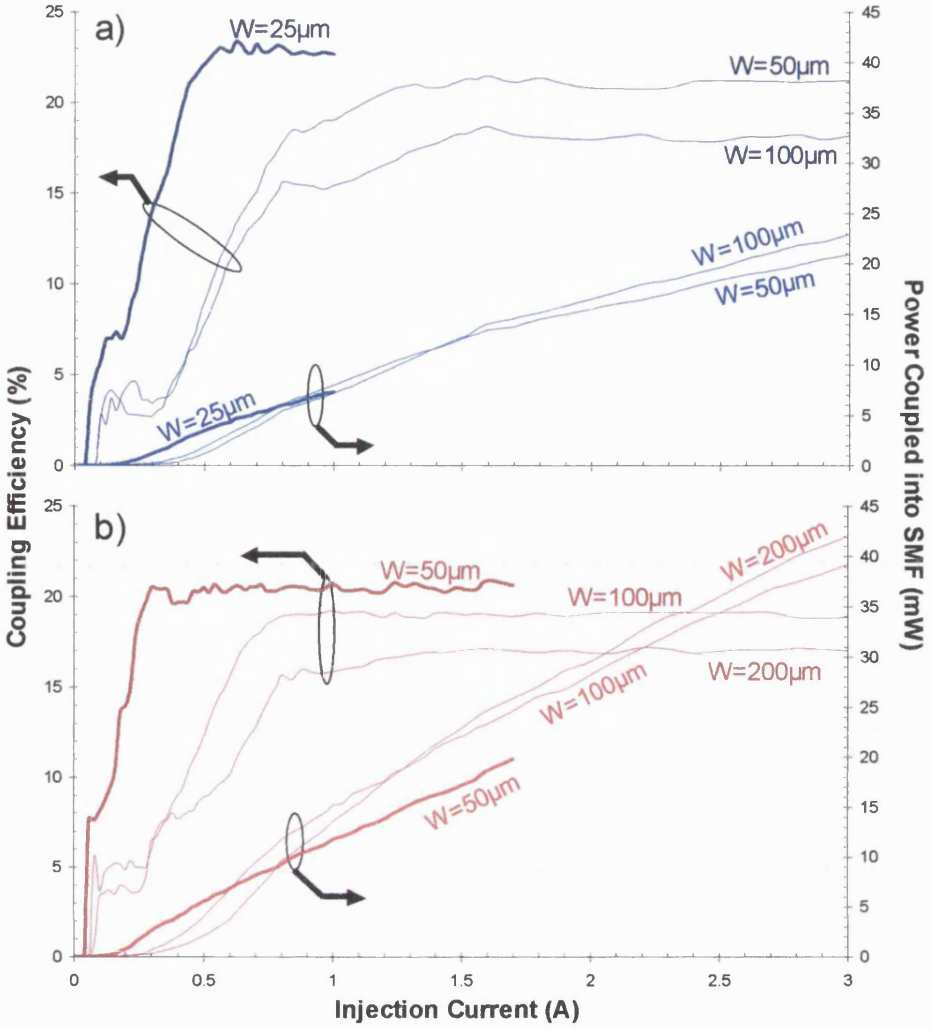

Figure 5.10: *Coupling efficiency and coupled power of (a) S-SLDs and (b) T-SLDs into a SMF using the triple-lens system.*

Coupling losses associated with the system of lenses technique are attributed to beam truncation (from Aspheric1), reflections from the lenses and the fibre, misalignment, lens imperfections, [5-10], and non-optimal focal length for the cylindrical lens. In fact, using a cylindrical lens with optimal focal length it is possible to achieve a collimated circular beam. However, one cylindrical lens is not sufficient to circularise the output beam of all devices considered in this thesis. Coupling losses were measured at various points in the system, Figure 5.11 and Table 5.6. The majority of the coupling losses occur in section C of the system where alignment of the fibre to the focussed spot occurs.

Table 5.6: *Losses estimated at different points in the lens system at currents above material transparency.*

Device name	Section A (%)	Section B (%)	Section C (%)	Total (%)
S-SLD(25)	5.1	20.5	51.1	76.7
S-SLD(50)	5.9	23.2	49.4	78.5
S-SLD(100)	6.7	21.4	53.2	81.3
T-SLD(50)	5.4	22.8	50.9	79.1
T-SLD(100)	6.3	21.6	52.9	80.8
T-SLD(200)	8.1	22.5	52.3	82.9

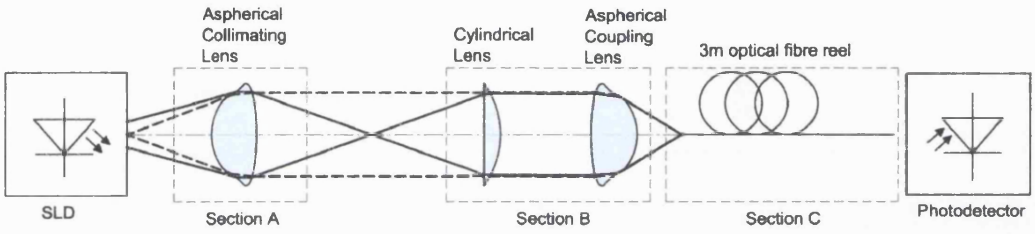

Figure 5.11: *Schematic showing the points from which losses in the lens coupling system were measured.*

5.5: Summary

In this Chapter two methods for coupling SLDs to optical fibres have been described, namely butt-coupling and system of lenses coupling. The efficiency of coupling S-SLDs and T-SLDs to SMFs and MMFs and corresponding losses were measured. For the B-C technique, a method of using the model described in Chapter 3 to compute the coupling efficiency is presented.

The B-C technique was shown to be suited for coupling SLDs to MMFs with 85.8% coupling efficiency measured using T-SLD(50) with index-matching gel. The maximum power coupled into MMFs was estimated to be 750mW for an AR coated T-SLD(200). A reduction in B-C efficiency was observed for increasing currents which was attributed to optical gain saturation.

The system of lenses technique is suitable for coupling SLDs to SMFs. The maximum coupling efficiency and estimated power coupled to a SMF was measured to be 23.3%, using S-SLD(25), and 42mW, using T-SLD(200), respectively.

References

[5-1] Shaw N., Williams P.J., and Buus J., *Optoelectronic integrated circuit (OEIC) waveguide coupler for spot size expansion and improved fibre coupling efficiency*, Electronics Letters, Vol. 31, No. 14, July 1995, pp. 1143-1145.

[5-2] Kuwahara, H., Sasaki M., and Tokoyo N., *Efficiecnt coupling from semiconductor lasers into single-mode fibers with tapered hemispherical ends*, Applied Optics, Vol. 19, No. 15, August 1980, pp. 2578-2583.

[5-3] Yamada J.-I., Murakami Y., Sakai J.-I., and Kimura T., *Characteristics of a Hemispherical Microlens for Coupling Between a Semiconductir Laser and Single-Mode Fiber*, IEEE Journal of Quantum Electronics, Vol. QE-16, No. 10, October 1980, pp. 1067-1072.

[5-4] Clark T., and Wanser K., *Ball vs. Gradient Index Lenses*, Photonics spectra, February 2001, pp. 94-96.

[5-5] Yeh S.-M., Huang S.-Y., and Cheng W.-H., *A New Scheme of Conical-Wedge-Shaped Fiber Endface for Coupling Between High-Power Laser Diodes and Single-Mode Fibers*, Journal of Lightwave Technology, Vol.23, No. 4, April 2005, pp. 1781-1786.

[5-6] Goldberg L., and Mehuys D., *High power superluminescent diode source*, Electronics Letters, Vol.30, No. 20, September 1994, pp. 1682-1684.

[5-7] Etten W.-V., and Plaats J.-V.-D, *Fundamentals of Optical Fiber Communication*, Prentice Hall International (UK) Ltd, London, 1991

[5-8] Tang Z., Zhang R., Mondal S.K., and Shi F.G., *Optimization of fiber-optic coupling and alignment tolerance for coupling between a laser diode and a wedged single-mode fiber*, Optics Communications, Vol. 199, November 2001, pp. 95-101.

[5-9] Livas J.C., Chinn S.R., Kintzer E.S., Walpole J.N., Wang C.A., and Missaggia L.J., *Single-Mode Optical Fiber Coupling of High-Power Tapered Gain Region Devices*, IEEE Photonics Technology Letters, Vol. 6., No. 3, March 1994, pp. 422-424.

[5-10] Hillerich B., *Influence of Lens Imperfections with LD and LED to Single-Mode Fiber Coupling*, Journal of Lightwave Technology, Vol. 7, No. 1, January 1989, pp. 77-86.

Chapter 6
Development of New SLD Designs

6.1: Introduction

This Chapter presents the in-house design and development of two novel geometry SLDs. The first is an array of n (n=3, 4, 5) T-SLDs. The second is a SLD with segmented contact composed of a tapered injection contact and a long stripe parallel to the output facet. The justification for the design and development of new SLD geometries will be discussed in detail in this Chapter. Photographic documentation of in-house fabricated prototypes of both devices is presented in Appendix I.

The development of the T-SLD Array (T-SLDA) is presented in Section 6.2. The LI characteristic, W-P efficiency, FF pattern and NF intensity profile of the array are presented and compared to the characteristics of an individual T-SLD. The model described in Chapter 3 is used to compute the FF pattern and NF intensity profile of the T-SLDA for comparison with the experimental results.

The segmented contact geometry, referred to as a *'Hammer-Head'* SLD (HH-SLD), is presented in Section 6.3. The novel (linear) LI characteristic of the HH-SLD is presented together with an analysis of the FF pattern and spectral distribution.

6.2: T-SLD Arrays

The T-SLD array has been designed to increase SLD output power without changing the output beam properties, for example to increase broadband optical power coupled to a MMF for applications including short-haul WDM communication systems, e.g., [6-1], or solid-state lighting, e.g., [6-2].

The schematic of the T-SLDA is presented in Figure 6.1. To prevent cross-talk (and, therefore, additional optical gain saturation) longitudinal v-groove deflectors have been included between the array elements in addition to the rear v-groove deflector essential to suppress lasing for each individual element in the array. The relevant device dimensions are presented in Table 6.1 for a n-T-SLDA.

Table 6.1: *Device dimensions for a n-T-SLDA.*

Description	Symbol	Value (μm)
Taper Length	L	1000
Taper width at output facet	W_T	100
Deflector length	L_{DEF}	900
Distance between rear deflector and taper	D	200
T-SLDA output facet width	W_{ARR}	$n \times W_T$

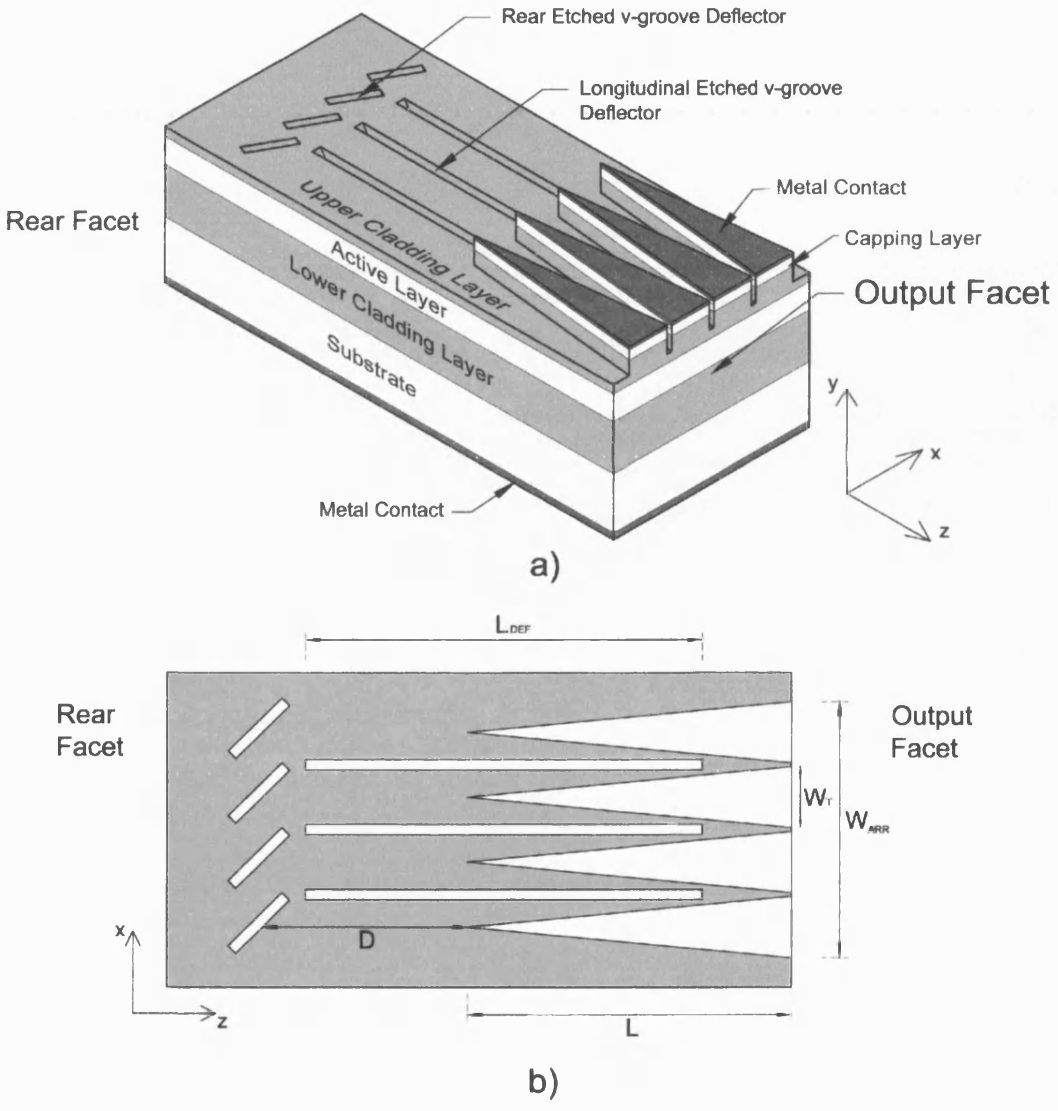

Figure 6.1: *(a) Schematic representation of a 4-T-SLDA. (b) Top view of the 4-T-SLDA.*

6.2.1: VI and LI characteristics

The VI characteristics of T-SLDA of 3, 4 and 5 elements are compared with that of an individual T-SLD in Figure 6.2. The device series resistance, R_S, [Chapter 4], increases with the number of elements in the array, Table 6.2. The increase in R_S is attributed to the sheet resistance of the p- contact (titanium and gold), which depends on the contact area, [6-3].

Table 6.2: *Series resistance for different element T-SLDA.*

Device type	R_S (Ω)
3 T-SLDA	0.71
4 T-SLDA	0.74
5 T-SLDA	0.76

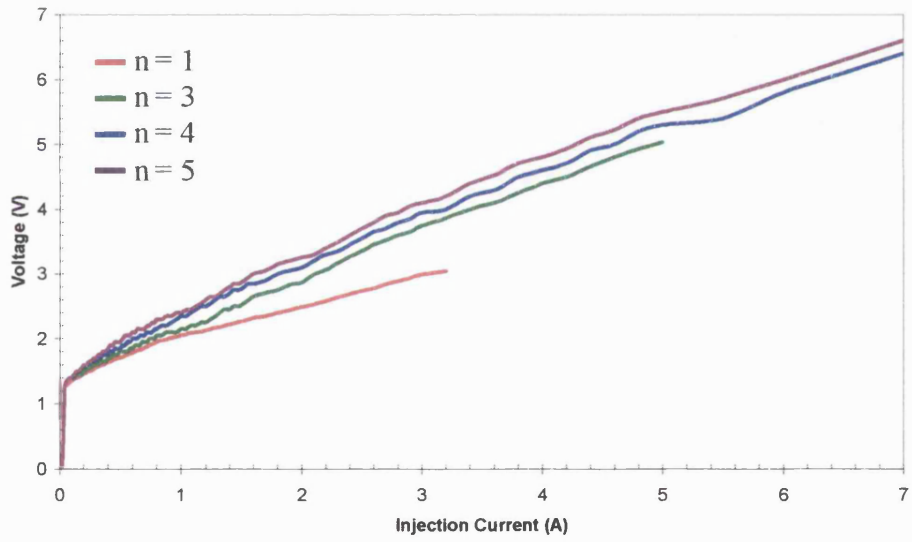

Figure 6.2: *Experimental VI characteristic measured from uncoated T-SLDAs of n elements (n=1, 3, 4, 5).*

The experimental LI characteristics and W-P efficiency curves measured from uncoated T-SLDAs with n-elements (n=3, 4, 5) are compared to those measured from T-SLD(100) (corresponding to n=1) in Figure 6.3. The maximum output power is 500mW for the 5-T-SLDA at I=7A. The peak W-P efficiency is significantly lower for T-SLDAs of a larger number of elements since the corresponding operating voltage increases

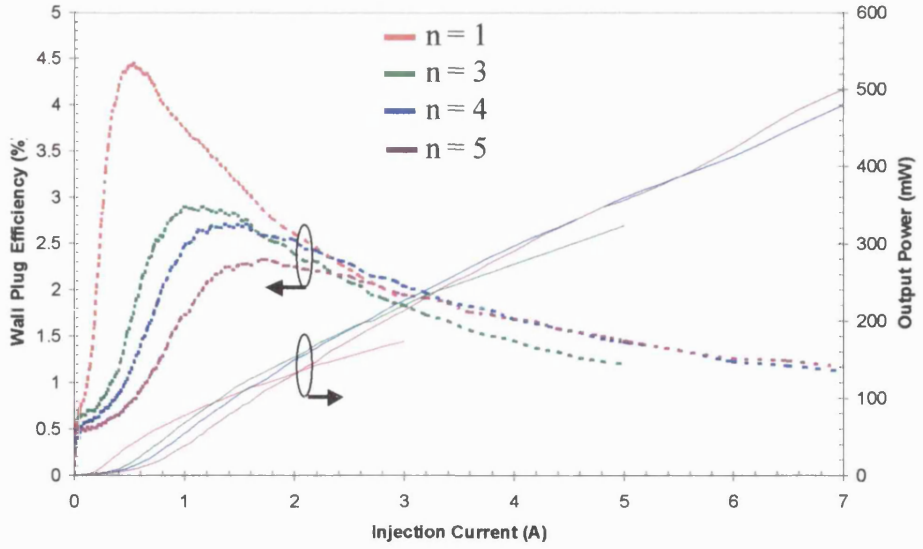

Figure 6.3: *Experimental W-P efficiency (dashed) and LI characteristics (solid) measured from T-SLDAs of different number of n elements (n=1, 3, 4, 5).*

For a meaningful comparison of the output power measured from T-SLDAs of different number (n) elements it is necessary to consider L-J curves, that is the output optical power with respect to injection current density (J) characteristics, Figure 6.4. Theoretical results obtained by summing the output power of n individual SLDs of the same type are also presented in Figure 6.4 for comparison. The output power of the n-element T-SLDAs is the same as that expected from n separate T-SLDs.

After AR coating as expected, [6-4], a five-fold increase in output (optical) power is observed, Figure 6.5, with corresponding increase in W-P efficiency. The reflectivity of the AR coating has been estimated with the ray model; the relevant operational characteristic parameters are summarised in Table 6.3. The measured output power is in excess of 2.7W from the 4-T-SLDA at (I=7A); at present this is the highest optical power reported from a SLD. The output power measured from the 5-T-SLDA is lower than expected due to a relatively poor AR coating.

Table 6.3: *Maximum W-P efficiency and output power of T-SLDAs including the estimated output facet reflectivities.*

Device type	Estimated Reflectivity (%)	Peak W-P Efficiency (%)	Output power (W)
3-T-SLDA	0.9	10.86	1.8
4-T-SLDA	0.8	9.96	2.7
5-T-SLDA	1.4	7.89	2.5

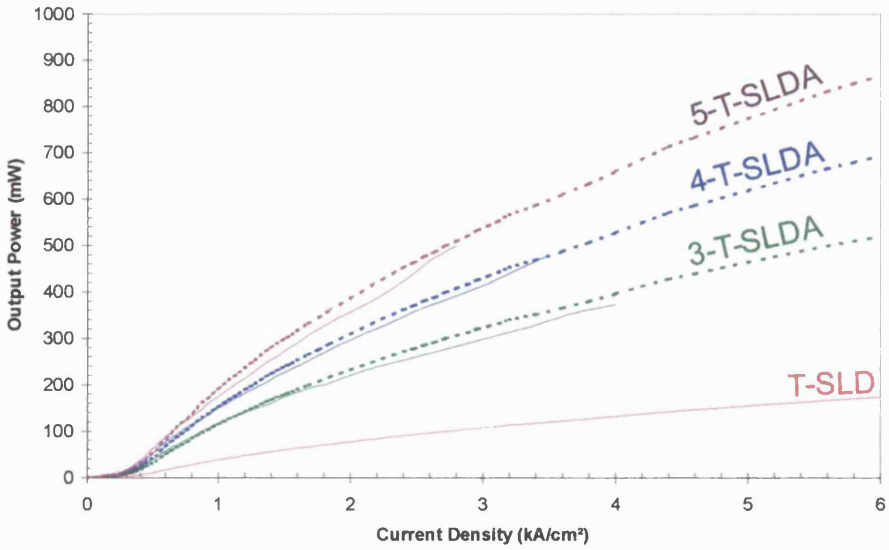

Figure 6.4: *Output power against current density measured from T-SLDAs of different number (n) of elements (n=1, 3, 4, 5). Theoretical results (dashed lines) are also plotted for comparison.*

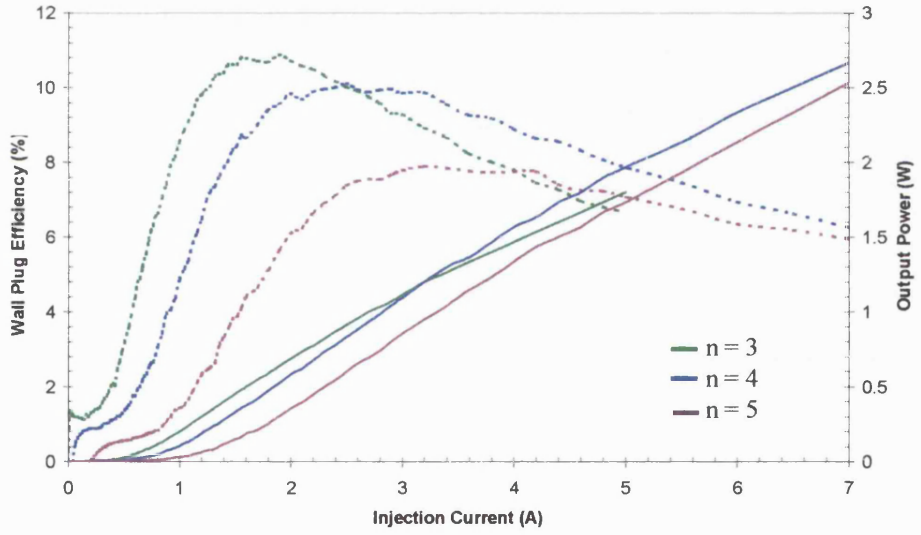

Figure 6.5: *Experimental W-P efficiency (dashed) and LI characteristic (solid) measured from AR coated T-SLDAs (n=3, 4, 5).*

6.2.2: Far field characteristics

The FF pattern measured from T-SLDAs at J=3kAcm^{-2} are plotted in Figure 6.6. As expected, the far field characteristics do not change with respect to those of the individual T-SLD. The lateral FF FWHM is approximately 30° for all devices. The only minor difference is in the slightly more prominent *'tail'* of the field observed in T-SLDAs.

This effect is attributed to rays travelling at wide angles in the region without longitudinal deflectors thereby crossing regions with gain before diffracting at the output facet. To verify the above statement T-SLDAs with 10μm separation between the output facets of the individual T-SLDs have been fabricated and characterised. As observed from Figure 6.6 the *'tails'* in this case become less prominent because the unpumped regions between the T-SLDs attenuate rays travelling at wide angles.

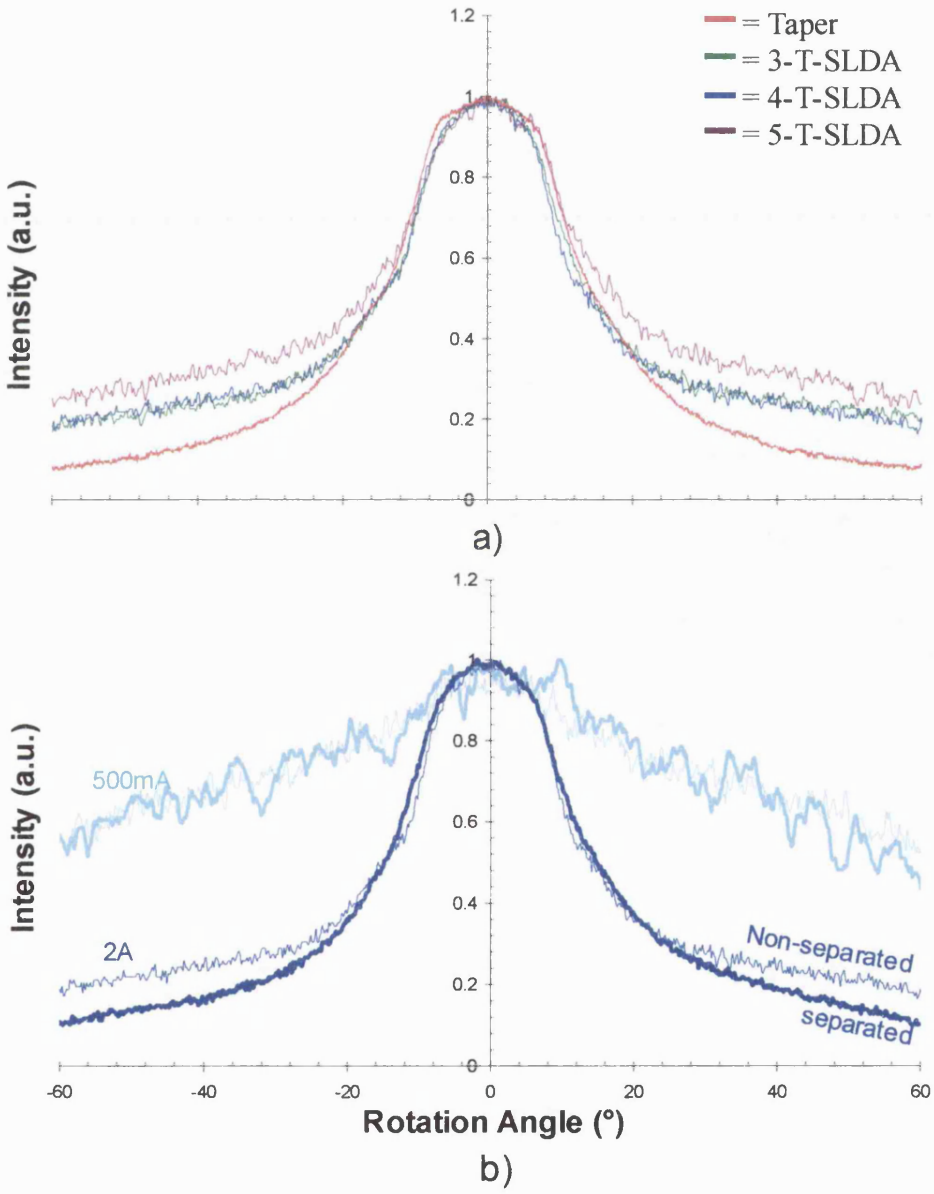

Figure 6.6: (a) Lateral *FF patterns measured from T-SLDAs (n=1, 3, 4, 5) at J=3kAcm^{-2}. (b) 4-T-SLDAs with and without separation between individual T-SLDs at various injection currents.*

Theoretical near and far field profiles obtained from the in-house developed ray model reproduce very closely the experimental curves for all devices. As a representative example, the experimental and theoretical lateral FF pattern obtained from 4-T-SLDAs at different injection currents are plotted in Figure 6.7.

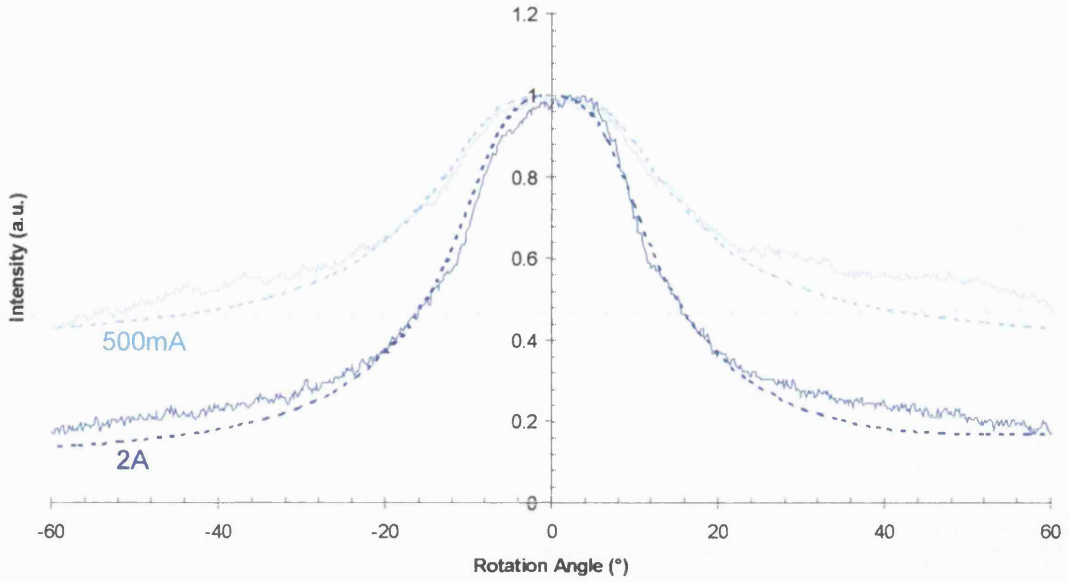

Figure 6.7: *Theoretical (dashed) and experimental (solid) lateral FF pattern of a 4 T-SLD array.*

6.2.3: Near field intensity profiles

The experimental NF intensity profiles measured from T-SLDAs (n=3, 4, 5) at different current densities are presented in Figure 6.8. The near fields observed from arrays of T-SLDs show that the individual elements are operating independently. The near field intensity profile of an individual T-SLD matches perfectly with those of the array elements, as shown in Figure 6.8. In addition, the peaks of the intensity profiles are at the same level for all arrays indicating a uniform distribution of carriers across the array. The theoretical results obtained from the model closely match the experimental profiles, as shown in Figure 6.9.

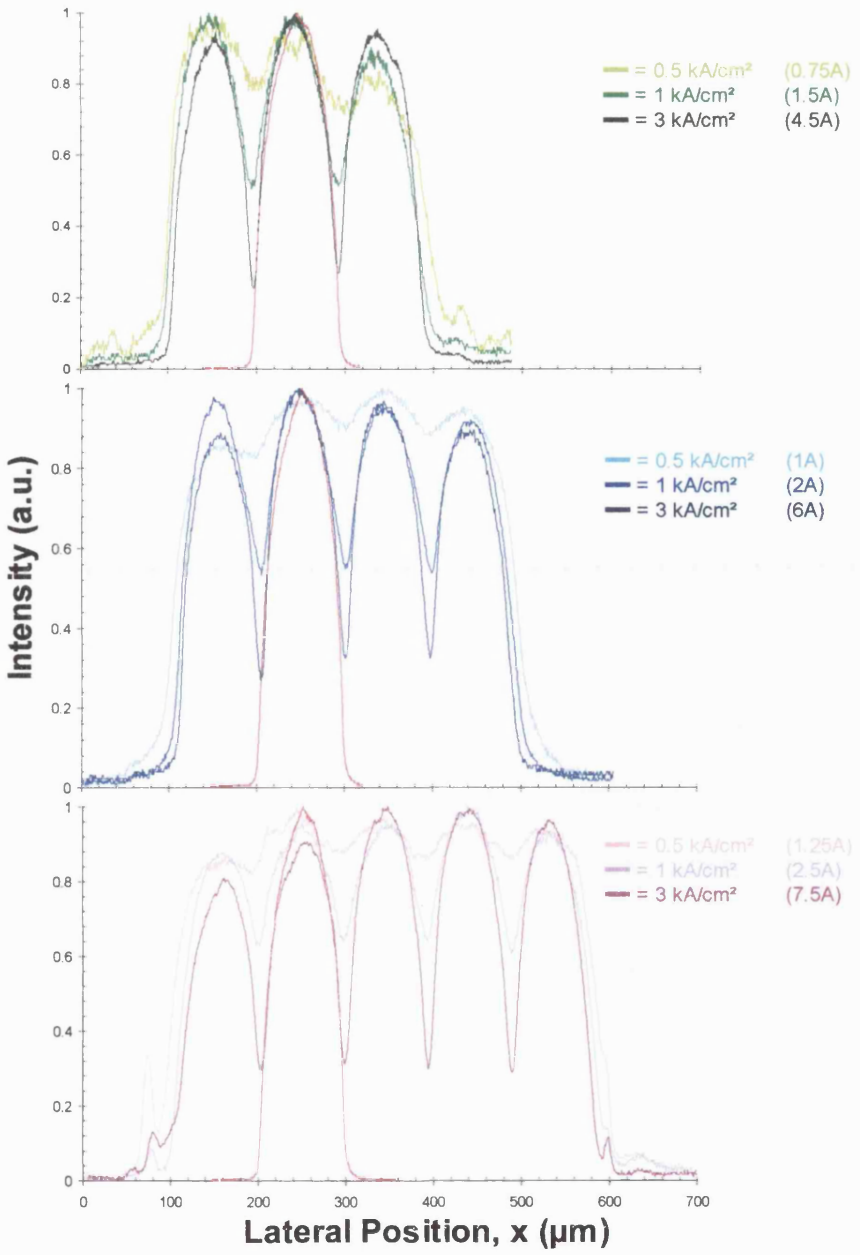

Figure 6.8: *NF intensity profiles observed from T-SLDAs at different current densities. The NF profile obtained from an individual T-SLD(100) (red) is included for comparison.*

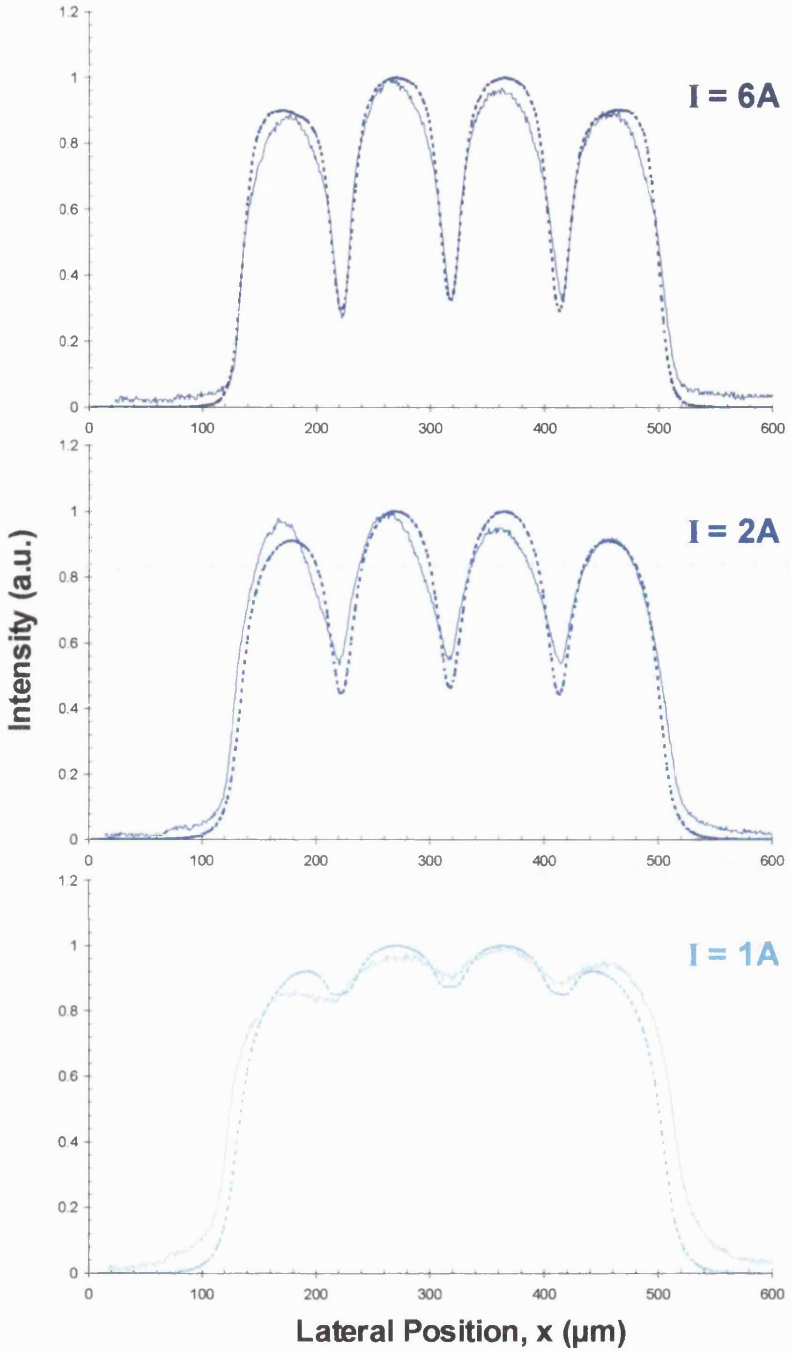

Figure 6.9: *Theoretical (dashed) and experimental (solid) NF intensity profiles obtained for 4-T-SLDAs at different injection currents.*

6.2.4: Spectral characteristics

Spectra obtained from 4-T-SLDAs are compared with the curves obtained from individual T-SLDs(100) at J=3kAcm^{-2} in Figure 6.10. No modulation is added to the spectral curves as a result of the array structure.

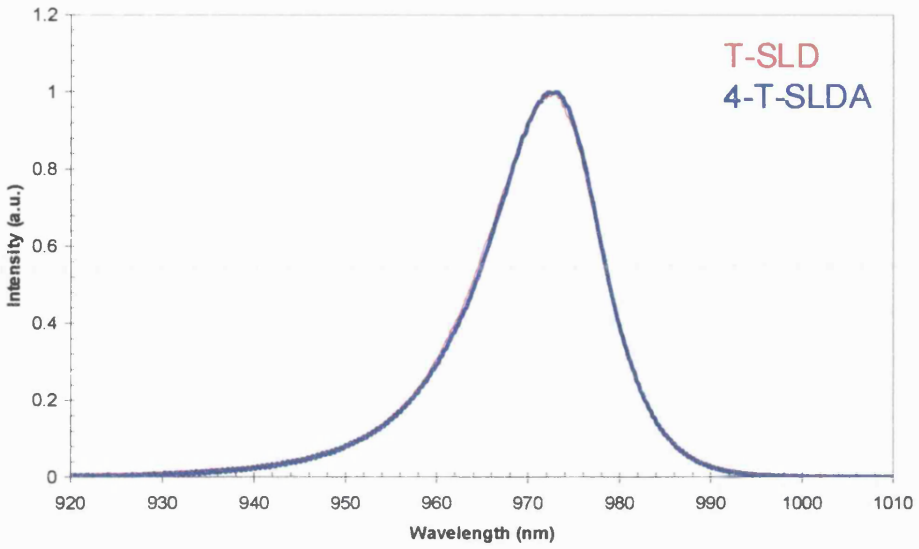

Figure 6.10: *Spectra curves obtained from 4-T-SLDAs and T-SLD(100) at J=3kAcm^{-2}.*

6.3: Hammer-head SLDs

The segmented HH-SLD has been designed to produce linear power-current characteristics for applications including, for example amplitude modulation.

The contact geometry is segmented into two sections: a Wide Stripe (WS), and a tapered section, Figure 6.11. The two contacts are separated by a 40μm deeply etched (~1.0μm) region to avoid short-circuiting and reduce current flow between the contacts. The resistance between the contacts is 90Ω which is high compared to the device series resistance (approximately 0.7Ω). Etched v-groove deflectors are positioned either side of the WS to prevent feedback from the cleaved edges. Etched deflectors are also positioned at the rear of the taper and the WS section to suppress optical feedback into the gain region. Current is injected independently into each of the contacts. Device dimensions for the HH-SLD are presented in Table 6.4.

The WS section is designed to increase the optical output power at low injection currents (spontaneous emission, non-positive optical gain). The WS section has operational characteristics similar to those of a surface emitting LED, [6-5], Figure 6.12. The LI characteristic measured from the taper section alone (WS section not contacted) is also plotted in Figure 6.12. The output power from the taper section is lower than that expected from a typical T-SLD of corresponding dimensions, [Chapter 4, Figure 4.3], because the unpumped WS section acts as an absorption region.

The LI characteristic obtained from HH-SLD by adjusting the currents in the two injection contacts is plotted in Figure 6.13. The percentage of total injection current supplied to each contact is also presented for clarity. The LI characteristic is linear with a slope efficiency of 0.04 WA^{-1} with a 2.8% maximum W-P efficiency, Figure 6.14. For I<250mA, current is supplied only to the WS section. With the on-set of superluminescence in the WS section the current supplied to the taper section is increased gradually to prevent the super-linear characteristic of ASE and maintain the HH-SLD LI curve linearity. The sublinear characteristic in SLDs caused by optical gain saturation is in fact removed by careful control of the relative currents supplied to each contact.

Table 6.4: *Device dimensions for a HH-SLD.*

Description	Symbol	Value (μm)
HH-SLD length	L	1000
Taper width at output facet	W_T	200
Length of wide stripe	L_{WS}	100
Width of wide stripe	W_{WS}	1000
Distance between rear deflector and taper	D_1	200
Distance between rear deflector and wide stripe	D_2	800
Distance between lateral deflector and wide stripe	D_3	200

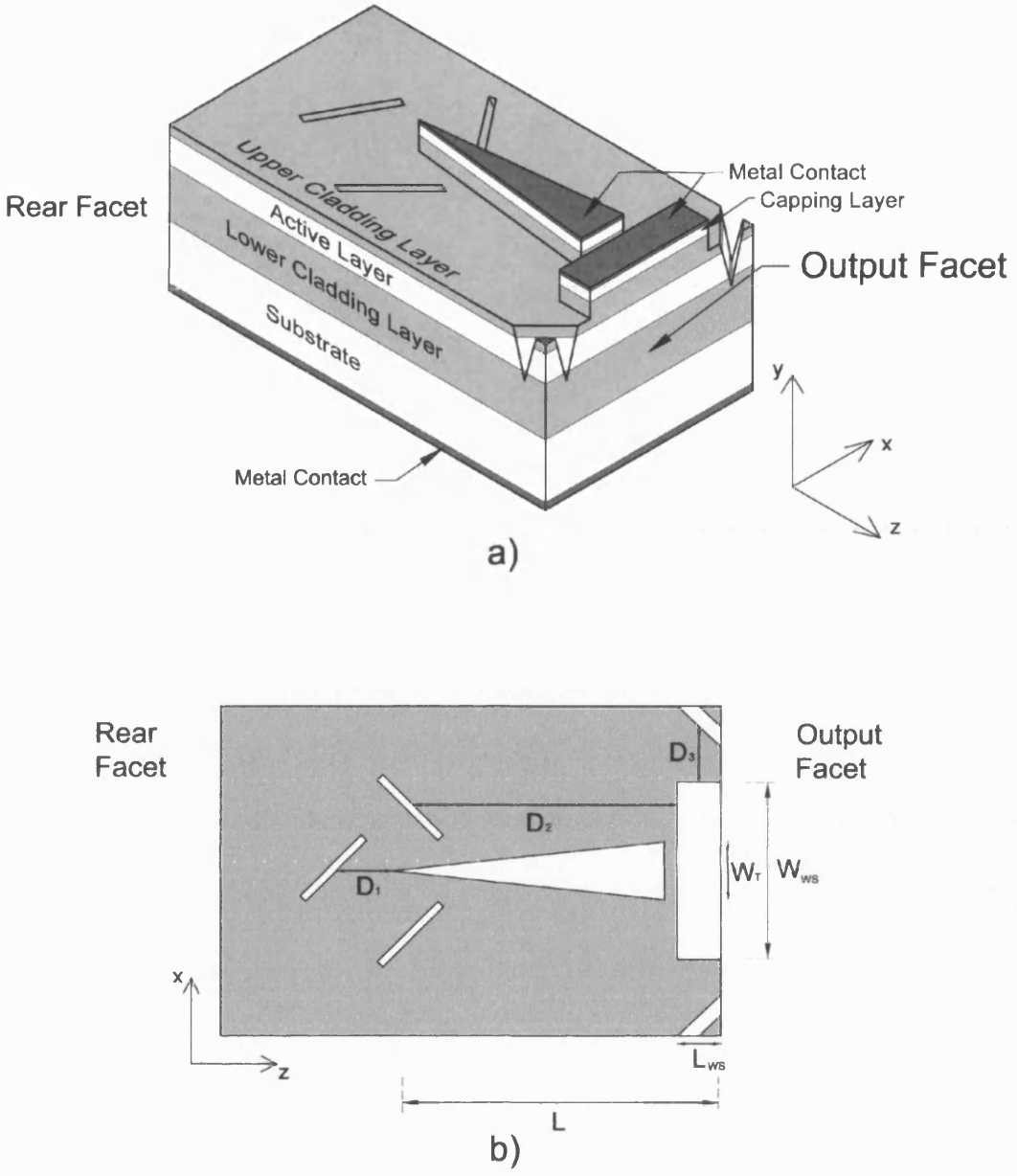

Figure 6.11: (a) *Schematic representation of an in-house designed and developed HH-SLD. (b) Top view of the HH-SLD.*

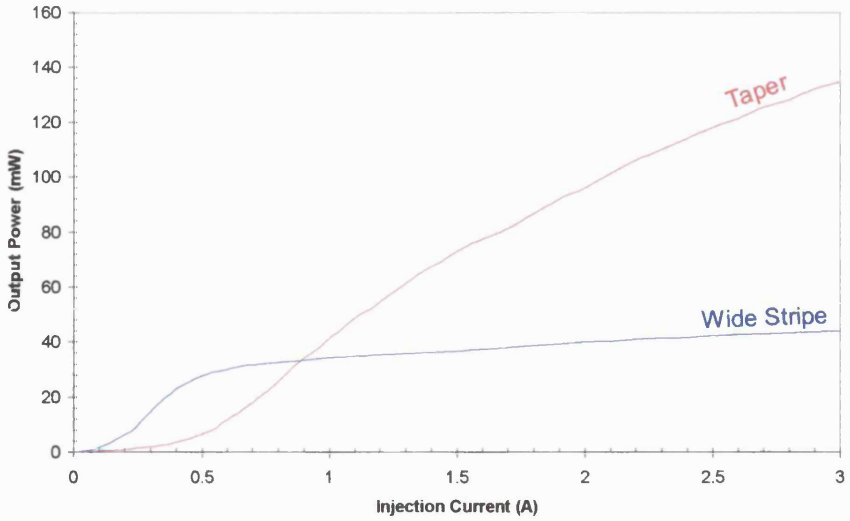

Figure 6.12: *Experimental LI characteristic obtained from the WS section and tapered section of a HH-SLD.*

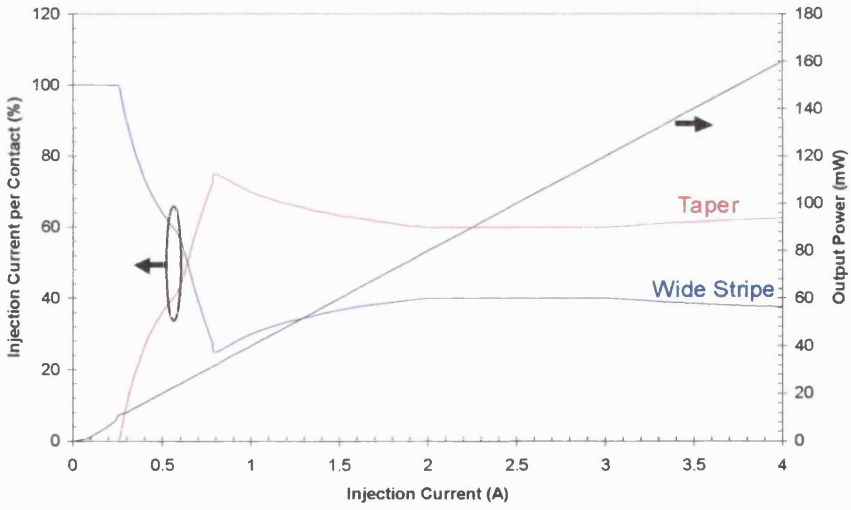

Figure 6.13: *Experimental LI characteristic obtained from a HH-SLD. The percentage of total injection current supplied to each contact is also plotted.*

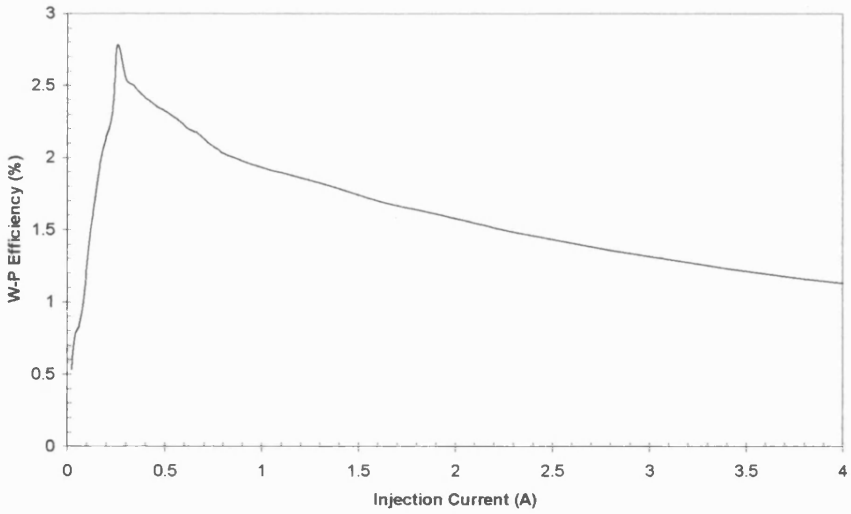

Figure 6.14: *Experimental W-P efficiency measured from a HH-SLD.*

The lateral FF pattern of the HH-SLD is presented in Figure 6.15 for various injection currents. The lateral FF patterns resulting from individual pumping of the WS and the tapered sections are also included for clarity and completeness. The FF pattern obtained from the WS section alone is a close approximation to the Lambertian profile (cos θ) expected from typical surface emitting LEDs, [6-5], inset of Figure 6.15(b). The FF pattern of the taper section is not similar to that of a T-SLD, Figure 4.15. This is attributed to the absorption region provided by the unpumped WS section affecting the FF pattern.

The FF pattern produced by combined pumping of the WS section and taper section at I=4A is similar to the FF pattern of a T-SLD. The light intensity produced by the taper section, no longer affected by an unpumped absorption region, dominates the HH-SLD FF pattern.

The normalised spectral distribution and coherence curve obtained from HH-SLDs at different injection currents are compared in Figures 6.16 and 6.17, respectively. At I=4A the coherence length of HH-SLDs is L_C=48.1μm similar to that achieved for T-SLDs fabricated from the same QW material, [Chapter 4]. The spectral distribution does not present significant modulation. The coherency curves show that there are no significant residual coherence peaks caused by the RI step provided by the deep etch between the contacts.

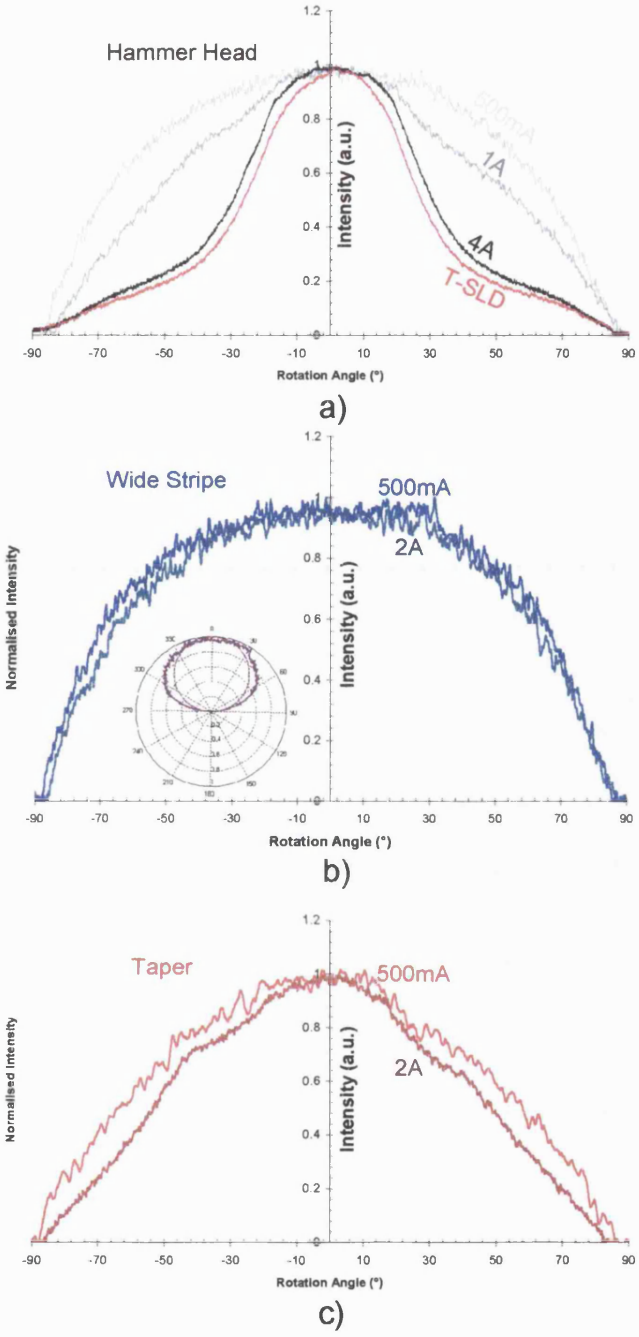

Figure 6.15: a) *Experimental FF pattern obtained from a HH-SLD (grey) at various injection currents. The FF pattern measured from T-SLDs(100) at I=2A is included for comparison (red). b) Experimental FF pattern of the WS section when contacted separately (blue) at various injection currents. The inset compares the FF radiation pattern for the WS section (solid) to the Lambertian profile (dashed). c) Experimental FF pattern of the taper section when contacted separately (red) at various injection currents.*

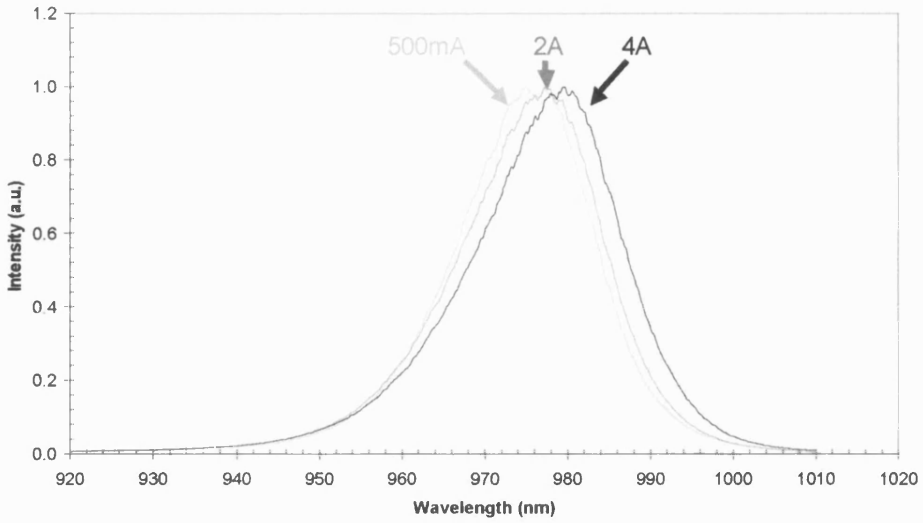

Figure **6.16:** *Spectral distribution of a HH-SLD for various injection currents.*

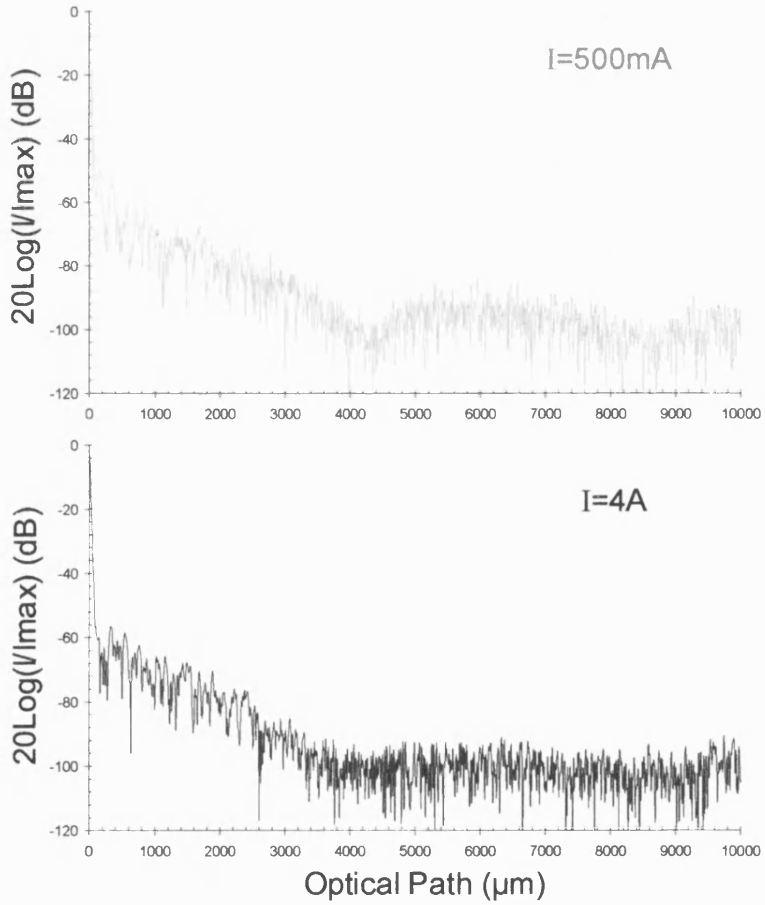

Figure 6.17: *Coherence curves of a HH-SLD at I=500mA and 4A.*

6.4: Summary

In this Chapter two novel geometry SLDs have been introduced, namely the T-SLD array and the HH-SLD. Both the T-SLD and HH-SLD have been characterised and the results compared to T-SLD characteristics. Theoretical results for the T-SLD array NF intensity profile and FF pattern were also presented.

The maximum output power measured from an AR coated T-SLD array was 2.7W and is the highest power obtained from a SLD. The output power from an n-element T-SLD array was found to be equivalent to the power obtained from n separate T-SLDs. The FF FWHM for the T-SLD arrays was measured to be the same as the FWHM of a T-SLD. Excellent agreement between theoretical and experimental results was achieved.

The novel linear LI characteristic obtained from (segmented contact) HH-SLDs was presented. The characteristic was achieved by carefully controlling the percentage of total injection current supplied to each contact. The slope efficiency of the LI characteristic was measured to be a constant $0.04WA^{-1}$ up to 4A driving current with a 2.8% maximum W-P efficiency at I=0.25A. At low injection currents the lateral FF pattern of the HH-SLD was similar to a Lambertian profile commonly found for surface emitting LEDs. At high injection currents the FF pattern was similar to that of a T-SLD. No spectral modulation was found in the spectral distribution of the HH-SLD.

References

[6-1] Chapuran T.E., Wagner S.S., Menendez R.C., Tohme H.E., and Wang L.A., *Broadband Multichannel WDM Transmission with Superluminescent Diodes and LEDs*, Globecom '91, Section 18.4, 1991, pp. 612-618.

[6-2] Peralta S., and Ruda H., *Applications for Advanced Solid-State Lamps*, IEEE Industry Applications Magazine, July/August 1998, pp. 31-42.

[6-3] Reyna R.F., Marti A., Algora C., Maroto J.C., and Araujo G.L., *Influence of Size Factors in the Electroluminescent Emission of Large Area GaAs IRED's*, IEEE Transactions on Electron Devices, Vol. 44, No. 7, July 1997, pp.1174-1176.

[6-4] Burrow L.D., Causa F., and Sarma J., *1.3W Ripple-free Superluminescent Diodes*, IEEE Photonics Technology Letters, accepted May 2005.

[6-5] Kressel H., and Butler J.K., *Semiconductor Lasers and Heterojunction LEDs*, Academic Press, New York, 1977, Chapter 14.

Chapter 7
Conclusions and Future Work

7.1: Conclusions

The main aim of this thesis was to investigate the properties of high-power superluminescent diodes with the purpose of improving device efficiency. The work done during this PhD involved developmental work and, therefore, device modelling, fabrication and characterisation. Representative results from the experimental characterisation of over two hundred devices have been presented. The conclusions drawn from the research work presented in this PhD thesis can be summarised as follows:

Device design, fabrication and characterisation The operating characteristics of in-house designed and fabricated stripe, tapered and parabolic SLDs have been presented. In the present devices the etched deflector was ion beam etched at 45° to the $(01\bar{1})$ plane for effective lasing suppression. A new monitoring technique was developed to improve the quality of in-house-deposited AR-coatings. By AR-coating the SLD output facet an increase in output power of a factor of five was obtained with respect to un-coated devices, achieving record-high optical powers in excess of 1.3W (pulsed, at 3kAcm^{-2}) from AR-coated tapered-SLDs, with 16% peak wall-plug efficiency. Under CW operation 67mW optical output powers (at 0.6kAcm^{-2}) were measured before material gain saturation (corresponding to approximately 2MWcm^{-2} internal power density at the facet). The corresponding spectra were ripple-free with less than 0.1dB intensity modulation from the 0.1nm Fabry-Perot cavity mode spacing, indicating that the etched v-groove deflector effectively provides lasing suppression. The SLD output was measured to be mainly TE polarised as expected from compressively strained quantum well material, with a corresponding 0.97 degree of polarisation.

Output Beam Characteristics The output beam profiles measured from in-house SLDs are typically elliptic (different lateral and vertical beam divergence). However, the device design can be optimised to achieve quasi-circular beam cross section for applications including illumination, and for inexpensive coupling to simple optical (aspherical) lenses.

FWHM Spectral Characteristics Typical spectral widths of 20nm (corresponding to approximately 45μm coherence length) were measured from SLDs fabricated from laser-type high-power double-heterostructure material with three identical QWs. By modifying the material epitaxy, incorporating QWs of different thicknesses, 40nm FWHM spectral widths centred at 1μm peak wavelength were obtained with Gaussian-like spectral distribution, corresponding to 16.5μm coherence length, comparing well with other results presented in the literature.

Device Efficiency Improvement Optical gain saturation was typically observed in the sub-linear light-current characteristics of SLDs and in the broadening of the FF patterns at high injection currents and attributed to the depletion of the carriers (hole-burning). Although an intrinsic device characteristic, optical gain saturation can be reduced by reducing the optical feedback from the device output facet. This has been achieved here in two ways:

- by tapering the injection contact geometry, thereby, effectively reducing the extent of the active region at the rear of the device. Tapered-SLDs were demonstrated to be less susceptible to optical gain saturation than conventional stripe-SLDs with same active volume, consistently achieving a factor of two wall-plug efficiency enhancement from tapered SLDs;
- by AR-coating of the output facet to effectively reduce the optical feedback and, therefore, carrier depletion at the rear of the active region, in addition to increasing optical transmission. A factor of five increase in optical output power (and wall-plug efficiency) was achieved by reducing facet reflectivity from 30% to approximately 1%.

Modelling results were presented to show that it is possible, in principle, to maximise device efficiency by computing the 'optimal' device length necessary given the other device parameters. It was found that optical saturation limited the output power of a SLD with too small a contact length whilst a reduction in current density and hence optical gain had the same effect for devices with lengths greater than the optimal length.

Finally, another method was investigated for increasing SLD efficiency by increasing the fraction of spontaneous emission coupled to the forward travelling photon density. This was achieved by including index-guided sections along the length of the SLD. This method was demonstrated to be effective only for stripe-geometry SLDs, achieving approximately 22% increase in wall-plug efficiency for a specific configuration with the index-guided region at the rear of the device. On the other hand, the reduction in wall-plug efficiency consistently observed in tapered-geometry SLDs with index-guiding regions was attributed to the fact that the increase in spontaneous

emission coupling to the forward travelling ASE was counter-balanced by a significant increase in optical gain saturation, as verified also by the 50% increase in lateral far field FWHM observed in such devices at high injection currents.

SLD-to-fibre Coupling The efficiency of coupling in-house fabricated SLDs to single- and multi-mode optical fibres was estimated by using two different techniques: butt-coupling and coupling using a system of lenses. A maximum of 84% coupling to multi-mode fibre (corresponding to approximately 0.75W optical power in the fibre) and 5.6% in single-mode fibres (7.5mW into the fibre) were obtained by using index-matching gel to reduce interface reflections. Modelling results were used to verify the experimental results and estimate the losses and the effect of optical gain saturation on the coupling efficiency. Optical coupling to single-mode fibres was significantly improved (by a factor of four, achieving 23%, corresponding to approximately 45mW into the fibre with non-AR coated SLDs) by using the system of lenses coupling. The system of lenses was designed to reduce the astigmatism of the output beam and to focus the beam to a spot with a diameter less than 10μm. After the onset of superluminescent operation the coupling efficiency remained constant for all devices indicating that optical saturation did not significantly affect the efficiency of lens coupling. The losses in the system were estimated, recognising that alignment was critical to the performance of the optical system.

New SLD designs proposed in this PhD Thesis The development of two novel SLD designs was presented:

- **Monolithic array of SLDs:** Novel arrays of edge-emitting tapered-SLDs were designed and fabricated for applications that require high-power, relatively broad-band and compact optical sources. Especially designed longitudinal v-groove deflectors were incorporated in the device design to prevent optical cross-talk between the array elements and, therefore, to reduce optical gain saturation. Output powers in excess of 2.7W (pulsed, at 3.5kAcm^{-2}) were achieved from AR-coated arrays of tapered-SLDs, with approximately 10% peak wall-plug efficiency. No significant spectral modulation was observed. The beam profiles measured from tapered-SLD arrays were similar to those obtained from individual tapered-SLDs, indicating that there is no coherent coupling between the elements. The experimental results were validated by those obtained from the models.

- **Segmented-contact Hammer-Head SLD:** The novel design of the segmented-contact tapered-SLD was also presented. This device was developed

to achieve linear power-current characteristics by careful control of the drive current in each contact, e.g., for optical signal modulation applications. The spectral distribution and coherence curve obtained from such devices showed no significant spectral modulation, indicating that the segmented contact did not introduce further, undesirable reflections.

Device Modelling Two models based on the ray analysis have been developed to interpret the operational characteristics of the devices studied here. The first model was used to calculate the power-current characteristics and spectra of SLDs. In addition, with this model it was possible to derive the longitudinal photon density distribution in the SLD and, therefore, estimate the effect of hole-burning on the device characteristics. The model was also extended to analyse longitudinally non-uniform SLDs by dividing the contact geometry into longitudinal sections, achieving excellent agreement between theoretical and experimental results for all geometries considered. In this model current spreading was not included.

The second ray model was developed to compute the near and far field intensity characteristics of SLDs with any geometry, including the arrays. In this model carrier spreading, carrier diffusion and optical gain saturation were accounted for by adopting a two-dimensional, super-Gaussian carrier density distribution, achieving realistic beam profiles and, therefore, excellent agreement with those measured in the laboratory.

7.2: Suggestions for further work

Thermal Management The majority of the experimental results presented in this thesis have been measured from SLDs operating under pulsed conditions (5μs, 200Hz) because the thermal management of the device have not been optimised yet. The preliminary results obtained under CW conditions [Chapter 4] give an indication of the effect of the high temperature developed in the device at high (CW) currents on the output power. One main technological development to be considered is the optimisation of the heat dissipation properties of the device mount.

SLD Spectral Properties For applications involving WDM, [7-1], [7-2], and short haul optical links it is desirable to have access to high power optical sources with relatively broad bandwidth. In this respect there is scope to

modify the material epitaxy to further increase the spectral full-width-at-half-maximum. The maximum spectral FWHM obtained in this thesis was 40nm.

Device Modulation For applications including optical communications across short-haul links it could be advantageous to directly modulate the SLD for signal encoding, [7-3]. Therefore, it will be necessary to investigate and quantify the modulation characteristics of SLDs, modulation frequency response, useful lifetime, the effect of chirp. Preliminary ideas have been discussed within the group on using segmented contacts with only the smaller contact providing the AC signal for modulation to reduce stray capacitance and chirp.

Output Power and Wall-Plug Efficiency Increase By improving the quality of the AR coating for the output facet it will be possible to improve extraction efficiency and increase significantly the optical power output as well as the wall-plug efficiency, which at present is only contributing to optical gain saturation.

Improved Coupling to Single-Mode Fibres The incorporation of the etched deflector at the rear of the device has been proved to be extremely effective for suppressing lasing and therefore, achieve superluminescent operation with insignificant spectral modulation. So far the interest was in achieving ripple-free, high output optical powers. By reducing the output facet width it will be possible to optimise coupling efficiency to single mode fibres, the compromise will be made with the achievable output power. Another possibility to be investigated is that of incorporating an integrated lens in the device design, [7-4].

Beam Quality By careful design of both the material epitaxy and the contact geometry it is possible to achieve a near-circular output beam cross-section, as demonstrated by the far field profiles obtained from some of the devices discussed in this Thesis. A circular beam cross-section would be beneficial for applications including illumination and for inexpensive coupling systems using simple optical (aspherical) lenses to reduce the complexity and cost of the device package.

Device Modelling The two models developed during this research programme will be incorporated into one comprehensive model to compute the light-current and spectral characteristics and the field profiles simultaneously.

References

[7-1] Kilkelly P.D.D., Chidgey P.J., and Hill G., *Experimental Demonstration of a Three Channel WDM System Over 110km using Superluminescent Diodes*, Electronics Letters, Vol. 26, No. 20, September 1990, pp. 1671 – 1673.

[7-2] Wagner S.S., and Chapuran T.E., *Broadband High-Density WDM Transmission using Superluminescent Diodes*, Electronics Letters, Vol. 26, No. 11, May 1990, pp. 696-697.

[7-3] Amann M.C., and Harth W., *Modulation Characteristics of Double-Heterostructure Superluminescent Diodes*, Electronics Letters, Vol. 13, 1977, pp. 291.

[7-4] Koyama F., Liou K.-Y., Dentai A. G., Tanbun-ek T., and Burrus C. A., *Multiple-Quantum-Well GaInAs/ GaInAsP Tapered Broad-Area Amplifiers with Monolithically Integrated Waveguide Lens for High-Power Applications*, IEEE Photonics Technology Letters, Vol. 5, No. 8, August 1993, pp. 916-919.

Appendix A:
Superluminescent diode fabrication

Numerous fabrication steps are needed to create a working SLD from a wafer of s/c material, Figure A.1 - A.12. The fabrication procedure is as follows:

1. The material is thinned by lapping the n-side (substrate) of the wafer using *wet and dry* emery paper until a thickness of 150μm is achieved, Figure A.1. The thickness of the material is measured using a dial gauge with 20μm sensitivity.
2. A thin Ge/Ni/Au alloy is evaporated onto the n-side of the wafer and annealed at 430°C in a furnace for 2 minutes, Figure A.2. The annealing process ensures that the gold diffuses into the GaAs resulting in a good ohmic contact.
3. The p-side is thoroughly cleaned before a rib geometry pattern of negative photo-resist is layered on to it via a process involving UV radiation and developing, Figure A.3. The developer used is a weak solution of sodium hydroxide (NaOH).
4. The rib geometry is fabricated by ion beam etching (IBE) the wafer, Figure A.4.
5. A coating of SiO_2 is sputtered onto the p-side of the wafer to ensure electrical isolation between the rib contact and the rest of the wafer, Figure A.5.
6. Using acetone, the SiO_2 is lifted off the rib by dissolving the photo-resist sandwiched in-between the SiO_2 and the rib. The capping layer of the rib is now exposed, Figure A.6.
7. A layer of titanium and gold is evaporated over the rib and the SiO_2, Figure A.7.
8. Applying another layer of photo-resist that covers the rib, Figure A.8, the excess titanium and gold is removed by IBE to form a contact region over the rib, Figure A.9.
9. A final layer of photo-resist is applied to the p-side of the wafer leaving a gap where the deflector is produced by IBE, Figure A.10. The deflector is etched through the active layer at an angle of 45° for the reason described in Chapter 2, Figure A.11.
10. The photo-resist is removed from the wafer and the device is cleaved leaving a mirror-like front facet.

11. The n-side of the SLD is mounted onto a copper heatsink using a conductive silver epoxy resin and a gold wire is ultra-sonically bonded onto the p-side of the wafer, Figure A.12.

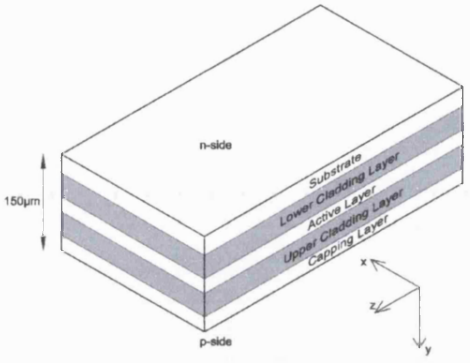

Figure A.1: *The wafer is lapped to a thickness of 150μm*

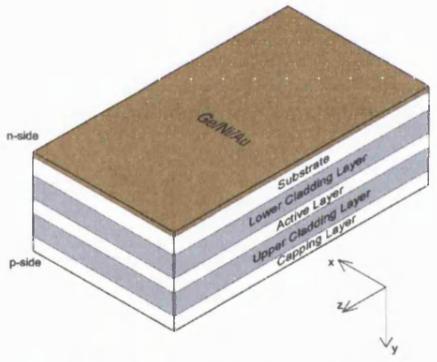

Figure A.2: *A Ge/Ni/Au alloy is evaporated onto the wafer*

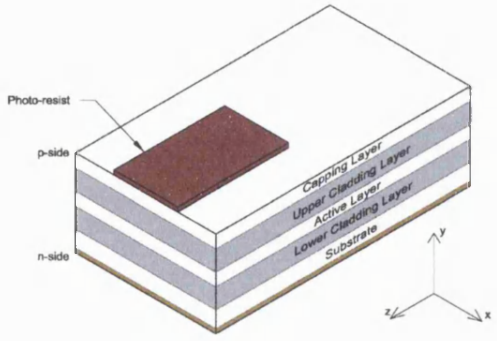

Figure A.3: *Photo-resist is applied to the wafer to define the rib geometry*

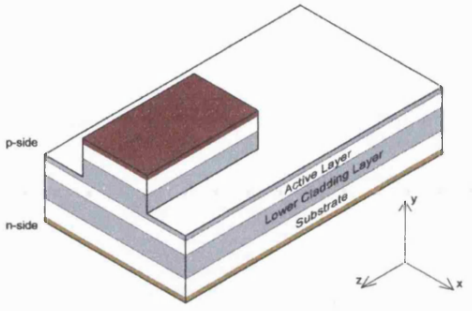

Figure A.4: *The rib is IBE through the capping layer and into the upper cladding layer*

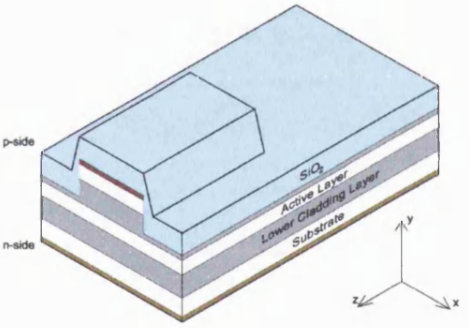

Figure A.5: *The p-side of the wafer is coated with SiO_2*

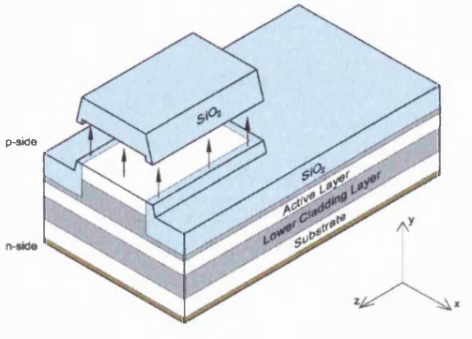

Figure A.6: *The SiO_2 is lifted of the rib*

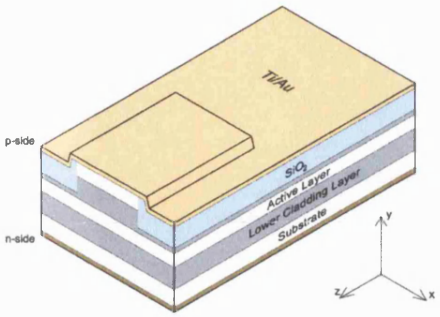

Figure A.7: *Ti/Au is evaporated over the rib and SiO_2*

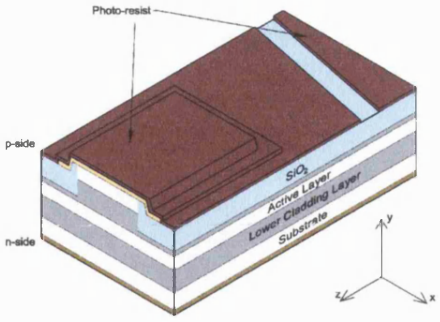

Figure A.10: *Photo-resist is applied to the p-side of wafer leaving a gap for the angled deflector*

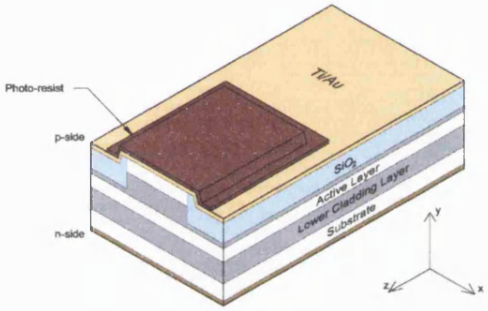

Figure A.8: *Photo-resist is applied to the Ti/Au to define the injection current contact area*

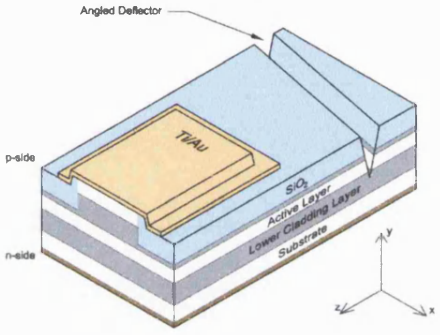

Figure A.11: *An angled deflector is IBE through the active layer*

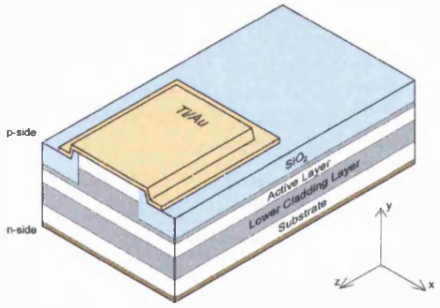

Figure A.9: *Excess Ti/Au is IBE away to form injection current contact region*

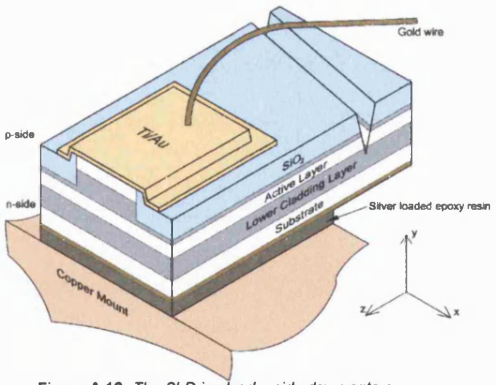

Figure A.12: *The SLD is glued n-side down onto a copper mount using a conductive silver epoxy resin. A gold wire is bonded onto the p-side of the SLD*

Appendix B

Fraction of spontaneous emission coupling to forward (and reverse) travelling photon density

In the following derivation the expression for the fraction of forward (and reverse) travelling photon density is obtained assuming that spontaneous emission is isotropic and considering a ray-model approach.

Supposing that all the radiation within the solid angle contributes to the forward travelling photon density, then:

$$\delta_f = \frac{\Delta\Omega_f}{4\pi} \qquad \text{(B.1)}$$

where δ_f is the fraction of spontaneously emitted forward travelling photons. A similar expression can be written for the fraction δ_r of spontaneous emission coupled to the reverse travelling photon density.

Assuming that all rays remain within the active medium cross-section, then

$$\Delta\Omega_f = \theta_V\theta_H \qquad \text{(B.2)}$$

where θ_V is the critical angle of total internal reflection at the interface between the cladding and the active layer, Figure B.1, and θ_H is the maximum angle for rays to remain within the active region in the lateral direction, Figure B.2.

Expression for θv:

The vertical angle, θ_v, is defined by the condition for total internal reflection of light rays at the interface between the cladding and the active layer (Figure B.1).

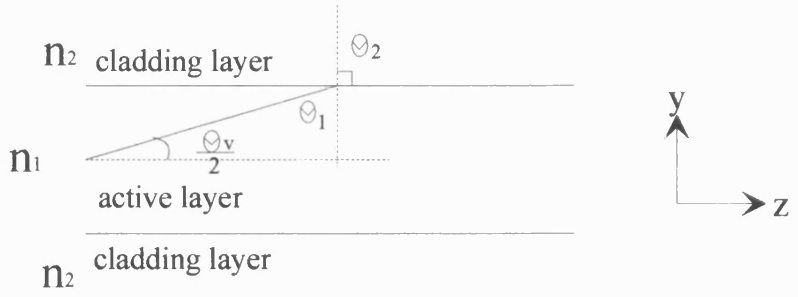

Figure B.1: Side view s*chematic representing showing the condition for total internal reflection of a light ray in the transverse direction.*

Using Snell's law

$$n_1 \sin\theta_1 = n_2 \sin\theta_2$$

For total internal reflection it is assumed that $\theta_2 = \frac{\pi}{2}$, therefore,

$$\sin\theta_1 = \frac{n_2}{n_1}$$

Since $\sin\theta_1 = \cos\left(\frac{\theta_V}{2}\right)$, then

$$\theta_V = 2\cos^{-1}\left(\frac{n_2}{n_1}\right) \qquad \text{(B.3)}$$

Expression for θ_h:

The width of the stripe contact defines the width of the active region. Only photons that remain in the active region are considered to define θ_h (Figure B.2).

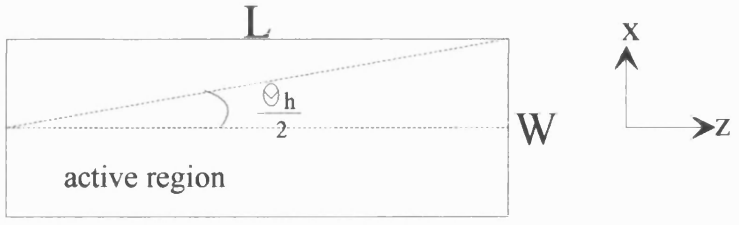

***Figure B.2**: Top view schematic of the active region; W=Width and L = Length of active region.*

It can be seen that

$$\tan\left(\frac{\theta_h}{2}\right)=\frac{W}{2L}$$

Considering L>>W and $\tan\theta \approx \theta$ for small values of θ, then the above expression can be simplified to

$$\theta_h = \frac{W}{L} \tag{B.4}$$

Combing equations (B.1), (B.3) and (B.4), the expression for the forward travelling photon density

$$\delta_f = \frac{1}{2\pi}\frac{W}{L}\cos^{-1}\left(\frac{n_2}{n_1}\right) \tag{B.5}$$

A similar expression for the reverse travelling photon density can be also derived. For a stripe SLD it is found that

$$\delta_f = \delta_r \tag{B.6}$$

For the tapered SLD it is assumed that the forward travelling photon density δ_f is given by (B.5). The reverse travelling photon density for a tapered SLD is given by

$$\delta_r = \frac{1}{\pi}\tan^{-1}\left(\frac{W_x}{L_x}\right)\cos^{-1}\left(\frac{n_2}{n_1}\right) \tag{B.7}$$

where W_x and L_X are the width and the length of each section respectively, with reference to Chapter 2.

Appendix C

Closed form solution of the forward and reverse travelling photon density equations

The general steady-state form for the forward and reverse travelling photon density equations is

$$\frac{dP}{dz} = \bar{g}_m(\lambda, N)P + \frac{\delta(\lambda)\delta_f N}{\mathrm{v}\tau_{sp}} \tag{C.1}$$

$$\frac{dQ}{dz} = -\bar{g}_m(\lambda, N)Q - \frac{\delta(\lambda)\delta_r N}{\mathrm{v}\tau_{sp}} \tag{C.2}$$

where $\bar{g}_m$ is the modal gain [Chapter 2, equation (2.5)]. By defining the constants

$$P_{sp} = \frac{\delta(\lambda)\delta_f N}{\bar{g}_m \mathrm{v}\tau_{sp}} \tag{C.3}$$

$$Q_{sp} = \frac{\delta(\lambda)\delta_r N}{\bar{g}_m \mathrm{v}\tau_{sp}} \tag{C.4}$$

and the new variables $\hat{P} = P + P_{sp}$ and $\hat{Q} = Q + Q_{sp}$, equations (C.1) and (C.2) can be re-written as

$$\frac{d\hat{P}}{dz} = \bar{g}_m \hat{P} \tag{C.5}$$

$$\frac{d\hat{Q}}{dz} = -\bar{g}_m \hat{Q} \tag{C.6}$$

Separating the variables and integrating by part equation (C.5):

$$\hat{P}(z) = \hat{P}_0 e^{\bar{g}_m z}$$

Since $\hat{P} = P + P_{sp}$ then, the closed form solution of the equation is

$$P(z) = P_0 e^{\bar{g}_m z} + (e^{\bar{g}_m z} - 1)P_{sp} \qquad \text{(C.7)}$$

Similarly, the solution for reverse travelling steady state photon density is found to be:

$$Q(z) = Q_0 e^{-\bar{g}_m z} + (e^{-\bar{g}_m z} - 1)Q_{sp} \qquad \text{(C.8)}$$

Appendix D
Field analysis of a Fabry-Perot cavity

The solutions of the steady state forward and reverse photon density equations are, respectively

$$P(z) = P_o e^{\bar{g}_m z} + (e^{\bar{g}_m z} - 1)P_{sp} \quad \text{(D.1)}$$

$$Q(z) = Q_o e^{-\bar{g}_m z} + (e^{-\bar{g}_m z} - 1)Q_{sp} \quad \text{(D.2)}$$

In a Fabry-Perot cavity, [Chapter 2], the boundary conditions for the field at the facets are

$$P(z = 0) = P_{IN} + R_0 Q_0 \quad \text{(D.3)}$$

$$Q(z = L) = R_L P_L \quad \text{(D.4)}$$

Substituting equation (D.4) into equation (D.2) it is possible to obtain the expression for Q_0:

$$Q_0 = R_L P_0 e^{2\bar{g}_m L} + R_L e^{\bar{g}_m L}(e^{\bar{g}_m L} - 1)P_{sp} + (e^{\bar{g}_m L} - 1)Q_{sp} \quad \text{(D.5)}$$

Similarly for determining P_0, substitute equation (D.5) into equation (D.3) to obtain

$$P_0 = \frac{P_{IN} + R_0 R_L e^{\bar{g}_m L}(e^{\bar{g}_m L} - 1)P_{sp} + R_0(e^{\bar{g}_m L} - 1)Q_{sp}}{1 - R_0 R_L e^{2\bar{g}_m L}} \quad \text{(D.6)}$$

Finally, the expression for the forward travelling photon density, at z=L, is

$$P_L = \frac{P_{IN} e^{\bar{g}_m L}}{1 - R_0 R_L e^{2\bar{g}_m L}} + \frac{(e^{\bar{g}_m L} - 1)\left(R_0 e^{\bar{g}_m L} Q_{sp} + P_{sp}\right)}{1 - R_0 R_L e^{2\bar{g}_m L}} \quad \text{(D.7)}$$

Appendix E

Carrier conservation rate equation

Consider a volume (ΔxΔyΔz) made from a s/c material with a current density J passing through it in a time Δt, Figure E.1.

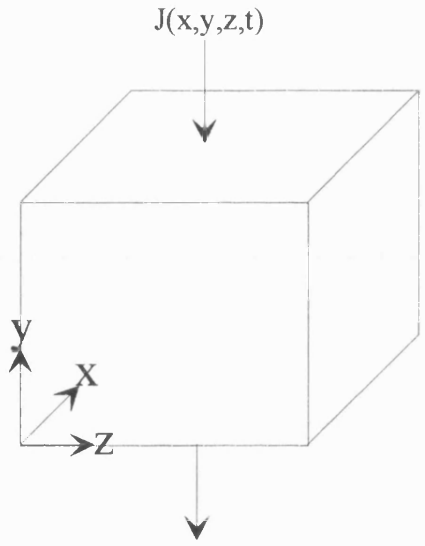

Figure E.1: *Schematic of a volume made from a s/c material with a current density passing through it.*

The number of particles entering the volume in time Δt by injection current pumping is

$$\frac{1}{q}J(x,y,z,t)\Delta x\Delta z\Delta t$$

where q is the magnitude of electronic charge.

The number of particles leaving the volume in time Δt is

$$\frac{1}{q}J(x,y-\Delta y,z,t)\Delta x\Delta z\Delta t$$

The net number of carriers entering the volume in time Δt is

$$\frac{1}{q}\left[J(x,y,z,t)-J(x,y-\Delta y,z,t)\right]\Delta x\Delta z\Delta t \qquad \text{(E.1)}$$

The increase in the number of carriers in the volume in time Δt is

$$\left(N(x,y,z,t+\Delta t)-N(x,y,z,t)\right)\Delta x\Delta y\Delta z \qquad \text{(E.2)}$$

where N is the injected carrier density.

However, since the volume is made from a s-c material, carriers recombine via stimulated or spontaneous emissions:

Total number of carriers recombining spontaneously in time Δt:

$$B_r N^2 \Delta x \Delta y \Delta z \Delta t$$

Total number of carriers recombining via stimulated emissions in time Δt:

$$\tilde{g}_m(\lambda, N)\big(P(z,t)+Q(z,t)\big)\Delta x \Delta y \Delta z \Delta t$$

where $\tilde{g}_m(\lambda, N)$ is the modal optical gain (s^{-1}); P(z,t) and Q(z,t) is the forward and reverse travelling photon density in the volume.

The total number of carriers recombining in the element in time Δt:

$$\left[B_r N^2 + \tilde{g}_m(\lambda, N)\big(P(z,t)+Q(z,t)\big)\right]\Delta x \Delta y \Delta z \Delta t \qquad \text{(E.3)}$$

For carrier conservation to occur, the increase in the number of carriers in the element should equal the net number of carriers entering the volume less the total number of carriers recombining in the volume in time Δt.

Combining equations (E.1),(E.2) and (E.3) obtain

$$\big(N(x,y,z,t+\Delta t)-N(x,y,z,t)\big)\Delta x \Delta y \Delta z = \frac{1}{q}\left[J(x,y,z,t)-J(x,y-\Delta y,z,t)\right]\Delta x \Delta z \Delta t$$
$$- \left[B_r N^2 + \tilde{g}_m(\lambda, N)\big(P(z,t)+Q(z,t)\big)\right]\Delta x \Delta y \Delta z \Delta t$$

Dividing all terms by ΔxΔyΔzΔt and taking the limits $\Delta y \to 0$ and $\Delta t \to 0$

$$\frac{\partial N}{\partial t} = \frac{1}{q}\frac{\partial J}{\partial y} - \left[\tilde{g}_m(\lambda, N)\big(P(z,t)+Q(z,t)\big) + B_r N^2\right] \qquad \text{(E.4)}$$

However, considering the steady-state case

$$\frac{\partial N}{\partial t} \to 0 \quad \text{and} \quad \frac{\partial J}{\partial y} \to \frac{J}{d}$$

where d is the thickness of active layer.

In addition, $\tilde{g}_m(\lambda, N) = \mathrm{v} g_m(\lambda, N) = g_m$ where v is the velocity of photon in the volume medium; $\bar{g}_m$ is the modal gain.

Substituting the results into equation (E.4), a steady-state rate equation for carrier conservation is derived

$$\frac{J}{vqd} = \bar{g}_m[P(z) + Q(z)] + \frac{B_r N^2}{v} \qquad \text{(E.5)}$$

Averaging equation (2.20) over the longitudinal length (L) of the active region

$$P_{av}(N) = \frac{1}{L}\int_0^L P(z)dz$$

$$P_{av}(N) = \frac{1}{L}\int_0^L \left(P_0 e^{\bar{g}_m z} + (e^{\bar{g}_m z} - 1)P_{sp}\right)dz$$

$$P_{av}(N) = \frac{(e^{\bar{g}_m L} - 1)}{\bar{g}_m L}\left(P_0 + P_{sp}\right) - P_{sp} \qquad \text{(E.6)}$$

Similarly, averaging equation (2.21) over the longitudinal length of the active region

$$Q_{av}(N) = -\frac{(e^{-\bar{g}_m L} - 1)}{\bar{g}_m L}\left(Q_0 + Q_{sp}\right) - Q_{sp} \qquad \text{(E.7)}$$

Appendix F
Experimental measurement techniques

LI characteristics

The LI characteristic of a s/c optical source describes how the light output power varies with the injection current. SLDs are specifically designed to avoid lasing so the LI characteristic is used to see how linearly the light output power increases with an increasing injection current.

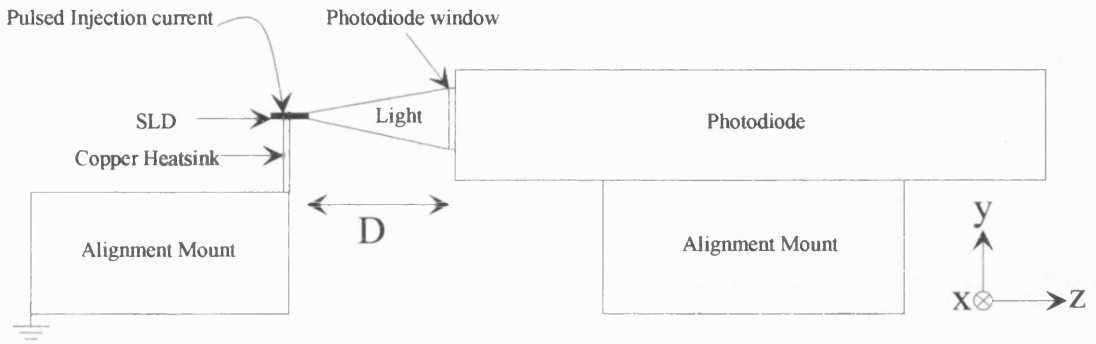

Figure F.1: *Schematic of the experimental set-up used to measure the LI characteristic of a SLD. D is the distance between the SLD and the photodiode.*

With reference to Figure F.1, the SLD is mounted onto a copper heatsink, which also acts as a current path, and attached to a mount for alignment along the three spatial axes. The light produced by the SLD is shone into the window of a photodiode. The photodiode measures the light output power of the SLD for increasing injection currents. Since the light diffracts as it emerges from the SLD the photodiode is placed in close proximity to the device (D≈1mm). This enables the photodiode to capture as much emitted light as possible.

Spectral characteristics

Spectral characteristics give the wavelength content of light emitted from a device. For SLDs the emitted light is expected to have a relatively large linewidth compared to laser diodes since the SLD is only partially coherent compared to the latter. The central peak wavelength of the emitted light depends on the s/c material from which the SLD is fabricated. The spectral characteristic of a SLD is measured using an Optical Spectrum Analyser (OSA), Figure F.2.

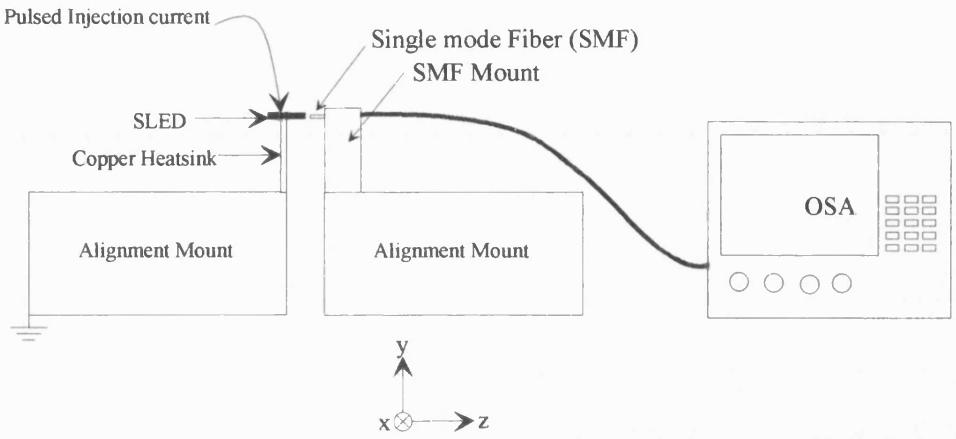

Figure F.2: *Schematic showing the experimental set-up using an OSA to measure the spectral characteristic of a SLD.*

The SLD is attached to a mount for alignment along the three spatial axes. A SMF with a core diameter of 5μm is butt-coupled to the SLD. The OSA measures the wavelength content of light captured by the SMF. The OSA has a wavelength resolution range of 0.01nm - 2nm.

FF pattern

The FF pattern is the angular light intensity distribution cross-section at a distance from a SLD. A lateral (x-z plane) and vertical (y-z plane) intensity distribution can be measured.

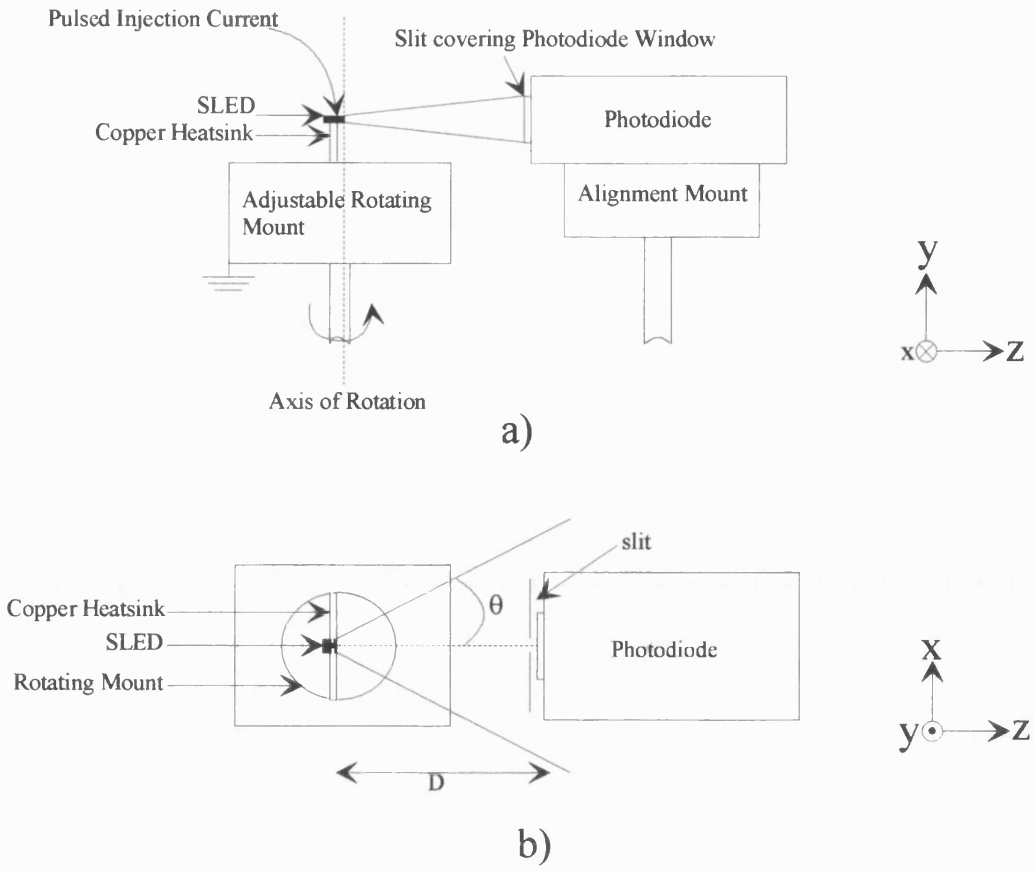

Figure F.3: *Schematic of the a) side view and b) top view of the experimental set-up used to measure the lateral FF pattern of a SLD. The light intensity is measured as a function of θ. D is the distance of the SLD to the photodiode.*

The SLD is mounted on a motorised rotating stage with the output facet placed on the centre of rotation. A metal plate with a 0.5mm slit is placed in front of photodiode window to improve the resolution of the measurement. The resolution is

$$\Delta\theta = \frac{W_{SLIT}}{D} \qquad \text{(F.1)}$$

where W_{SLIT} is the width of the slit placed over the photodiode and D is the distance of the SLD to the photodiode.

The minimum angular resolution of the motorised stage is 0.1°. A typical value of Δθ is 0.05° (when W_{SLIT}=0.5mm and D=10cm). The photodiode can therefore accurately resolve any angular rotation made from the rotating stage.

NF intensity profiles

The NF profile is a measurement of the light distribution across the front facet of a SLD.

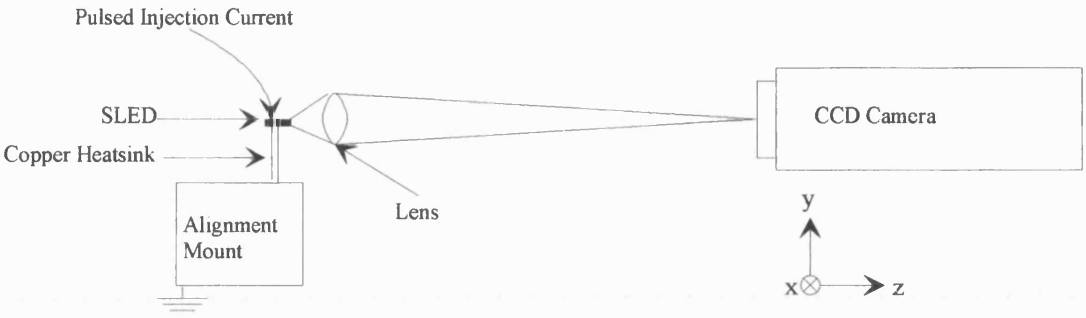

Figure F.4: *Schematic of the experimental set-up used to detect the NF profile of a SLD.*

The focal point of the lens is placed on the front facet of the SLD device. An image of the front facet is then projected onto a high-resolution camera, connected to a PC, to ensure correct alignment. When an injection current is supplied to the SLD the NF profile at the front facet of the device is scanned by the computer. The NF profile is measured for different injection currents to detect changes in the near field profile with current.

The measurement requires careful alignment and the charge-coupled device (CCD) camera needs to be calibrated before each set of measurements. The Numerical Aperture (NA) of the lens is chosen to be large so that a large fraction of the light emitted from the front facet of the device is captured. Typically NA = 0.54.

Appendix G(i)

Multi-layer structure and optical properties of material QT1137

Table G(i).1: *Epitaxial layer structure for material QT1137*

Layer	Thickness	Composition	Doping	Dopant
Capping	0.2 µm	GaAs	1×10^{19} cm^{-3}	Zn
Cladding	1.4µm	$Al_{0.44}$	1×10^{18} cm^{-3}	C
Guide	0.6µm	$Al_{0.3}$	3×10^{16} cm^{-3}	C
Barrier	100Å	GaAs	undoped	
QW	70Å	$In_{0.2}$/GaAs	undoped	
Barrier	100Å	GaAs	undoped	
QW	70Å	$In_{0.2}$/GaAs	undoped	
Barrier	100Å	GaAs	undoped	
QW	70Å	$In_{0.2}$/GaAs	undoped	
Barrier	100Å	GaAs	undoped	
Guide	0.6µm	$Al_{0.3}$	3×10^{16} cm^{-3}	Si
Cladding	1.4µm	$Al_{0.44}$	1.4×10^{18} cm^{-3}	Si
Buffer	0.5µm	GaAs	1×10^{18} cm^{-3}	Si

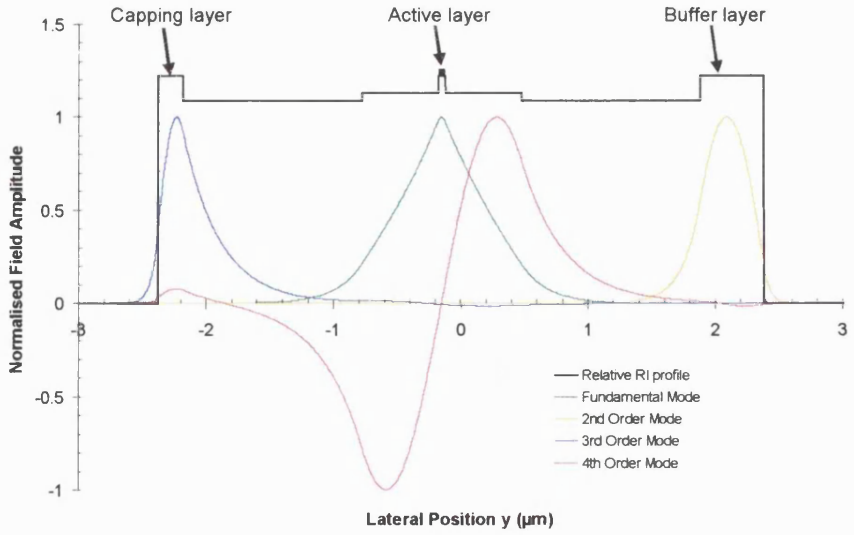

Figure G(i).1: *Relative refractive index profile of material QT1137 and corresponding vertical bound modes*

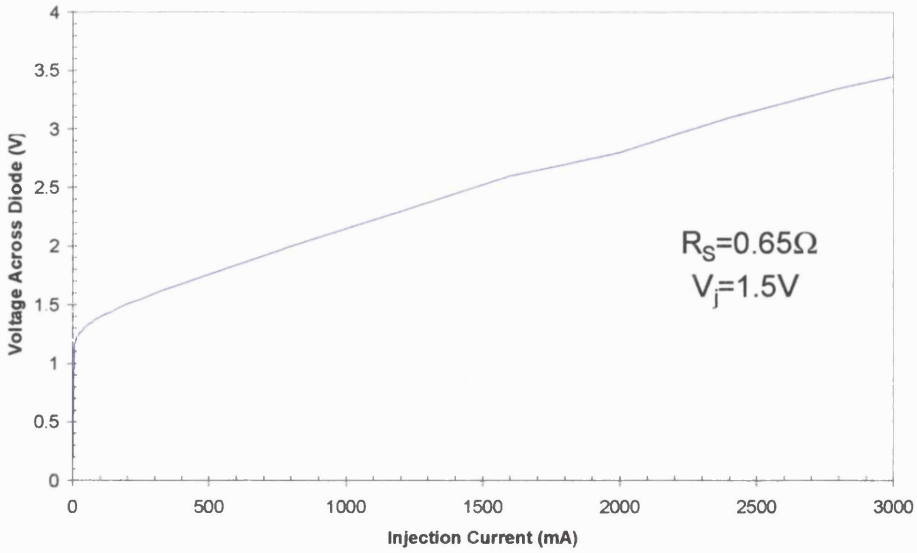

Figure G(i).2: VI *characteristic measured from S-SLD(50) fabricated from material QT1137*

Table G(i).2: *Material constants used to simulate the characteristics of SLDs fabricated from QT1137*

Material Constants	Value
B_r	1.0×10^{-10} (cm^3s^{-1})
A_0	1.8×10^{-16} (cm^2)
N_{tr}	1.45×10^{18} (cm^{-3})
α_s	-4 (cm^{-1})
α_f	-4 (cm^{-1})
Γ	0.14

Appendix G(ii)

Multi-layer structure and main characteristics of material QT1819

Table G(ii).1: Epitaxial layer structure of material QT1819

Layer	Thickness	Composition	Doping	Dopant
Capping	0.18 μm	GaAs	high	Zn
Cladding	1.34μm	$Al_{0.43}$	2×10^{18} cm^{-3}	C
Guide	0.62μm	$Al_{0.29}$	5×10^{16} cm^{-3}	C
Barrier	100Å	GaAs	undoped	
QW	95Å	$In_{0.2}/GaAs$	undoped	
Barrier	100Å	GaAs	undoped	
QW	70Å	$In_{0.2}/GaAs$	undoped	
Barrier	100Å	GaAs	undoped	
QW	50Å	$In_{0.2}/GaAs$	undoped	
Barrier	100Å	GaAs	undoped	
Guide	0.6μm	$Al_{0.29}$	1.2×10^{17} cm^{-3}	Si
Cladding	1.4μm	$Al_{0.43}$	1.5×10^{18} cm^{-3}	Si
Buffer	0.5μm	GaAs	high	Si

Materials QT1819 and QT1137 are very similar in structure; the only difference is in the width of the QWs. According to quantum mechanics the emitted photon energy of a s/c QW increases as the well width decreases, [1]. By suitably choosing the QW widths the spectral bandwidth obtained from the material emission can be engineered. The calculated transition energy as a function of QW width for $Ga_{0.8}In_{0.2}As$ QWs bounded by GaAs barriers is presented in Figure G(ii).1.

The QW widths of QT1819 were chosen to obtain transition energy steps of approximately 50meV ($\Delta\lambda_{peak}\approx25nm$) between QWs thereby obtaining an overall theoretical spectral bandwidth of approximately 75nm. Transitions from the second QW energy levels are neglected in the first approximate analysis. The spontaneous emission spectrum of the material provided by the manufacturer is presented in Figure G(ii).2, [2]. The VI characteristic obtained from S-SLD(50) fabricated from QT1819 is

presented in Figure G(ii).3. The voltage across the SLD is unexpectedly large for all drive currents when compared to the VI characteristic of QT1137 and is attributed to defective material.

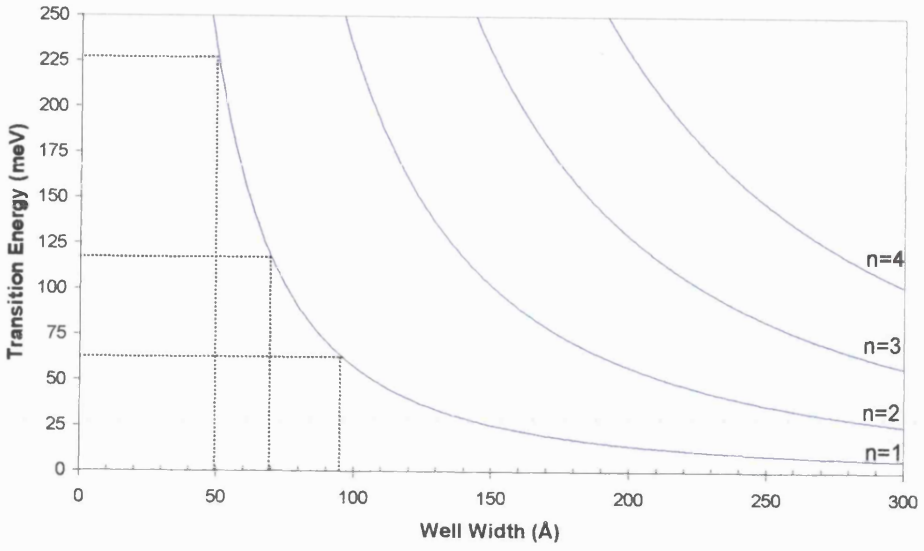

Figure G(ii).1: *The calculated transition energy versus the well width for a $Ga_{0.8}In_{0.2}As$ quantum well bounded by GaAs barriers where n is the transition level.*

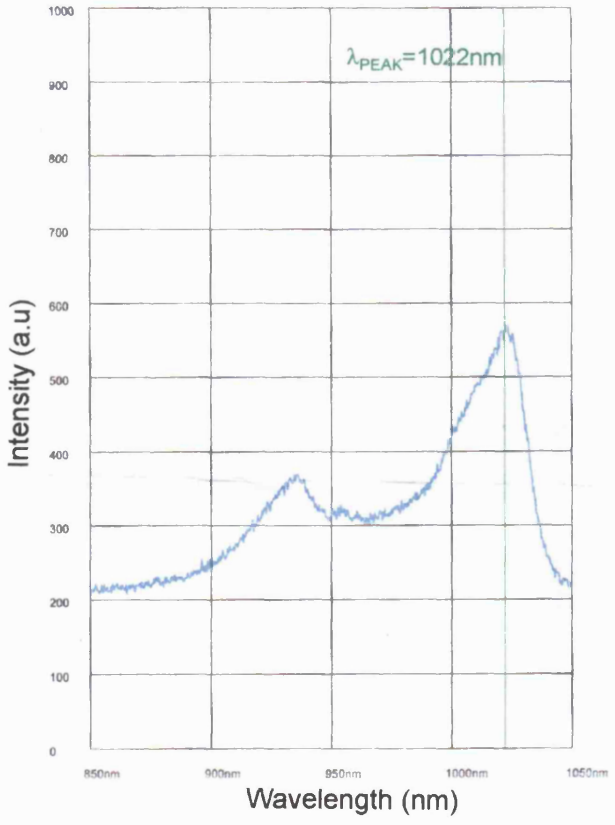

Figure G(ii).2: *Spontaneous emission spectra from material QT1819.*

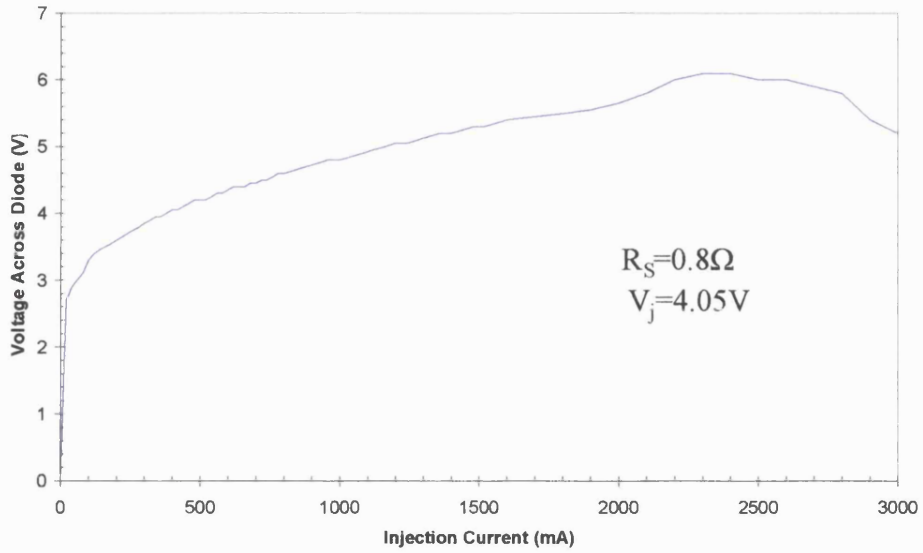

Figure G(ii).3: *VI characteristic of material QT1819 measured from S-SLD(50)*

References

[1] Lin C.-F., Lee B.-L., and Lin P.-C., *Broad-Band Superluminescent Diodes Fabricated on a Substrate with Asymmetric Dual Quantum Wells*, IEEE Photonics Technology Letters, Vol. 8, No. 11, November 1996, pp.1456-1458.

[2] Dr J. S. Roberts, EPSRC National Centre for III-V Technologies, University of Sheffield, UK.

Appendix H
AR coating techniques

This Appendix describes two techniques for AR coating the output facet of a SLD.

Technique 1:

An AR coating is applied to reduce the reflectivity of output facet of a SLD. The equipment used to AR coat a SLD is presented in Figure H.1. The process takes place inside a vacuum chamber at a pressure of 5×10^{-3} mbar. An electron beam is 'fired' at a target consisting of the AR coating material (ZrO_2/TiO_2). The ZrO_2/TiO_2 is sputtered onto the output facet of the SLD which is positioned under the target. Current is applied to the SLD and the emitted power is detected by a photo detector also present within the chamber. As the AR coating is deposited on the output facet the change in detected output power is monitored. When the output power reaches the maximum value the process is terminated. By this process an optimal single layer AR coating is achieved.

Technique 2:

This technique of applying an AR coating to the output facet of a SLD is presented in Figure H.2. The method of sputtering the AR coating material is the same as that described for Technique 1 above. The difference between the techniques is in the way the AR coating film deposition is monitored. In this second technique a laser diodes (LD)(λ_{LD} = 807nm) is used to measure the AR coating thickness. Using a beam splitter the light from the LD is shone onto a sample (with the same material composition as the SLD) and measured using a photo detector. When the light intensity measured by the photo detector reaches a minimum the thickness of the AR coating is equivalent to $\lambda_{LD}/4$. The time taken to reach the minimum is measured (t_{min}). However, the minimum reflected intensity corresponds to the LD wavelength of the light produced from the LD and not necessarily to that of the SLD. Therefore, extra AR coating time

(t_{extra}) is necessary to compensate for the difference in λ. The estimated extra-time is determined by the following expression:

$$t_{extra} = t_{\min} - \frac{t_{\min} \times \lambda_{SLD}}{\lambda_{LD}} \qquad \text{(H.1)}$$

where λ_{SLD} is the central wavelength emitted from the SLD spectral distribution. The optimal AR coating for this technique relies upon two assumptions: a constant deposition rate of the AR coating, and the deposition terminating precisely at the extrapolated time. Due to these two assumptions the AR coating Technique 2 is less accurate than Technique 1, therefore the latter has been used more often in the work presented in this thesis.

A comparison of typical output facet reflectivities produced by the two AR coating techniques is presented in Table H.1.

Table H.1: Comparison of *the output facet reflectivity and accuracy obtained with the two AR coating techniques described above.*

AR Coating Method	Output Facet Reflectiity
Technique 1	1.2% (±0.5%)
Technique 2	1.8% (±0.8%)

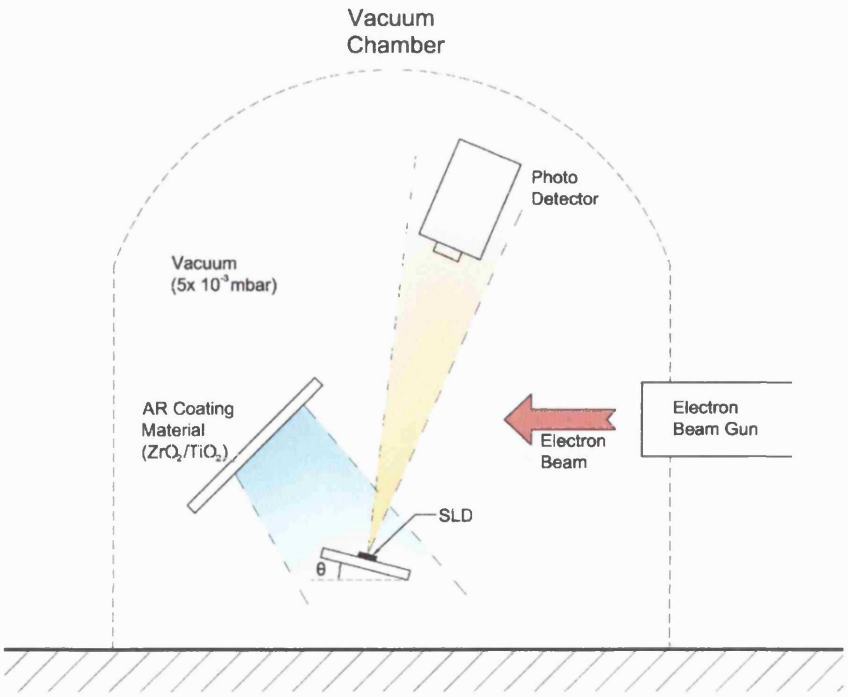

Figure H.1: *Schematic representation of the equipment used for Technique 1.*

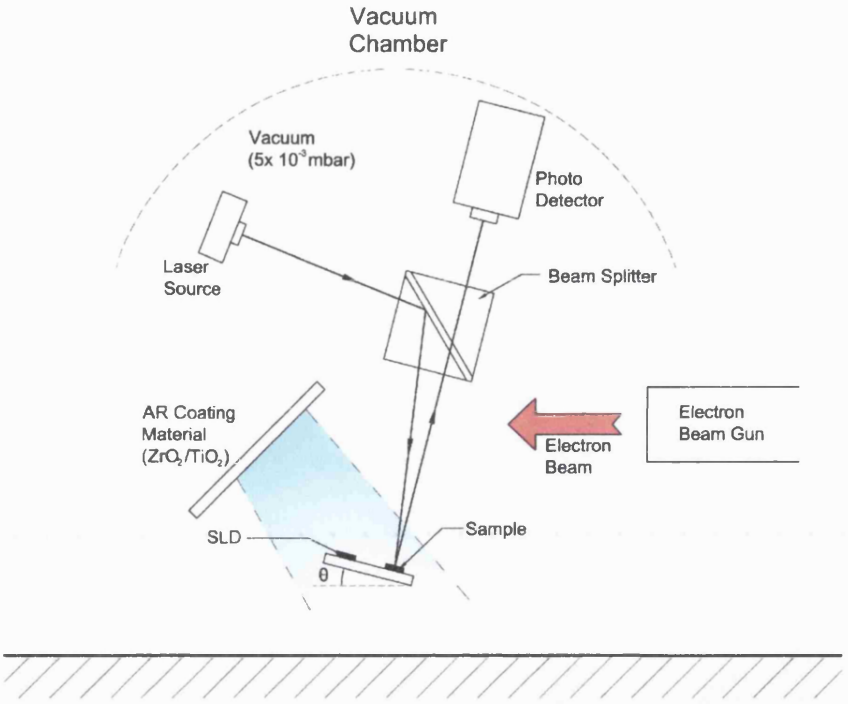

Figure H.2: *Schematic representation of the equipment used for Technique 2.*

Appendix I
Novel geometry SLDs

The pictures presented in this Appendix are of the novel geometry SLDs presented in Chapter 6. The pictures are taken with an objective lens (×10) microscope imaging the SLD onto a CCD camera.

T-SLD array:

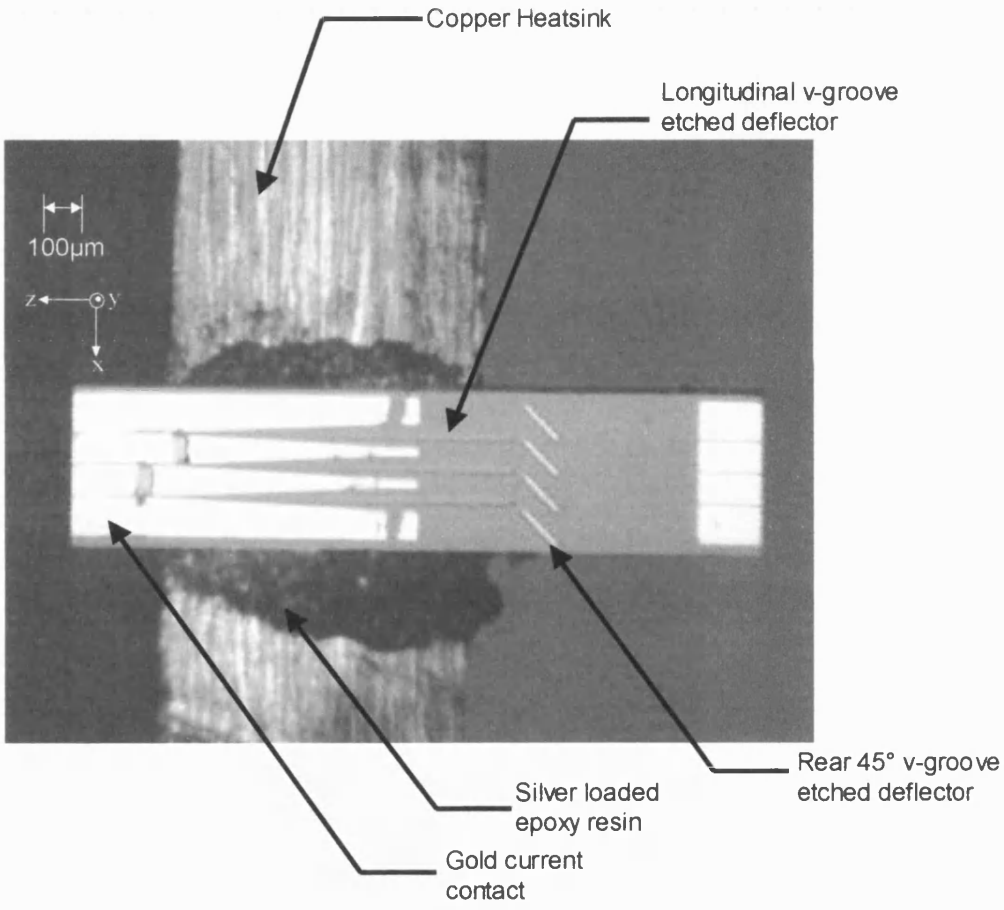

Figure I.1: *Top view of the 4-element T-SLD array.*

HH-SLD:

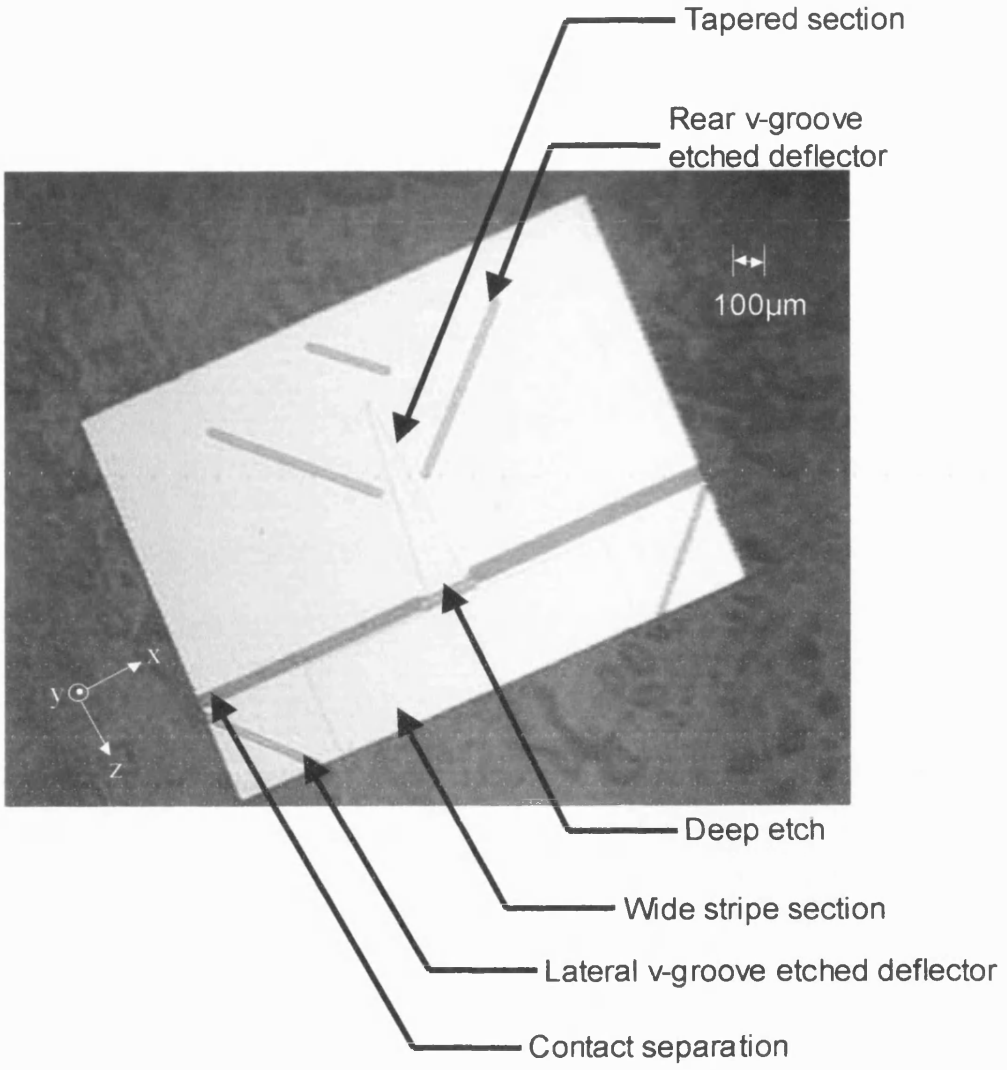

Figure I.2: *Top view of the HH-SLD.*

Appendix J

Journal and conference publications from research

[1] L. Burrow, F. Causa and J. Sarma, 'Ray model for the analysis of the operational characteristics of Straight-Stripe SLEDs', Semiconductor and Integrated Optoelectronics Conference (SIOE'03), Cardiff, Wales, April 2003.

[2] L. Burrow, F. Causa and J. Sarma, 'Coupling edge-emitting Superluminescent LEDs to optical fibres', Semiconductor and Integrated Optoelectronics Conference (SIOE'04), Cardiff, Wales, April 2004.

[3] L. Burrow, F. Causa and J.Sarma, 'Optimisation of the Wall-Plug efficiency of Superluminescent LEDs: theory and experimental characterisation', Quantum Electronics and Photonics (QEP'04), Glasgow, Scotland, September 2004.

[4] L. Burrow, F. Causa, 'High-Power Broad-Line-Width Ripple-Free Super-Luminescent Diodes', Semiconductor and Integrated Optoelectronics Conference (SIOE'05), Cardiff, Wales, April 2005.

[5] L.D. Burrow, F. Causa and J.Sarma, '1.3W Ripple-Free Superluminescent LED', Conference on Lasers and Electro-Optics (CLEO'05), Washington, U.S.A., May 2005.

[6] L. Burrow, F. Causa and J.Sarma, '1.3W Ripple-Free Superluminescent Diode', IEEE Photonics Technology Letters, accepted May 2005.